TERAHERTZ AND SUB-TERAHERTZ TUNABLE RESONANT DETECTORS BASED ON EXCITATION OF TWO DIMENSIONAL PLASMONS IN InGaAs/InP HEMTs

by

NIMA NADER ESFAHANI
B.S., University Of Tehran, 2009
M.Sc., University of Central Florida, 2013

A dissertation submitted in partial fulfillment of the requirements
for the degree of Doctor of Philosophy
in the Department of Physics
in the College of Sciences
at the University of Central Florida
Orlando, Florida

Summer Term
2014

Major Professor: Robert E. Peale

ABSTRACT

Plasmons can be generated in the two dimensional electron gas (2DEG) of grating-gated high electron mobility transistors (HEMTs). The grating-gate serves dual purposes, namely to provide the required wavevector to compensate for the momentum mismatch between the free-space radiation and 2D-plasmons, and to tune the 2DEG sheet charge density. Since the plasmon frequency at a given wavevector depends on the sheet charge density, a gate bias can shift the plasmon resonance. In some cases, plasmon generation results in a resonant change in channel conductance which allows a properly designed grating-gated HEMT to be used as a voltage-tunable resonant detector or filter. Such devices may find applications as chip-scale tunable detectors in airborne multispectral detection and target tracking.

Reported here are investigations of InGaAs/InP-based HEMT devices for potential tunable resonant sub-THz and THz detectors. The HEMTs were fabricated from a commercial double-quantum well HEMT wafer by depositing source, drain, and semi-transparent gate contacts using standard photolithography processes. Devices were fabricated with metalized transmission gratings with multiple periods and duty cycles. For sub-THz devices, grating period and duty cycle were chosen to be 9 μm and 22%, respectively; while they were chosen to be 0.5 μm and 80% for the THz device. The gratings were fabricated on top of the gate region with dimensions of 250 μm × 195 μm.

The resonant photoresponse of the larger grating-period HEMT was investigated in the sub-THz frequency range of around 100 GHz. The free space radiation was generated by an

ultra-stable Backward Wave Oscillator (BWO) and utilized in either frequency modulation (FM), or amplitude modulation (AM) experiments. The photoresponse was measured at 4K sample temperature as the voltage drop across a load resistor connected to the drain while constant source-drain voltages of different values, V_{SD}, were applied. The dependence of such optoelectrical effect to polarization of the incident light, and applied V_{SD} is studied. The results of AM and FM measurements are compared and found to be in agreement with the calculations of the 2D-plasmon absorption theory, however, a nonlinear behavior is observed in the amplitude and the line-shape of the photoresponse for AM experiments. For detection application, the minimum noise-equivalent-power (NEP) of the detector was determined to be 235 and 113 $pW/Hz^{1/2}$ for FM and AM experiments, respectively. The maximum responsivity of the detector was also estimated to be ~ 200 V/W for the two experiments.

The far-IR transmission spectra of the device with nanometer scale period was measured at 4 K sample temperature for different applied gate voltages to investigate the excitation of 2D-plasmon modes. Such plasmon resonances were observed, but their gate bias dependence agreed poorly with expectations.

Dedicated to my mom and the memory of my father

ACKNOWLEDGMENTS

I wish to acknowledge my advisor, Professor Robert Peale, for his time, advice, and guidance given to me throughout my studies at UCF. Without his constant help and patience, this work would have never been in its present shape. I also wish to thank him for not hesitating to provide me with his streaming knowledge and ideas. I should also thank him for his continuous financial support during my time at UCF. He played a great role as my advisor and mentor. I owe everything that I have accomplished to his presence and his mentorship will never be forgotten.

I would also like to thank RYDH (Optoelectronic Technology Branch) in Air Force Research Laboratory (AFRL), Sensors Directorate, for their trust, and support, as well as the opportunity they gave me to be a part of their team. I should specifically thank Dr. Justin Cleary for his patience, support, and guidance during my years in AFRL. He was always there for me during the hard and easy times and I always benefitted from his support and knowledge, his helps will never be forgotten. I also acknowledge the financial support provided to me by AFRL during the past two and half years, I would like to thank Dr. Justin Cleary, and Dr. Jonahira Arnold for this financial support. I owe special thanks to Dr. Dave Tomich for being a grey beard.

I would like to thank Dr. Walter Buchwald, Dr. Masahiro Ishigami, and Dr. Enrique Del Barco for serving on my dissertation committee and spending their time evaluating this work.

I especially wish to thank Mr. Chris Fredricksen for his invaluable help in Labview and familiarizing me with different experimental instruments like Backward Wave Oscillators, Sub-THz waveguide components and cryogenics. The numerous helps and suggestions I got from him to setup the experiments will never be forgotten.

I also thank my UCF group member, Doug Maukonen for his help and advice on setting up the low-noise electronics and circuitry for photoresponse measurements.

I should also thank Dr. Andrey Muraviev for his help in data analysis and polarization dependence measurements. He played an important role to resolve polarization related problems.

I would take the opportunity to say thanks to David Bradford and Xin Qiao for their valuable help in the machine shop.

I wish to thank Dr. Walter Buchwald, Dr. Joshua Hendrickson, Andrew Davis, and Sandy Wentzel for their extensive efforts to fabricate the measured HEMT structures.

I owe a special thanks to Dr. Justin Cleary, Dr. Joshua Hendrickson, Dr. Shiva Vangala, and Dr. Julian Sweet from AFRL for their continuous help, concern and support. I've learned a lot from them and they were always there for me as a friend and a co-worker when I needed them for any moral and/or scientific support.

I should also thank Dr. Shiva Vangala along with my UCF group member Imen Rezadad for their valuable help in taking the SEM pictures of the measured devices.

This work was supported by Air Force Office of Scientific Research (AFOSR), Program manager: Dr. Gernot Pomrenke. I would like to acknowledge his financial on this research project.

I would like to acknowledge my other colleagues at UCF: Dr. Tatiana Brusentsova, Janardan Nath, Dr, Gautam Medhi, Deep Panjwani, Dr. Monas Shahzad, Farnood Khalilzadeh-Rezaie, Pedro Figueiredo, Doug Moukonen, Javaneh Rezadad, Evan Smith and Jonathon Arnold for their support.

I would also like to thank my friend Behzad Nematpajouh for standing by my side in all occasions for these many years.

Above all I would like to thank my mom, late father, sisters and brother for believing in me and for their constant love, support and encouragement, which has made all this work possible.

TABLE OF CONTENTS

LIST OF FIGURES

LIST OF TABLES

CHAPTER 1 INTRODUCTION

1.1 Background and motivation

The terahertz (THz) band is a frequency range of $(0.3\text{-}10)\times10^{12}$ Hz in electromagnetic waves spectrum and it occupies the regime between radio waves and Infrared light. Many materials ranging from semiconductors to explosive and living tissues are either semitransparent to THz frequencies or have specific terahertz fingerprints due to their molecular rotational and vibrational transitions, lattice vibrations in solids, and intraband transitions in semiconductors [1]. Based on these interactions with the THz field, materials can be divided into three categories for THz applications, namely, metals and highly doped semiconductors that are highly reflective (due to their large real permittivity in THz), materials with water content and/or polar molecules like organic compounds and explosives that are highly absorptive or have absorption finger prints, and non-polar molecules such as paper, plastic, cloths, wood, wood products and ceramics that are transparent at THz frequencies. These materials are usually opaque to visible light. The THz transparency of some of the visibly opaque materials like fabrics and cloths, along with distinctive absorption features of explosive and organic compounds make THz a unique window for applications such as security screening, imaging and explosive detection [2-11] as well as applications in optoelectronic subsystems, airborne multispectral detection, and target tracking. Figure 1 presents a diagram of the electromagnetic wave spectrum. The terahertz region is marked with some of its applications in the figure.

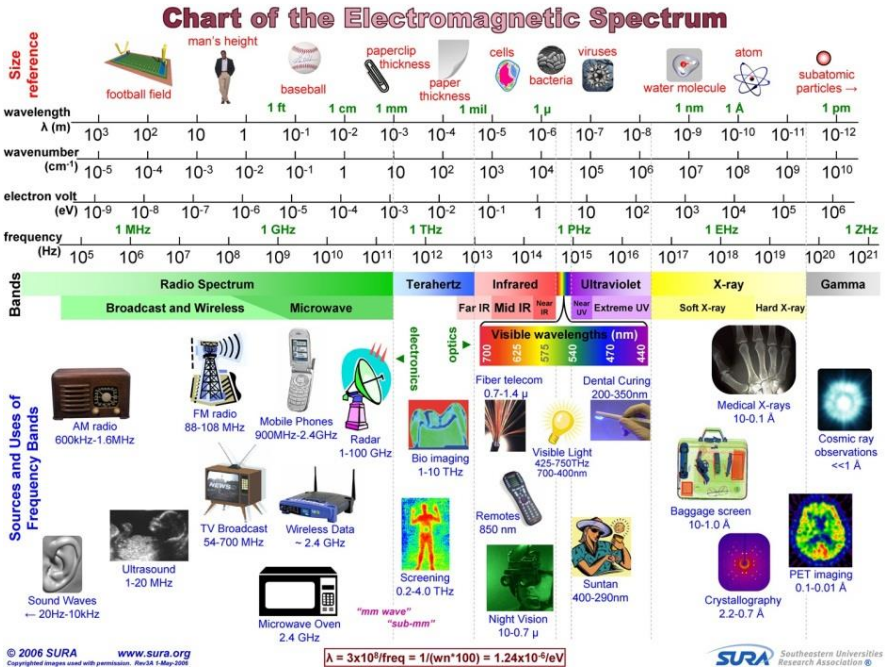

Figure 1: EM-waves spectrum with the terahertz region marked with some of its applications.
Credit: The Southeastern Universities Research Association (SURA)

Despite considerable applications, however, technology at these frequencies remains limited, partly due to the lack of reliable sources and detectors, the so-called "THz Gap". This is historically due to hard fabrication processes and small feature sizes in components suitable for THz applications. Recent years, however, has witnessed an extensive research efforts to fill the THz Gap which has resulted in the fast growth of newly emerging THz sources such as Backward Wave Oscillators [12], optically pumped gas lasers [13], and THz quantum cascade lasers (QCLs) [14-22]. The search for a reliable THz detector, however, hasn't been that successful. Commercially available detectors are mainly non-tunable and broadband [23-28]. These detectors are based on number of different technologies, namely, bolometric components

[27-29], Schottky diodes [23], pyroelectric materials [24, 30], and Golay Cell [31, 32]. Each of these technologies experiences a certain drawback. Bolometers offer very high sensitivities but they require cryogenic temperatures of < 4 K to remove the background heat. This makes them expensive and not always available. They also have slow sampling rates to allow for the heat dissipation process. Schottky diode-based detectors are not tolerable to high power sources such as gas lasers. Pyroelectric-based detectors and Golay Cell also require a relaxation time to allow them dissipate the heat generated by the incident THz radiation. Table 1 compares the THz detection characteristics of the abovementioned devices.

Table 1: THz broadband detectors

Detector (Manufacturer)	**NEP ($W/Hz^{0.5}$)**	**Responsivity (V/W)**	**Sampling rate**	**Operating Temperature**	**Operating frequency (THz)**
Schottky diode (Virginia Diodes)	1×10^{-10}	< 4000	1 GHz	Room Temp.	0.1 – 1.7
QMCI Pyroelectic detector	4.4×10^{-10}	1.83×10^{5}	10 Hz	Room Temp.	< 20
Gentec-EO Pyroelectric	2×10^{-10}	4×10^{5}	5 Hz	Room Temp.	0.1 - 30
Golay Cell (Microtec)	10^{-8}	< 5000	70 Hz	Room Temp.	0.02 - 20
Golay Cell (Tydex)	1.4×10^{-10}	1×10^{5}	20 Hz	Room Temp.	0.15 - 20
QMCI Hot Electron Bolometer	7.5×10^{-13}	3500	1 MHz	4.2 K	0.06 – 0.5

Detector (Manufacturer)	NEP ($W/Hz^{0.5}$)	Responsivity (V/W)	Sampling rate	Operating Temperature	Operating frequency (THz)
QMCI Germanium Bolometer	2×10^{-12}	1×10^{4}	< 1 KHz	8 K	0.1 - 20
IR-Labs Hot Electron Bolometer	8×10^{-13}	------	600 KHz	4.2 K	0.06 - 1.5
IR-Labs Si Bolometer	1.2×10^{-13}	2.4×10^{5}	200 Hz	4.2 K	0.15 - 20

Commercially available detectors, suffer from the lack of tunable THz detectors with resonantly enhanced responsivity and NEP in a narrowband frequency range. Extensive research efforts are spent in studies of such devices based on two-dimensional electron systems, such as metal-oxide-semiconductor field-effect transistors (MOSFETs) [33-34], HEMTs [35-55], and Graphene [56-57]. These devices can be promising candidates to fill this gap due to their possible room temperatures operation in devices with high mobility values ($> 10^3$ cm^2/Vs), and their sensitive response with NEP values of ~ 10^{-11} to 10^{-12} $W/Hz^{0.5}$.

1.2 High Electron Mobility Transistors

High electron mobility transistors (HEMTs) are electronic devices based on field effect transistors (FETs). These devices are grown by molecular beam epitaxy (MBE) or metal-organic chemical vapor deposition (MOCVD) growth of two different wide and narrow bandgap semiconductor layers. All layers are lattice matched to the substrate. At the interface of the two layers with different bandgaps there forms a quantum well due to the conduction band offset

between the two. An n-type thick or δ-doped layer based on the wide bandgap material is placed in the structure on top of the interface to provide the quantum well with the required doping. The dopants fall and get trapped into the interface due to the quantum well formation. These dopants will occupy the ground level state of the potential well and their movement in the direction normal to the interface will be limited due to the quantum well's quantized states. They are, however, free to move in the plane of the interface and are therefore called two dimensional electron gas or "2DEG". The doped layer is separated from the interface by a few nanometers thick undoped layer of the same type, called "Spacer". This will reduce the scattering of the charge carriers inside 2DEG by the extra leftover dopants in the doped layer and therefore increase device's mobility significantly.

1.3 HEMTs as plasmon based terahertz devices

Figure 2 presents the diagram of a grating-gated HEMT structure. The 2DEG layer with sheet charge density, n_s, is located at the distance d below the surface. Grating with period a, and openings t acts as the gate region with the incident x-polarized THz radiation propagating along the z-axis (with the x-axis being perpendicular to the grating bars). When grating period is much smaller than the wavelength of the incident light (~λ/100), it will see the THz radiation as a DC electric field. Grating bars will then become polarized and induce localized electric fields inside the semiconductor layers underneath. These local fields have the same spatial periodicity as the grating bars and their direction screens the grating polarization which in turn follows the polarization direction of the incident light at each instant in time. These local fields induce

oscillations with high damping rates in the charge carriers inside 2DEG. At the resonant frequency of the electron gas, however, they couple to the 2DEG and excite resonant collective oscillations or "2D-plasmons"; in analogy with a classical mass-spring system with an external force. The grating period, therefore, defines the wavevector of the excited plasmons. The resonant plasmon frequencies are determined from this wavevector and the 2D-plasmons dispersion relation. The dispersion relation depends on the 2DEG sheet charge density, which in turn depends linearly on the external gate-voltage [58-59]. This provides a means to not only excite plasmon modes but also to actively tune the absorption resonances.

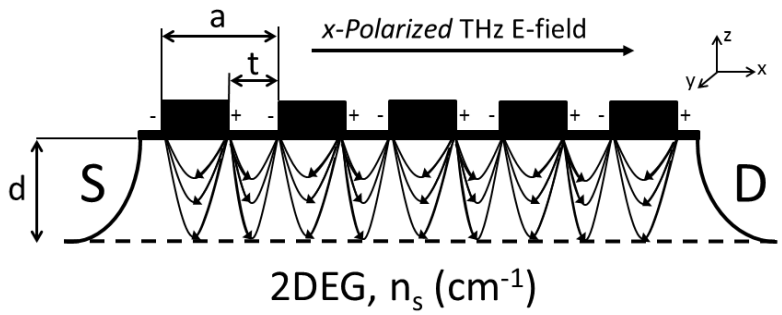

Figure 2: Sketched diagram of the grating-gated HEMT structure with the incident x-polarized free space radiation

Plasmon based HEMTs have potential as fast, chip-scale THz devices and specifically frequency-tunable resonant detectors. The tunable resonant absorption of plasmons in the 2DEG of grating-gated MOSFETs and HEMTs has been reported for a number of material systems which include Si-inversion layers [33-34], GaAs [35-45], GaN- [46-47], InGaAs/InP-[48-54], InGaP-based HEMTs [55], and Graphene [56-57]. This conversion of THz radiation to

plasmons confined on subwavelength structures (~λ/100) may aid in bridging the gap between microwave electronics and infrared photonics[1].

Historically, GaAs-based HEMTs have received particular attention for tunable THz resonant detection [36-41], THz near-field enhancement [45], and THz mixers [43-44]. For detector application, the coupling structures have progressed from simple lamellar gratings [36-38] to split gratings [39], nano log periodic antennas, and hybrid antenna-grating structures [35, 40-42] in this material system to increase responsivity and reduce the noise-equivalent-power (NEP) of the detector.

1.4 InGaAs/InP based HEMTs and their advantage

InP based HEMTs are typically lattice matched molecular beam epitaxially grown InAlAs/InGaAs heterostructures on InP substrate. The quantum well forms at the interface of the InAlAs and InGaAs layers with the conduction band discontinuity (ΔE_c) of ~ 0.51 eV. Figure 3 presents the schematics of the conduction band and Fermi energy level in a double quantum well InGaAs/InP-based HEMT. The two 2DEG layers from in the two interfaces of InAlAs with InGaAs where the conduction band goes below the Fermi level due to the observed ΔE_c.

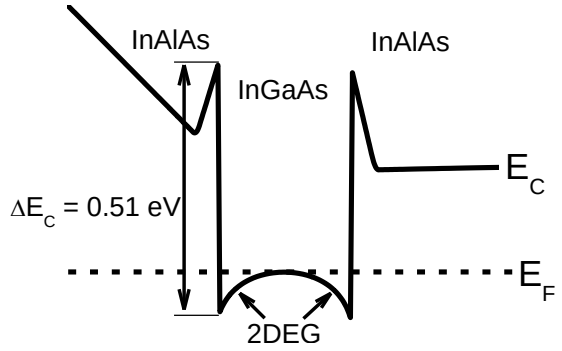

Figure 3: Schematics of the formation of the quantum well at the interface of two InAlAs and InGaAs layers with different bandgaps.

InGaAs/InP materials system [48-49], merits attention due to potentially ~1 to 2 order of magnitude higher sheet charge density and lower electron effective mass when compared with GaAs-based systems. These features would result in stronger plasmon absorption at higher THz frequencies which potentially pushes the above mentioned applications to the higher frequencies of few THz. Furthermore, lattice matched growth of InGaAs/InAlAs heterostructures on InP substrates enables integration with other established InP-based photonics and fast optoelectronic integrated circuits. Although some works report on the electrical effects associated with plasmon modes in 2DEG based transistors [34, 36-41, 48, 51-55], others focus on device absorption properties [33, 46, 49, and 50] where theory adequately describes the spectrum [60-67]. No theory, however, has yet been presented to explain how 2D-plasmons couple to the electrical transport properties of the HEMT.

CHAPTER 2 THEORETICAL CONSIDERATION

2.1 Two dimensional plasmons dispersion

The plasmon wavefunction is proportional to $exp[i(kx-\omega t)]$, where the x axis is the line between source and drain contacts and the wavevector $k = k' + i\,k''$ is complex. The real part k' is the propagation constant, which takes positive or negative values for right (+x) and left (-x) propagating plasmons, respectively. The imaginary part k'' is the attenuation constant. Due to the periodic grating coupler, incident radiation can excite plasmons having only a discrete set of possible k' values, namely $k_n' = 2\pi n/a$, where n is an integer of either sign. The dispersion relation (in SI units) for 2D-plasmons under zero Source-Drain bias is [65],

$$\omega_n^2 = \frac{n_s e^2 k_n'}{m^* \varepsilon_0}[\varepsilon_b + \varepsilon_t coth(k_n' d)]^{-1} \qquad (1)$$

where $\omega_n = 2\pi f_n$ and f_n is the frequency of the n^{th} integer order plasmon, e the electron charge, m^* the effective mass, d the 2DEG depth from the grating, n_s the 2DEG sheet charge density, and ε_t (ε_b) the relative permittivity of the semiconductor layers above (beneath) the 2DEG, respectively.

If the grating-gate is close enough to the 2DEG layer ($k_n'd << 1$), one obtains $Coth[k_n'd] \sim 1/k_n'd$ and the dispersion relation reduces to

$$\omega_n = \sqrt{\frac{e^2 n_s d}{m^* \varepsilon_0 \varepsilon_t}}\, k_n' \qquad (2)$$

In an unbiased device ($V_{SD} \sim 0\ V$) the left and right propagating plasmons are degenerate and their superposition forms 2D-plasmon standing waves. A finite applied V_{SD} causes electron

drift with velocity v_0 and lifts the degeneracy. Then the dispersion for the two different plasmon modes in the applicable limit $k_n'd << 1$ can be written as [67] [APPENDIX A],

$$k_{1,2} = \frac{-\left(\frac{iv_0}{\tau}+2v_0\omega\right)\pm\sqrt{\Delta}}{2\left(4Ad-v_0^2\right)} \quad (3)$$

$$\Delta \equiv -\frac{v_0^2}{\tau^2} + 16Ad\omega^2 \quad (4)$$

where τ is the relaxation time, and $A = n_s e^2/4\varepsilon_t\varepsilon_0 m^*$. In an unbiased device with $v_0 \approx 0$ *m/s*, Eqs. 3 and 4 reduce to Eq. 2 for a gating-gate coupler with Re[k] = k_n'.

For calculations of the plasmon dispersions, the value of n_s is estimated to be [59]

$$n_s = \frac{\varepsilon_t\varepsilon_0}{ed}\left(V_g - V_{th}\right) \quad (5)$$

Where V_g and V_{th} are gate bias and the measured channel depletion threshold voltage, respectively [46]. We determined V_{th} from I-V curves [48] to be -0.85 V ±10% depending on the device and measurement temperature.

Figure 4 presents the calculated dispersion curves from Eqs. 3 and 4 for our sub-THz device with V_g = 0 V, using a, n_s, and τ, values of 9 μm, 1.51×10^{12} cm^{-2}, and 0.25 ps, respectively. Dispersion curves of the unbiased and biased device are shown with black solid and red dashed lines, respectively. For the biased ($V_{SD} \neq 0$ V) device, v_0 was taken to have the value 1×10^5 m/s, and we observe that degeneracy in the dispersion curve is split by 25 GHz at the 207 GHz position of the fundamental, which is indicated by a symbol and an arrow. A

"right" moving plasmon is defined as one propagating in the direction from source to drain. This drift velocity is within the range of the reported saturated values [68-69] [APPENDIX B].

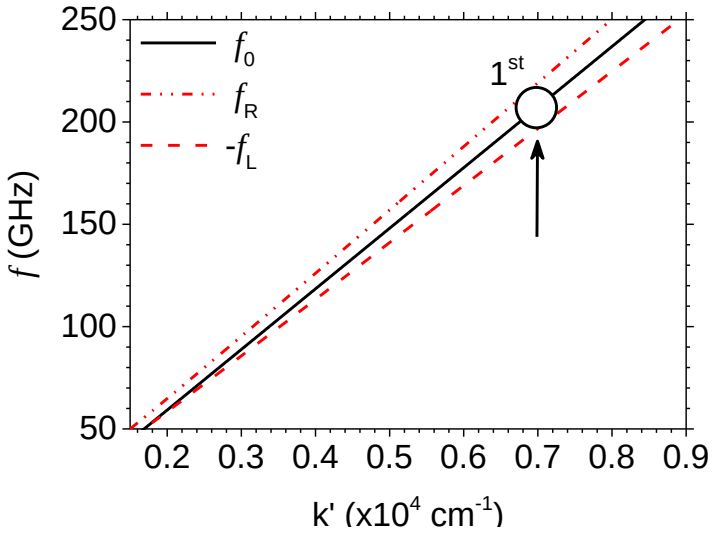

Figure 4 : Calculated dispersion curves of the biased and unbiased device with dashed and solid curves respectively.

Frequency of the fundamental f_1 for sub-THz device (Eqs. 3 and 4) is plotted as a function of sheet charge density, n_s, in figure 5. Corresponding values of V_g are given on the upper horizontal axis, and a vertical arrow gives the position of the fundamental at zero gate bias. Symbols on the V_{SD} = 0 V curve indicate the position of the fundamental for the values of V_g used in our calculations (V_g is a quasi-continuous variable in our experiment ranging in value from –0.50 to +0.85 V) and the arrow indicates the fundamental harmonic for zero gate bias. The meaning of the solid and dashed curves is the same as in Fig. 4. When a Source-Drain bias is applied, the two left and right moving plasmons show two different frequencies of 195 and

220 GHz at V_g = 0 V, respectively, a frequency difference of 25 GHz. This ~ 13% difference is fairly constant over the range of V_g values in the experiment [APPENDIX B].

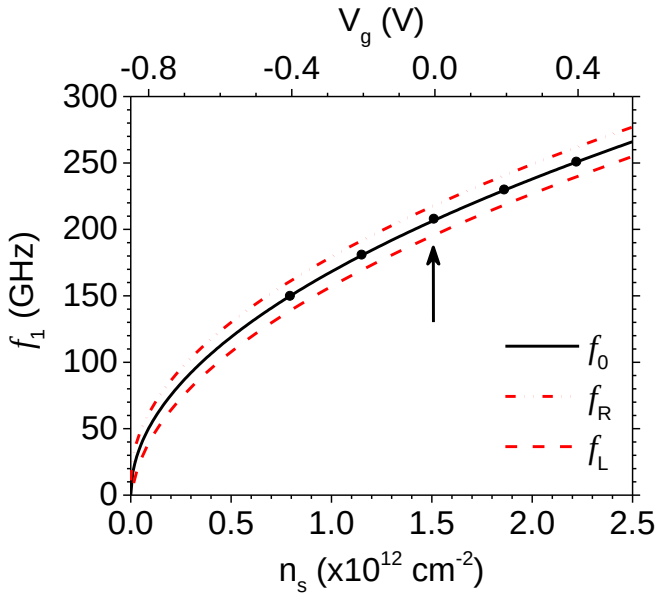

Figure 5: Calculated frequency of 1st-order plasmon of the biased and unbiased device as a function of n_s (V_g) (red dashed and black solid curves, respectively).

2.2 Analysis of transmission spectrum

The transmission spectrum of the plasmon based HEMT can be calculated following the theory of 2D grating couplers [66, 70]. Such spectrum depends on different device parameters such as electron effective mass, m^*, 2DEG depth from the grating, d, grating period and duty cycle, a and t/a, Sheet Charge density, n_s, and 2DEG relaxation time, τ. The analysis of such dependences will help to choose appropriate material system, and to design the appropriate HEMT structure for the frequency range of interest. Moreover, the following analysis will provide us with better understanding of the device behavior when its photoresponse is measured.

Figure 6 presents the effect of different 2DEG depths of 38 and 76 nm. The spectra is calculated for an imaginary InGaAs/InP-based device (m^* = 0.043) with n_s, τ, a, t/a values of 1.51×10^{12} cm^{-2}, 0.25 ps, 0.5 μm, and 0.3 respectively All lines shift to lower frequencies with decreasing depth, which is understood intuitively as being due to the interaction of the plasmon fields with the gate electrons, and therefore increasing the mass involved in the plasma oscillation, in analogy with classical mass-spring system. The stronger interaction with the THz grating polarization also makes the lines deeper, which is a desirable effect [APPENDIX C].

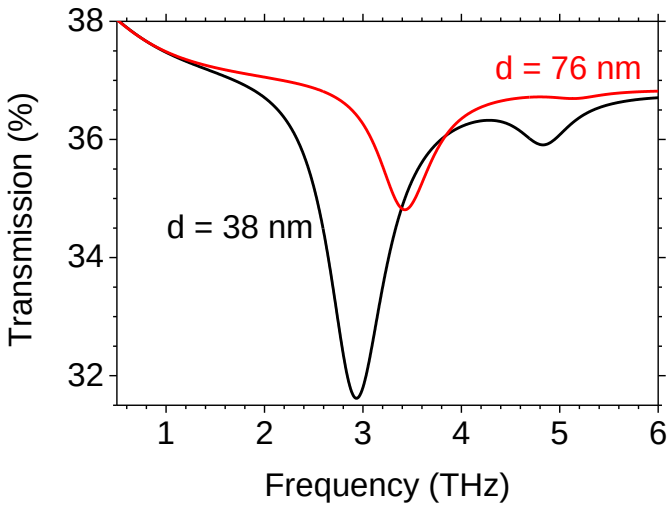

Figure 6: Calculated Plasmon spectrum for a device with two different 2DEG depths as labeled in the graph.

A different electron effective mass is one of the main effects of choosing different material systems. Figure 7 presents the calculated transmission spectra of a device with parameters used in Fig. 6 with 2DEG depth fixed at 38 nm. Two different values of 0.08 and 0.043 are used for effective mass. These values correspond to GaAs- and InGaAs/InP-based material systems, respectively. Plasmon frequencies redshift and absorption deeps become shallower with increasing electron effective mass. These can be explained by using the mass-spring system

analogy: higher electron effective mas will result in increasing the total mass involved in the plasma oscillation which redshifts the oscillation frequency. On the other hand, higher effective mass will increase the inertia involved in oscillations which makes it harder to excite plasmons. This can result in having a shallower absorption feature in the transmission spectrum.

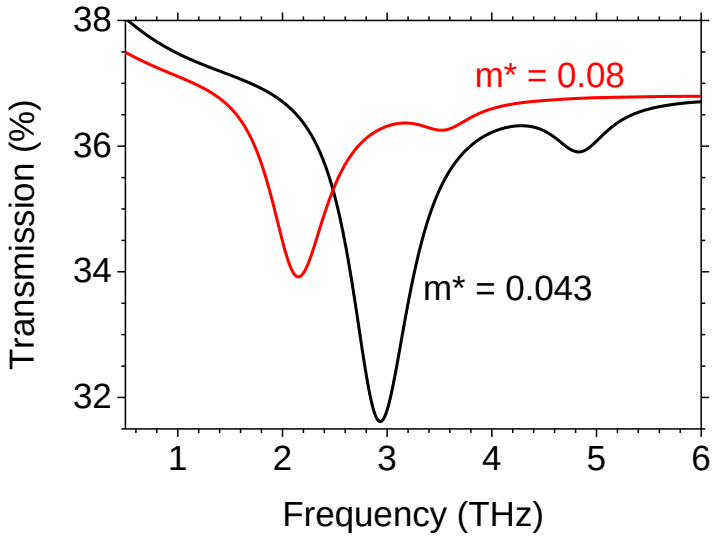

Figure 7: Calculated Plasmon spectrum for a device with two different electron effective masses as labeled in the graph.

Figure 8 presents the results of varying *t*/*a*, for in InGaAs/InP-based device. Parameters used are same as the ones in Fig. 6 but with different grating duty cycles, *t*/a. Smaller *t*/*a* results in lower total transmittance but stronger coupling to plasmons, as evidenced by deeper absorption lines in comparison to the baseline. The lower total transmission is due to the smaller grating openings and increase in reflection by grating metal. Expansion of the curves vertically reveals another feature already reported [71], namely, that the second-order mode disappears when *t*/*a* = 0.5. Note that the position of the resonances is independent of *t*/*a*.

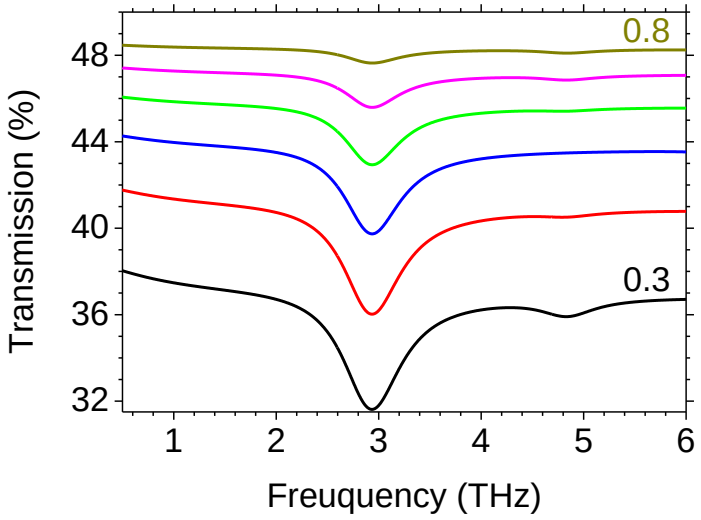

Figure 8: Effect of varying grating gap-to-period ratio *t/a*. The *t/a* values are given above each curve. The extremes of the *t/a* range are indicated next to their corresponding curve, with each neighboring curve differing by *t/a* steps of 0.1.

Next, *t/a* value is fixed at 0.3 and grating period, *a*, is increased from 0.5 to 10 μm with rest of the parameters remaining the same. Calculated transmission spectra are plotted in figure 9. As *a* increases, the resonances shift to lower wavenumber, the separation between first and second resonance decreases until they merge at $a \sim 4$ μm. The lines become deeper, indicating stronger coupling to the plasmons. The redshift in frequencies can be explained by the grating wavevector of $2\pi n/a$. As grating period is increased, the momentum component added to the free space radiation by the corrugated structure is decreased as $1/a$ which results in the coupling to lower energy plasmons. The factor $\omega\tau = 2\pi f\tau$ defines the resolving factor of different plasmon modes for a specific device. For frequencies where $f > 1/2\pi\tau$ (with $f = 0.6$ THz in the calculated device) period of the plasmon oscillations is shorter than the scattering lifetime and therefore

different modes will be resolved. In a frequency regime where $f < 1/2\pi\tau$, however, scattering effects dominate the plasmon oscillations. This results in broadening of resonant features and merging of the different order plasmons.

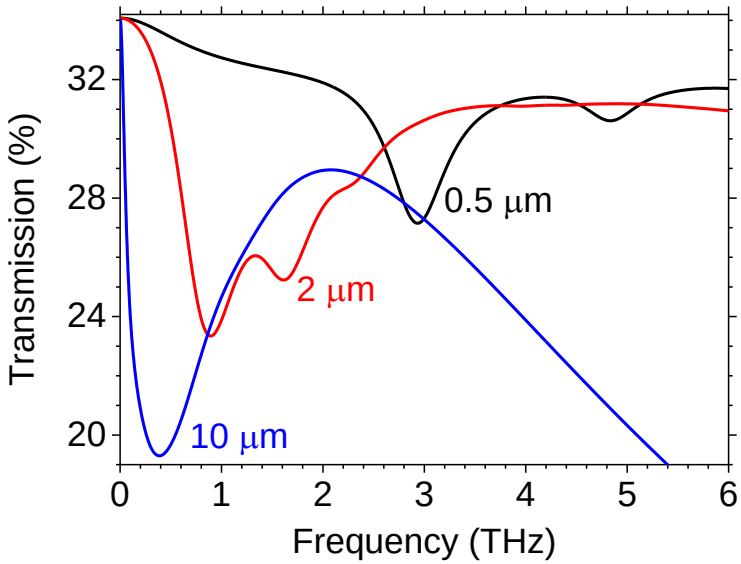

Figure 9: Effect of changing grating period with $t/a = 0.3$. Values of a are given at the side of the corresponding peaks.

Figure 10 presents the calculated transmission of the device for different relaxation time values. In this figure, device parameters are assumed to be the same as in Fig. 9 but with grating period fixed at 9 μm and relaxation time changed from 10 ps to 0.25 ps. Data is plotted for narrower frequency range of up to 1.5 THz for better clarity. For large relaxation times, spectra shows up to 7th-order plasmon mode, however, as relaxation time is decreased, different orders become shallower until they merge and broaden out at $\tau = 0.5$ ps. For $\tau < 0.5$ ps spectra shows one broad resonance at 387 GHz. This resonance is not the 1st-order harmonic and neither the 2nd-order but its transmission minimum is closer to the 2nd-order mode. This broad feature is a

superposition of all the modes due to the small τ value, and its line-shape follows the baseline of the transmission spectra for devices with large relaxation times. This behavior can be also attributed to the decrease in $\omega\tau$ factor at smaller τ values.

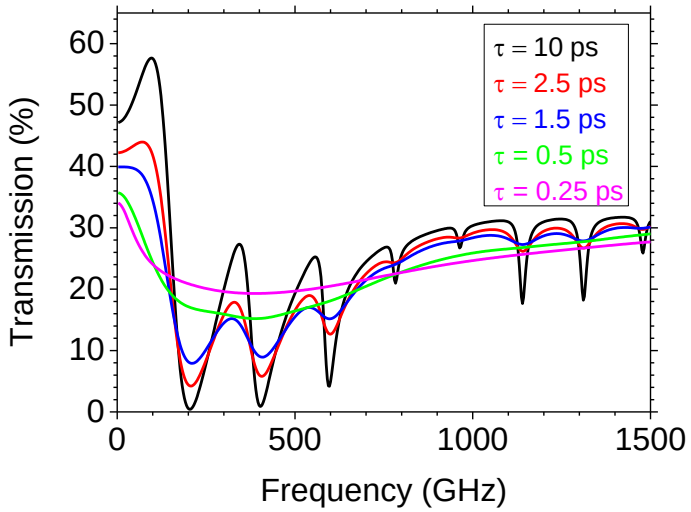

Figure 10: Calculated transmission spectra of an InGaAs/InP-based device with a = 9 μm, t/a = 0.3, and n_s = 1.51×10^{12} cm^{-2} but with different relaxation times as marked in the legend.

Gate-bias is the means of tuning the plasmon resonances by controlling the sheet charge density of the 2DEG. We explore the effect of gate bias on the calculated transmission spectrum in figure. 11. The data is calculated for a device designed to have plasmon resonance at sub-THz frequencies by choosing its grating period, a, to be 9 μm. Other device parameters were chosen to be the same. Sheet charge density, n_s, was calculated for different V_g values from Eq. 5 with V_{th} = -0.85 V, d = 38 nm, and ε_t = ε_{InAlAs} = 12.24. Increasing the negative gate voltage decreases the sheet charge density, which shifts the band to lower wavenumbers while making it shallower as explained by depletion of charge carriers.

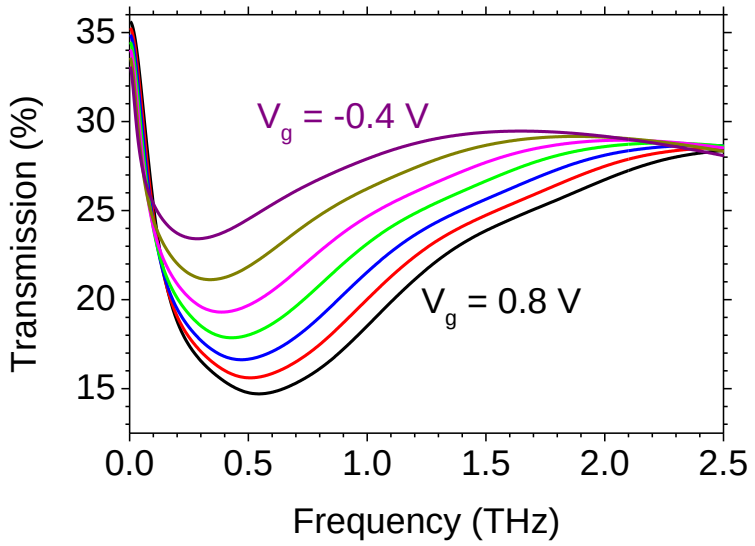

Figure 11: Calculated transmission spectra as a function of gate voltage for a device with a = 10 μm, t/a = 0.3. The extremes of the V_g range are indicated next to their corresponding curve, with each neighboring curve differing by V_g steps of 0.2 V.

2.3 Theoretical considerations for frequency modulation (FM) experiments

During the FM experiments the frequency of the sub-THz source is modulated with amplitude Δf. Source-Drain current I_{SD} is recorded using a lock-in amplifier synchronized with the sub-THz frequency modulation Δf. The lock-in input is the voltage drop V_L across the load R_L and is given by [49, 51-52]

$$V_{out}(V_g, f) = \frac{2}{\pi}\left(\frac{dV_L(V_g,f)}{df}\right)\Delta f \qquad (6)$$

Since the high-impedance lock-in input draws approximately no current, Eq. 2 may be expressed in terms of I_{SD} as

$$V_{out}(V_g, f) = \frac{2}{\pi}\left(\frac{dI_{SD}(v_g,f)}{df}\right)R_L\Delta f \qquad (7)$$

The change dI_{SD} may be written as *d(BWA)*, where *B* is a coupling factor between plasmonic absorption and the change in channel conductance, *W* is the effective radiation power transferred to the 2DEG at each frequency, and *A* is absorbance of the device. This will give

$$V_{out}(V_g, f) = \frac{2}{\pi}\left[\frac{(dBWA)}{df}\right] R_L \Delta f \qquad (8)$$

We assume *B* to be frequency and gate-bias independent. The microwave power inside the waveguide is independent of frequency due to power leveling, but once it leaves the waveguide and is incident on the sample, the value of *W* may vary strongly with wavelength due to interference effects. However, it is assumed that *W* is constant over the small Δf utilized so that there will be no artifacts due to amplitude modulation. The lock-in output is then

$$V_{out}(V_g, f) = \frac{2}{\pi} BW \left(\frac{dA(V_g,f)}{df}\right) R_L \Delta f \qquad (9)$$

Assuming constant front surface reflectance *R*, we obtain absorbance as $A = 1-R-T$ and therefore $dA/df = - dT/df$. Figure 12 presents dT/df from the transmittance spectra calculated in Fig. 11. Calculated spectra are shown for the frequencies up to 120 GHz. A record of lock-in output for different gate voltages produces a set of points corresponding to a vertical slice through the calculated curves in Fig. 12. By choosing different center frequencies, we are able to reproduce the complete curves shown in Fig. 12 over the frequency range accessible to our radiation sources. Those ranges are indicated in the figure with two bars.

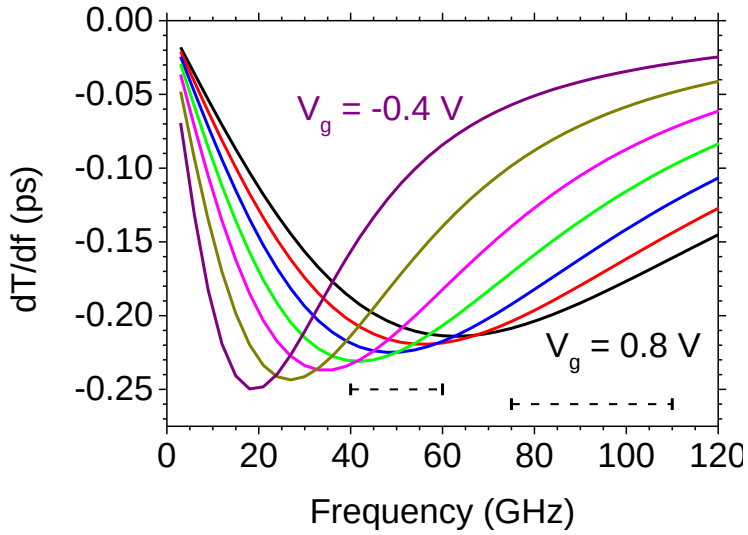

Figure 12: Calculated dT/df spectra of a device with a = 9 μm, and t/a=0.3. The extremes of the V_g range are indicated next to their corresponding curve, with each curve differing from its neighbors by 0.2 V. Horizontal bars indicate our range sources.

CHAPTER 3 EXPERIMENT

3.1 Fabrication of the HEMTs

The devices were fabricated from a molecular-beam-epitaxial grown, InGaAs/InP HEMT heterostructure with two δ-doped layers (Table 1). This will assist in the formation of two quantum wells at the two interfaces $In_{0.68}Ga_{0.32}As$ channel with $In_{0.52}Al_{0.48}As$ as shown in Fig. 3. The δ-doping, instead of a thick doped layer, was chosen to avoid formation of the parasitic or "virtual" gate [70, 72-73]. The detailed layer structure of the MBE grown heterostructure is presented in table 2. Using this device structure, the doping level of different layers is calculated by Silvaco Atlas finite element method simulation software. Such calculations are overlapped with device structure and presented in figure 13. The two 2DEG layers are marked with the two arrows. These two layers of highly concentrated 2D electrons are ~20 nm apart and have 5-6 orders of magnitude higher charge densities when compared with their neighboring layers.

Table 2: MBE grown epilayer structure used for fabrication of the HEMT

75 Å n^+-$In_{0.6}Ga_{0.4}As$ 6.0×10^{18} cm^{-3} Cap Layer
350 Å $In_{0.52}Al_{0.48}As$ Undoped
Si δ-doping layer 4×10^{12} cm^{-2}
30 Å $In_{0.52}Al_{0.48}As$ Undoped Spacer
200 Å $In_{0.68}Ga_{0.32}As$ Channel
30 Å $In_{0.52}Al_{0.48}As$ Undoped Spacer
Si δ-doping layer 4×10^{12} cm^{-2}
3000 Å $In_{0.52}Al_{0.48}As$ Buffer
InP Substrate

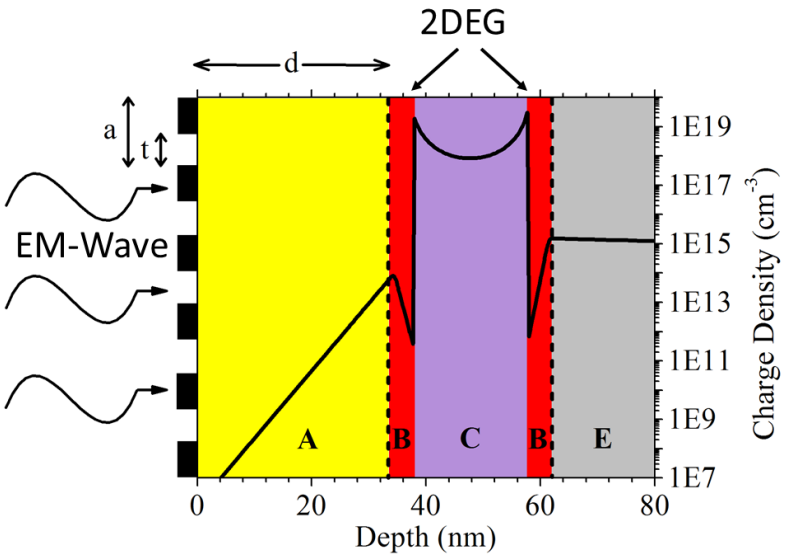

Figure 13: The epitaxially-grown materials are indicated as A = $In_{0.48}Al_{0.52}As$ with δ-doping at the interface with B, B = undoped $In_{0.48}Al_{0.52}As$ spacer, C = $In_{0.32}Ga_{0.68}As$ channel and E = $In_{0.48}Al_{0.52}As$ buffer layer. Radiation is incident on the grating-gate from the left. The black curve indicates the charge density distribution.

Device fabrication first involved etching of the active layers into mesas for electrical isolation. This was followed by the patterning and deposition of electron-beam evaporated Ti/Au (500nm/2500nm) metal pads, subsequently rapid thermal annealed to form ohmic source and drain contacts. Gates were formed by first removing the doped-InGaAs cap layer that facilitated source and drain ohmic contact formation. A 20 nm layer of Ti was then deposited on the 195 µm × 250 µm gate region to act as a semitransparent gate metal to allow uniform gate-bias control of the 2DEG sheet charge concentration. The gratings, with periods a = 0.5 and 9 µm were patterned over the semi-transparent gate by optical and e-beam lithography, respectively. The duty cycles were chosen to be 0.22 and 0.8 for large and small period gratings. The grating bars were formed by depositing e-beam evaporation of stacks of Ti/Au (15 nm/100

nm). This would position the top 2DEG layer at 38 nm beneath the gate gratings, having d = 38 nm. Source, gate, and drain bond pads were fabricated by photolithography using Ti/Au (50 nm/250 nm). The sub-THz sample was mounted in a TO-5 transistor package with cap removed. The THz sample was mounted on a modified TO-5 housing to have a hole aligned with the gate region of the transistor so that there can be no transmission of THz light except through the gate region. An optical microscope image of the sub-THz device is presented in figure 14 while THz-device with smaller grating period is shown in figure 15.

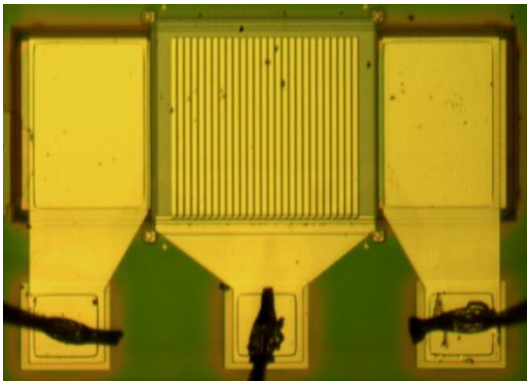

Figure 14: Optical microscope image of our sub-THz grating gated InP-based HEMT.

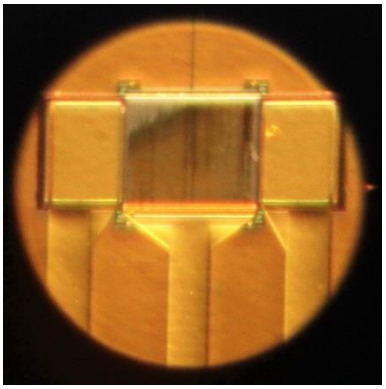

Figure 15: Optical microscope image of our THz HEMT.

3.2 Electrical characterization of the HEMTs

The I-V characteristic of the HEMT device was measured at different sample temperatures to determine the sheet charge density and relaxation time values. For the I-V measurements Drain of the device was grounded while Source and Gate were biased relative to the ground. I-V curves were measured for different V_g values with V_g step size of 0.1 V. Applied Source-Drain voltage, V_{SD}, was swept from 0 to 2.5 V for each of the Gate voltages and the Source-Drain current, I_{SD} was recorded. All the biasing was done with two Keithley 2400 Source meter units.

3.3 Experimental setups for characterization of the sub-THz device

3.3.1 Backward wave oscillators

Backward wave oscillator (BWO) is a radiation source designed to convert the energy of an electron beam to Sub-THz and THz range electromagnetic (EM) waves. They can provide radiation powers up to 100 milliwatts (mW) and frequencies from 1 GHz to 1.5 THz with different vacuum tubes. These sources provide a huge tunability range that can give benefits over conventional single line sources. A BWO consists of a vacuum tube with an electron gun and a slow-wave structure. Slow wave structure is a circuit where the phase velocity of the electromagnetic wave is much smaller than the speed of light. For instance, it can be a helix where the speed reduction factor is the ratio of the pitch of the helix to its circumference. In such a circuit, electromagnetic waves can be matched to a slower moving electron beam to form

oscillating electron bunches as similar to travelling-wave tubes that are used to amplify RF signals.

In a BWO, a linearly moving electron beam, generated by an electron gun, is accelerated to the collector at the other side of the tube. The beam is radially confined by a magnetic field around the vacuum tube. Propagating along the axis of the cylindrical tube, electron beam passes through a resonant cavity containing a slow-wave circuit. Such a cavity provides a set of electromagnetic modes that propagate along and in the opposite direction to the electron beam with a phase velocity matching the speed of electrons. These propagating slow modes interact with the negatively energetic electron beam and cause oscillating electron bunches that radiate electromagnetic (EM) waves in GHz and THz frequencies [74]. Generated EM-wave out-couples to the output of the tube using a directional coupler close to the cathode of the electron gun. The backward wave oscillators are so named due to the negative group velocity of the cavity modes involved in the interaction and therefore their energy transfer is backwards along the electron beam. This can also be explained by the opposite direction of cavity modes Poynting vector relative to the velocity vector of the electron beam [74].

The operating frequency of a BWO can be tuned by changing the cathode voltage of the electron gun. An increase in the cathode voltage increases the speed of the propagating electrons and therefore decreases the transit time of the electrons through the cavity and, consequently, shortens the period (increase the frequency) of the generated oscillations.

The BWO used in this work had two operating frequency ranges of 40-60 GHz and 75-110 GHz. The BWO power supply had a feedback loop serving as a power leveling circuit by using the output of a crystal detector that was monitoring the radiation as the feedback input.

3.3.2 Cryogenic temperatures and closed cycle Helium cryostat

The HEMT device was fixed to the cold copper plate of a Janis SHI-4 closed cycle cryostat. The closed cycle cooler was able to reach temperatures as low as 4 K in 45 minutes. At the end of the vacuum jacket was installed a polyethylene (PE) vacuum window, which allows Sub-THz radiation to pass into the cryostat and irradiate the device.

To control the temperature of the sample, a silicon diode temperature sensor was thermally contacted to the copper below the device and connected to a Lakeshore Cryotronics Inc. 331S temperature controller. The temperature controller applied current to a 50 ohm heater wire glued around the second stage of the cryostat. The heater was formed by wrapping 50 ft of Nichrome heating wire around the cylindrical second stage. This wire has a layer of polyimide insulation around it which allows it to tolerate local temperatures as high as 500 K. The heating power was up to 50 W. This wire was fixed to the copper body with a layer of VGE-7031 varnish which can tolerate temperatures up to 470 K for up to 2 hours. Figure 16 presents a photo of the device mounted inside the cryostat. The three Source, Drain, and Gate contacts of the device are visible. Locations of the HEMT device and the Si diode are marked with the red arrows and labeled accordingly.

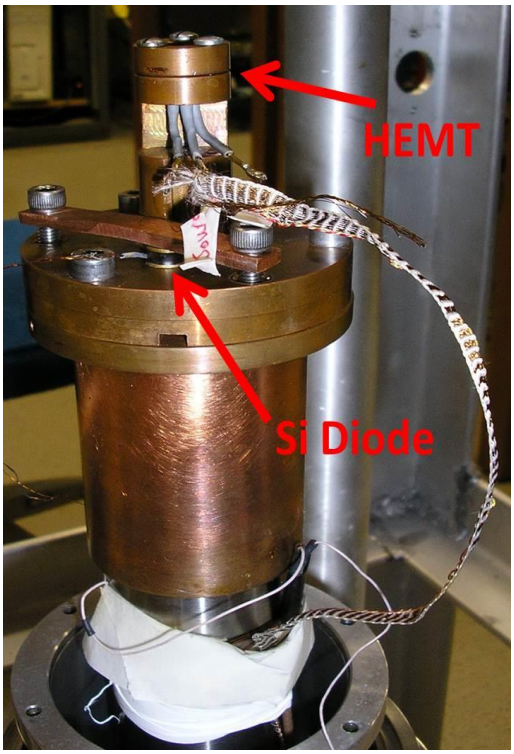

Figure 16: A photo of the HEMT device mounted inside the Janis SHI-4 cryostat

3.3.3 Frequency modulation setup for photoresponse measurement

Figure 17 presents a schematic of the FM experiment. A 100 Hz sine wave with adjustable DC offset was used to modulate the BWO frequency around a central value set by the offset. Moreover, adjusting the DC offset enabled us to sweep the applied Cathode voltage and consequently the output frequency of the BWO. The modulation amplitude was 100 MHz, or ~ 0.1% of the central frequency. The same control signal was high-pass filtered and amplified for the lock-in reference. A crystal detector connected via a 10 dB directional coupler monitored the sub-THz power, and this signal was used for power leveling the BWO.

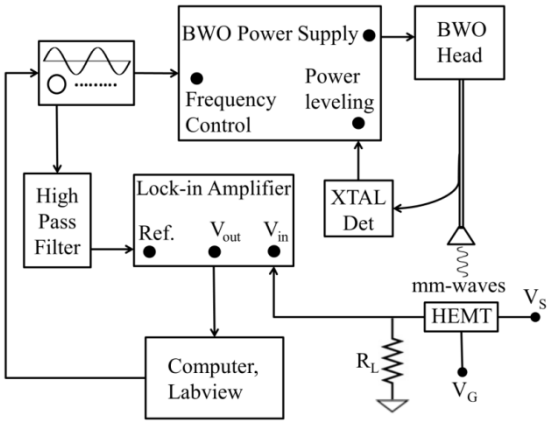

Figure 17: Schematic of the frequency modulation experimental setup

The radiations from the BWO were covering two frequency ranges of 40-60 GHz and 83-108 GHz by adjusting the DC offset of deriving sine wave in the ranges of 0.5-3.7 V and 1.17-3.4 V, respectively. Sub-THz waves were then conducted to the cryostat with rectangular waveguides and a polarization-preserving horn. The radiation power was kept constant over each of the ranges by the power leveling circuit. Separate sets of WR-19 and WR-10 waveguide components were used for these two frequency ranges, respectively. These waveguide sets differ from each other in size and are specifically designed to have the maximum coupling to the sub-THz waves of each frequency range. After exiting the gain horn, the radiation passed through a PE window into the vacuum of the cryostat to irradiate the device. The BWO head could be rotated about the optical axis to study polarization effects. During measurements, a constant 0.5 V was applied to the source while the gate was biased at 0, -0.1 and -0.2 V, all with respect to ground, with the drain connected to ground via a 100 Ω load. Figure 18 presents a photo of the setup in FM experiments.

Figure 18 : Top view image of the FM measurements setup.

3.3.4 Polarization Check experiments

An experimental setup was designed to test the effect of scattering of sub-THz radiation from Polyethylene cryostat window and reflection from different metal surfaces on radiation polarization. The setup was consisted of two gain horns placed in front of each other that are referred to as the emitting and collecting horns, respectively. The emitted sub-THz radiation generated by the BWO exits the emitting horn and propagates through free space before being collected by the collecting horn for detection by a crystal detector. The emitting horn was fixed throughout the experiment with a vertical polarization axis. The collecting horn was rotatable about the optical axis so that its polarization axis could be either horizontal or vertical. When two horns have matching polarization axes; the radiation will be collected by the collecting horn and detected by the crystal detector. This was confirmed by placing a wiregrid polarizer in the beam path. If their polarization axes are perpendicular to each other, however, the polarization

of the emitted beam won't match that of the collecting horn and therefore no radiation will be detected at the crystal detector unless scattering off or reflection from an object in the beam path changes the polarization of the incoming light. Figures 19 and 20 present pictures of the experimental setup when polarization axes of the two horns are parallel and perpendicular, respectively.

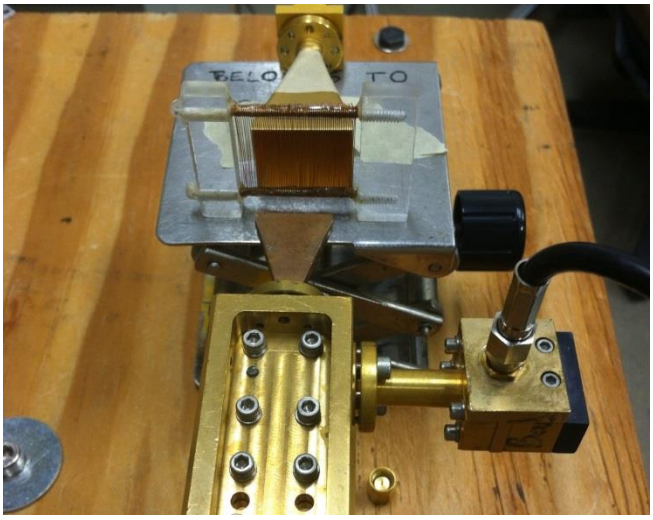

Figure 19: Image of the experimental setup with polarization axes of two horns parallel.

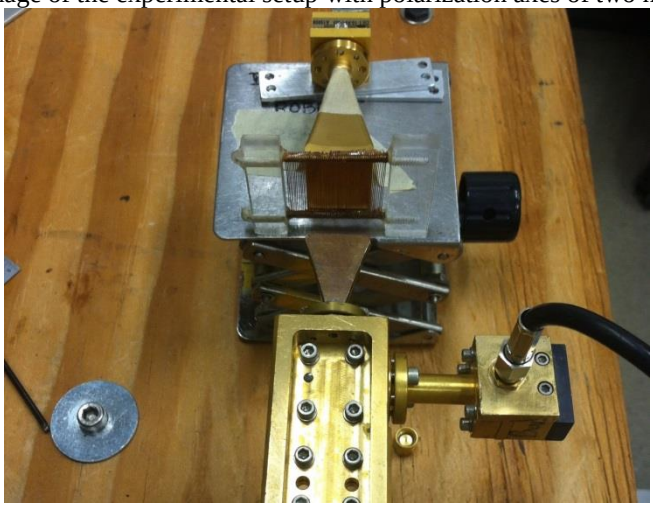

Figure 20: Image of the experimental setup with polarization axes of two horns perpendicular.

3.3.5 Amplitude modulation setup for photoresponse measurement

In AM experiment, the device was mounted in the Janis closed cycle cryostat at. Radiation generated by a backward wave oscillator (BWO) at 77 or 106 GHz was guided into the cryostat via a rectangular waveguide vacuum-sealed at a standard waveguide junction by a rubber o-ring with a 3-μm-thick sheet of mylar. This reduced standing wave interferences and polarization scrambling in comparison to other measurements with frequency modulation by having the output of the polarization-preserving horn separated from the device by just 7 mm with no intervening window. Figure 21 presents a top-view image of the experimental setup. The waveguide structure coupled to the cryostat through is visible. The red arrow points to the o-ring sealed waveguide port and the location of the Mylar sheet.

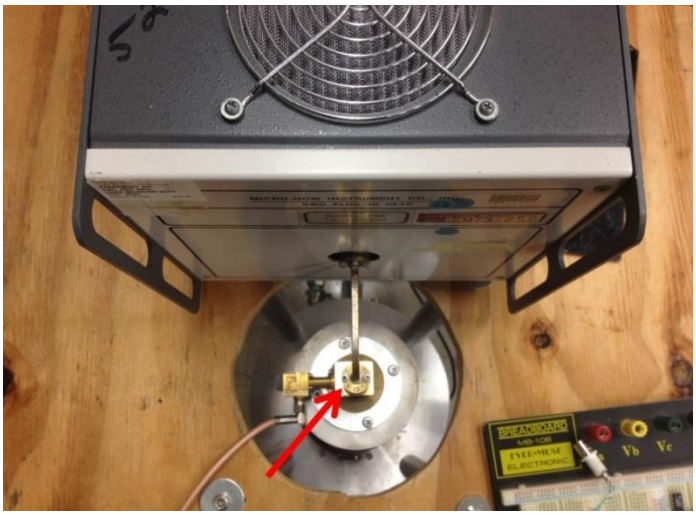

Figure 21: Top view image of the AM measurements setup.

The incident radiation, electronically amplitude modulated at 512 Hz, was monitored by a crystal detector via a 10 dB directional coupler (Fig. 21). The detector signal was high-pass

filtered and amplified to serve as the lock-in reference. Constant voltages of 0, 0.25, or 0.5 V were applied to the source while the drain was connected to ground via a 100 Ω load. The voltage on the grating-gate (V_g) was stepped from -0.5 to 0.8 V with respect to ground in increments of 10 mV. The voltage across the load resistor was input to the lock-in for synchronous detection of the photoresponse. A diagram of the experimental setup is presented in figure 22.

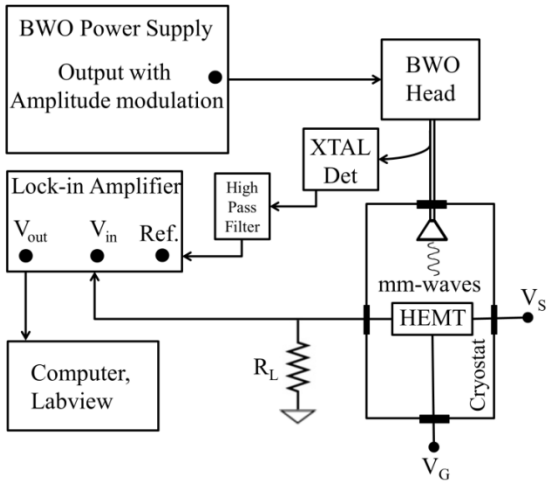

Figure 22: Schematic of the amplitude modulation experimental setup.

3.4 Experimental setups for characterization of the THz device

3.4.1 Bomem DA8 FTIR setup for THz plasmonic transmission spectra

Transmission spectra through the gate region of the device were measured at 4 K sample temperature using a Bomem DA8 Fourier spectrometer with a Globar source, 12 and 25 micron Mylar pellicle beamsplitters and a liquid-He cooled Si-bolometer. In this case, the sample was mounted upside down on the light cone inside the bolometer using rubber cement, similar to the

experimental procedure outlined in [47]. In this configuration, pictured in figure 23, unpolarized far-IR light first passed through the substrate of the HEMT exiting through the grating-gate before being collected by the bolometer. The plasmon-exciting local fields due to polarization of the grating bars induced by the incident THz field are still expected in this case. During these measurements, a negative gate bias was applied to the gate with the source and drain grounded in order to observe any sheet charge dependent resonant effects.

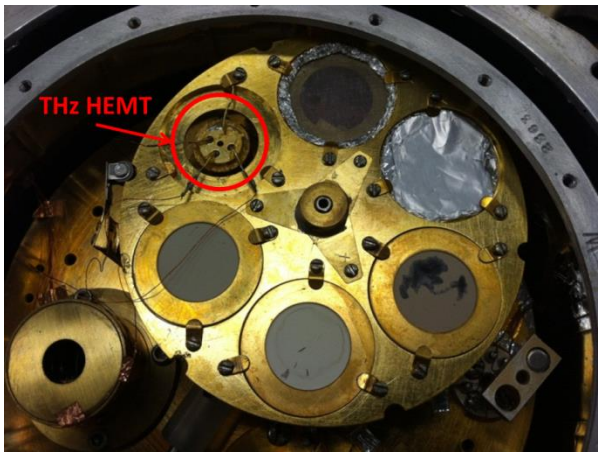

Figure 23: A picture of the InP HEMT device mounted with grating facing the bolometer collection cone for 4 K measurements using Bomem DA8 FTIR spectrometer.

3.4.2 Bruker 80v FTIR spectrometer integrated with Hyperion 1000 IR microscope

The THz device was mounted inside a Janis ST-500 continuous flow liquid-helium cryostat and was oriented so that unpolarized IR-radiation hit the grating before passing through the layered structure of HEMT. Sample temperature was monitored by a Si diode temperature sensor and stabilized at 20 K with a Lake Shore Cryogenics 331 temperature controller. The cryostat was fixed to an optical stage and placed in the beam path of the Bruker Hyperion 1000 IR-microscope integrated with a Bruker 80v Fourier transform infrared (FTIR) spectrometer.

The Far-IR radiation of FTIR's globar lamp entered the microscope through a side polyethylene window. A 15x reflective condenser lens were used to focus the beam on the sample. Focused beam would hit the grating, pass through the device, and then collected and collimated by a 15x reflective objective on top of the cryostat. The transmitted beam was then detected using a helium-cooled Si-bolometer interfaced with the system. The entire microscope setup was purged by dry N_2 to reduce atmospheric absorption lines in THz region. During the measurements Source and Drain of transistor were grounded while Gate was biased in range of V_g = -0.2 V to 0.2 V with the voltage step size of 0.1 V to tune the possible plasmon absorption lines. Figure 24 presents a picture of the device mounted inside the cryostat while the complete experimental setup is shown in figure 25.

Figure 24:A picture of the HEMT device mounted inside the cryostat and oriented so that IR-radiation was passing through the grating first.

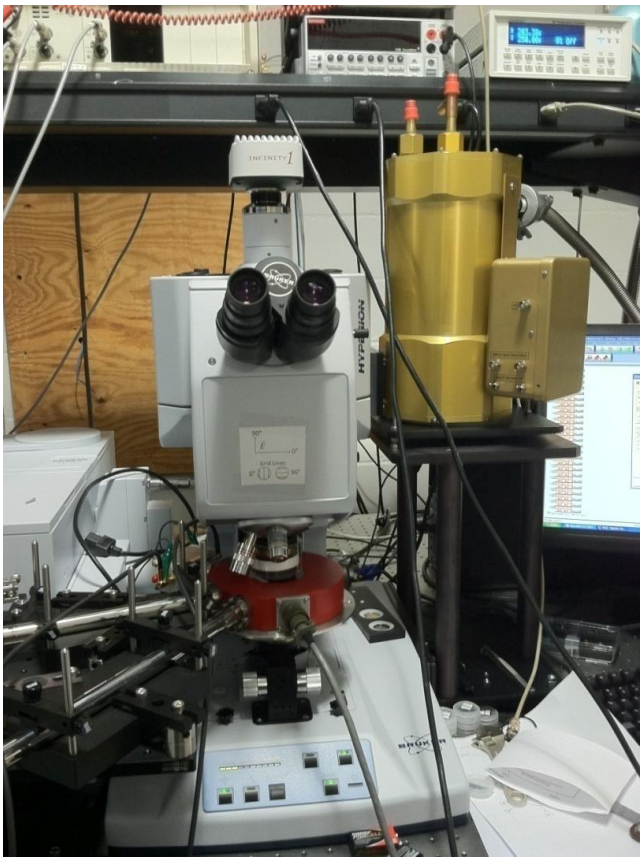

Figure 25: A picture of the experimental setup with FTIR spectrometer on left, IR-microscope with the interfaced Si-bolometer at center and cryostat mounted on a stage and placed in the beam path.

CHAPTER 4 RESULTS AND DISCUSSION

4.1 Sub-THz HEMT Device

4.1.1 Results of frequency modulation experiment

Source-Drain I-V curves of the HEMT were measured for different of gate-biases and two different sample temperatures of 295 K and 4 K in order to determine n_s and τ of the device. Data was taken for V_g between 0 to -0.5 V with steps size of -0.1 V and are presented in figure 26. Source-Drain current, I_{SD}, saturates to different levels which decrease with increasing negative gate bias until the HEMT reaches pinch off. Measured I_{SD} saturates at higher values for each gate voltage when sample is at 4 K. This can be attributed to the reduced scattering and therefore higher mobility when sample is cooled.

The saturation current, $I_{sd,sat}$, data are plotted in figure 27 as a function of gate voltage. In this figure, data for 295 K and 4 K sample temperatures are plotted with black and red colored symbols, respectively. The black and red curves are fits of formulas from [59] to the data. The fit parameters, namely initial doping of the δ-doped layers and mobility, allow determination of relaxation time and sheet charge densities at each applied V_g.

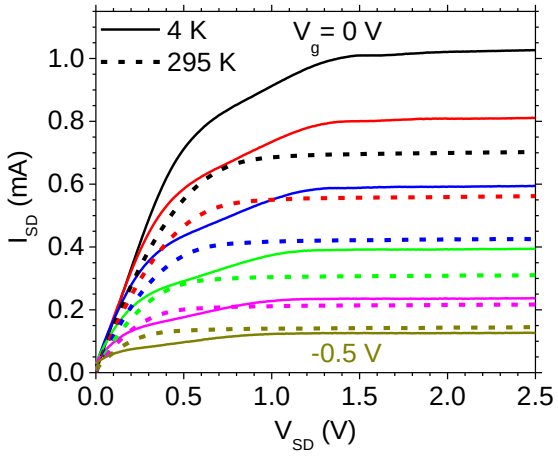

Figure 26: Measured I-V Curves of the device at T = 295 K and 4 K

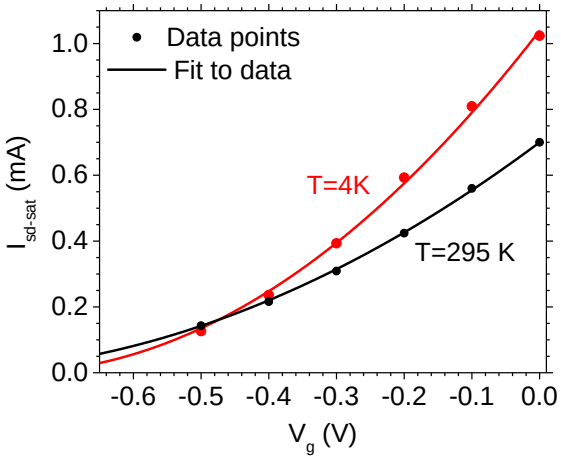

Figure 27: $I_{sd\text{-}sat}$ vs V_g data (symbols) and fits (lines) for the two measurement temperatures of 295 K and 4 K

Table 3 presents the values of μ, τ, n_d, and n_s at V_g = 0 V at the two temperatures. Relaxation time, τ, is calculated from the fitted mobility by $\tau = m^* \mu / e$ and n_s is calculated from Eq. 5 with n_d related to the Threshold voltage by $V_{th} = \phi_b - E_c - e n_d d / \varepsilon_t \varepsilon_0$. Mobility and therefore relaxation time of the transistor increases with decreasing temperature as expected. Moreover

the sheet charge density of 2DEG is decreasing at lower temperature due to the freezing of some of the charge carriers at low temperatures.

Table 3: Values of mobility, relaxation time, initial doping, threshold voltage, and sheet charge density of sub-THz device for V_g = 0 V at 295 and 4 K.

T (K)	**μ (cm^2/V.s)**	**τ (ps)**	**n_d (cm^{-2})**	**V_{th} (V)**	**n_s (V_g = 0) (cm^{-2})**
295	7760	0.19	1.65×10^{12}	-0.90	1.61×10^{12}
4	15300	0.37	1.44×10^{12}	-0.81	1.39×10^{12}

Figure 28 (a) presents calculated absorption spectra for the device at time of FM experiments at 4 K sample temperature for frequencies up to 400 GHz. Data are plotted for the experimental gate-biases of 0, -0.1, and -0.2 V. The figure includes only the low frequency portion of the broad plasmon resonance bands, whose peaks occur at 365, 340, and 320 GHz as indicated by triangle symbols above the respective curves. These broad bands are the superposition of different order plasmonic modes due to the small τ value of the device; this behavior is explained in detail with Fig. 10 in theory section. The BWO ranges (Fig.28-b) lie at frequencies where the absorptance curves are 35 and 65% of the maximum value, so that our experimental wavelengths are within the plasmon resonance absorption bandwidth.

From Eq. 9, the lock-in output is proportional to *dA/df*, whose spectrum is presented in figure 28 (b) with the ranges of the available BWOs indicated. Maxima of plasmon absorption bands are marked by triangle symbols, where the derivatives are zero. From these curves, we expect the response to decrease with increasing frequency.

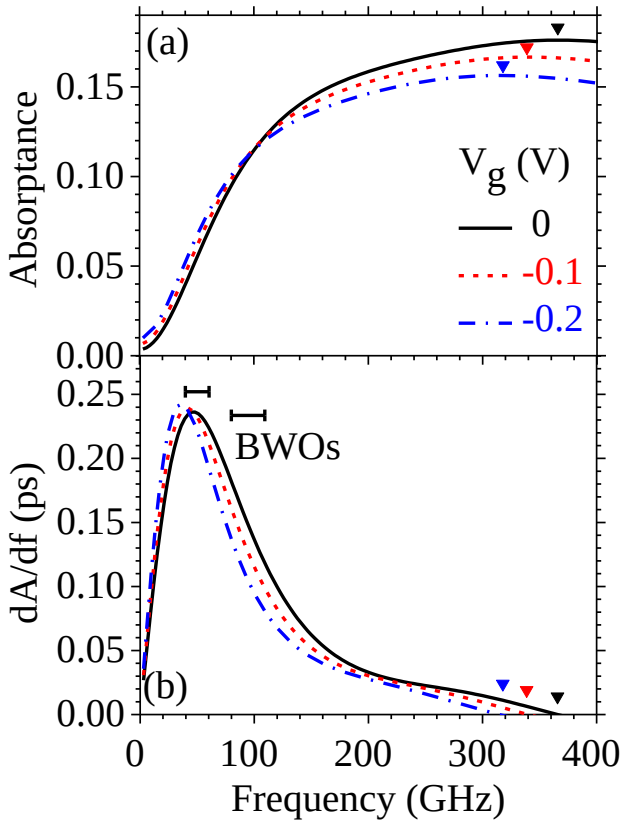

Figure 28: Calculated absorptance spectra. Absorptance maxima are marked by symbols. (b) Calculated *dA/df* spectra. The horizontal bars indicate the available BWO ranges.

First, radiation power of the BWO was measured with a crystal detector in place of the horn to better characterize incident sub-THz waves. The crystal detector outputs are presented in figure 29 for the frequency ranges of 40-60 GHz and 83-108 GHz with black and red curves, respectively. Data was measured with the power leveling circuit on. Although the measure output for the 40-60 GHz frequency is relatively flat at 2.1 V, it experiences a steady decrease with increasing wavelength in the high frequency range. The sensitivity of the crystal detectors used in power measurements were 800 (1000) mV/mW for the low (high) frequency range.

Using these sensitivity values the radiation powers at the location of the gain horns is derived as 2.6 and 1.7 mW for low and high frequency ranges, respectively. The reported value for 83-108 GHz range is calculated based on the average output of the crystal detector at 96 GHz.

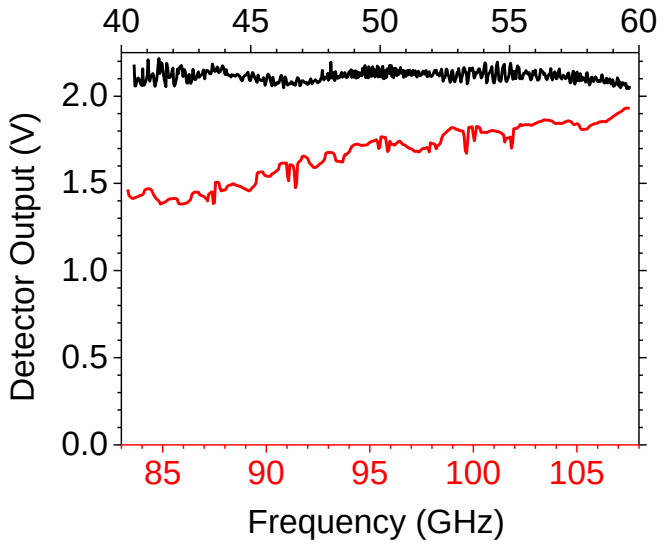

Figure 29: Outputs of the crystal detectors for the two frequency ranges of the experiment.

As described in section 2.5, during the experiment sub-THz radiation was divided into two paths by a directional coupler. The beams entering the side and main outputs were passed through 90 degree bend waveguides with radii r_1 and r_2 before being used to level the radiation power and being directed into the cryostat, respectively (figure 30).

The power leveling was performed using a crystal detector mounted at the 10 dB side output of a directional coupler (DR). As shown in figure 30, sub-THz beam entering this output would pass through an internal DR 90 degree bend waveguide with radius r_1 before entering the detector. On the other hand, in the main output a 90 degree bend waveguide with radius r_2 was

necessary to couple the radiation to the upward-looking cryostat (Fig 18). Replacing the gain horn at the end of this bend with a crystal detector (Fig. 30) allows comparison of the power spectra measured at the two locations, as shown in figure 31.

The results are that the power at the directional coupler is fairly flat and stable; however, the power at the position of the horn shows larger fluctuations. In the low frequency region, the power at the horn is at least fairly flat, but in the high frequency region, there is a clear increase with frequency. This can be attributed to two factors, namely, the radius mismatch between the two bend waveguides at the two ends of the direction coupler in the high frequency range waveguide set (WR-10 band) and additional losses and scattering at the longer wavelengths in the bent portion of the waveguide.

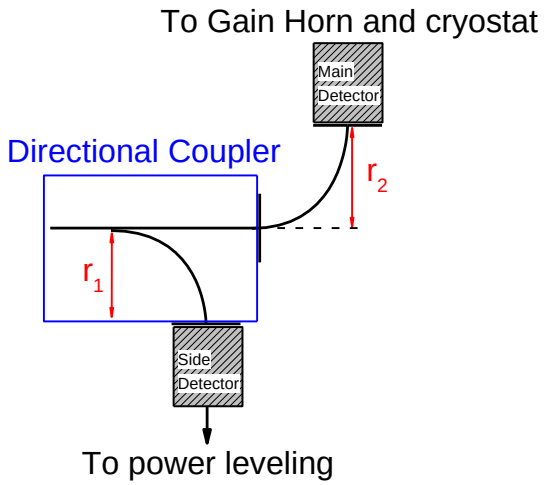

Figure 30: Schematic of the experimental setup used to record radiation power of at outputs of directional coupler.

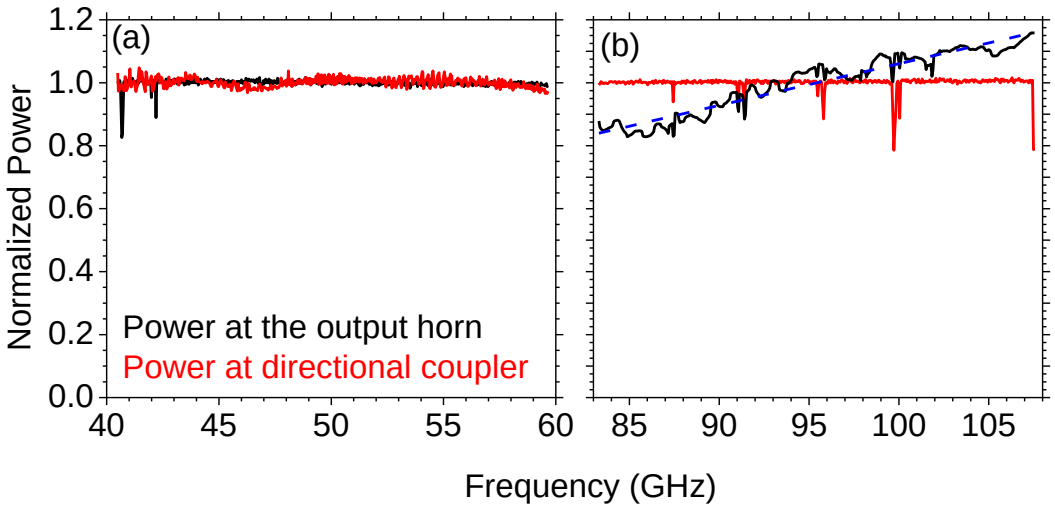

Figure 31: Radiation power collected at the directional coupler and output horn for the frequency range **(a)** 40-60 GHz **(b)** 83-108 GHz. Powers are normalized for comparison.

The measured photoresponse of the device is shown in figure 32 for gate-biases of 0, -0.1, and -0.2 V as black, red, and blue curves, respectively. The effect was measured over the full 40-60 GHz and 83-108 GHz ranges, but only a portion of each measured spectrum, and only the nominal perpendicular polarization data (inset schematic), are presented. The detected photoresponse shows sharp features at discrete frequencies as opposed to the continuous electrical response expected from Fig. 28 and Eq. 9. This is explained by interference and the formation of standing waves, which is a well-known experimental artifact in sub-THz spectroscopy. When standing wave nodes occur at the grating no plasmons can be excited, and hence there can be no electrical response. At frequencies where anti-nodes occur, excitation of plasmons and a corresponding electrical response may occur. Although the known standing wave phenomenon somewhat obscures the results, it is clear each individual peak weakens with

increasing negative gate bias suggesting reduced plasmon interactions with the decreasing 2DEG sheet charge as expected. The noise of the system was measured by blocking the radiation and recording the lock-in output, and its root-mean-square (RMS) value was determined to be ~ 45 nV.

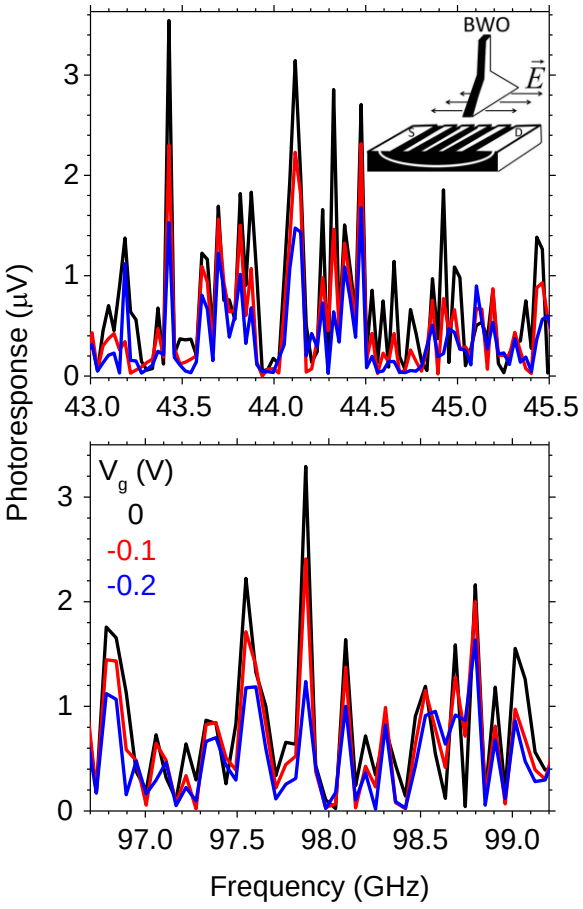

Figure 32: Photoresponse of the HEMT at T = 4 K to Sub-THz radiation for three gate biases. Data are for nominal perpendicular polarization as expected from the horn orientation (inset schematic).

Although the response for parallel polarization is expected to be zero since it should fail to polarize the grating and produce plasmon-exciting local fields, a similar but weaker response

was in fact observed for this nominal polarization. Figure 33 presents such a photoresponse in the same frequency ranges as in Fig. 32. While most of the photoresponse peaks in Fig 32 are measured to be above 2 μV, they drop to values smaller than 1.8 μV at measured data for nominal parallel polarization.

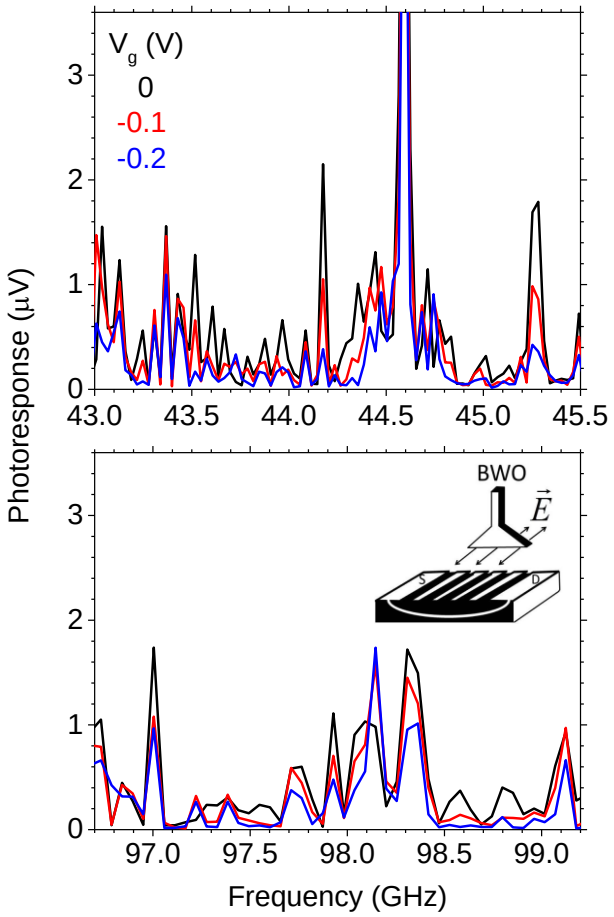

Figure 33: Photoresponse of the HEMT at T = 4. Data are for nominal parallel polarization as expected from the horn orientation (inset schematic).

The presence of such electrical effect for radiation with wrong polarization forced us to investigate the actual polarization state of the incident light when it reaches the sample using the

experimental setup explained in section 2.6. Figure 34 (a) presents the radiation spectral intensity recorded by a crystal detector when the polarization axes of emitting and collecting horns are aligned parallel for optimum collection. When a wire grid polarizer is placed in the radiation path with wires oriented perpendicular to the beam polarization, the beam is unaffected as anticipated. When the polarizer is rotated 90 degrees, the beam is strongly blocked, also as anticipated to be due to absorption by polarizer's wire grids.

Figure 34 (b) presents the recorded intensity when the collecting horn is rotated 90 degrees. In such orientation no radiation intensity should be recorded due to the polarization mismatch of the two gain horns, and in fact and a poor radiation is detected. When the polyethylene cryostat window [51] is placed between the crossed horns, however, a jump in the signal is observed at the higher frequencies. This is attributed to rotation of the polarization by some small angle due to scattering from imperfections in or on the window. A mass of randomly oriented wires produces an even stronger response, suggesting that random reflections from metal surfaces inside the cryostat may also serve to randomly alter the incident polarization. These studies simply confirm that the well-known possible change of polarization angle on reflection or refraction [75] is likely occurring in our experiment.

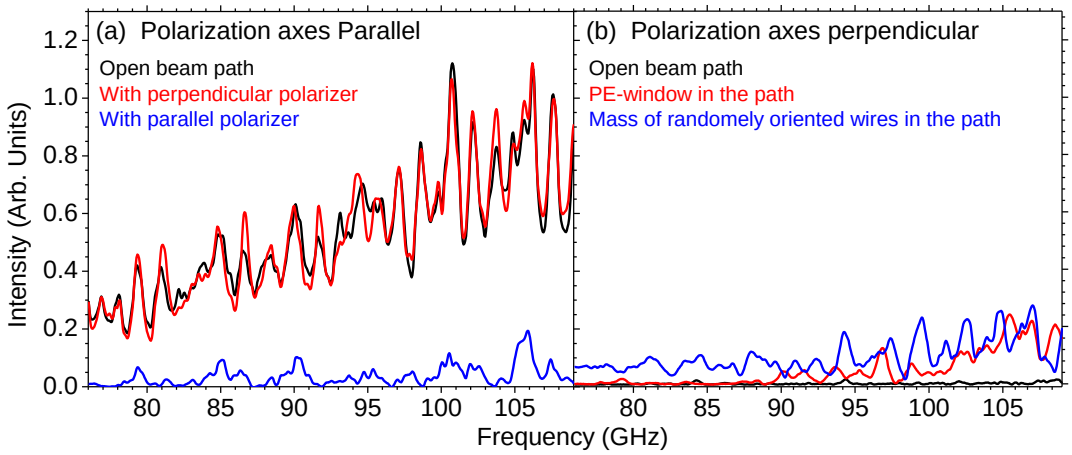

Figure 34: Radiation intensity collected by the collecting horn, radiation power is not leveled. (a) when polarization axes of two horns are parallel (b) when polarization axes are perpendicular.

Linear fits to the data in each full frequency range represent the average photoresponse and its frequency dependence for each V_g. Figure 35 compares such fits to the theoretical *dA/df* spectra from Fig 28 (b). To focus purely on the frequency dependence, each fit is vertically scaled by different values to match the corresponding theoretical *dA/df* curves. These values are presented in table 4.

Table 4: Scaling factors for different gate voltages at 40-60 GHz and 83-108 GHz frequency ranges

V_g (V)	**Scaling Factors**	
	40-60 GHz	**83-108 GHz**
0	2.61×10^{-7}	2.01×10^{-7}
-0.1	3.28×10^{-7}	1.97×10^{-7}
-0.2	4.13×10^{-7}	2.00×10^{-7}

In the low frequency range (Fig. 35), experiment is matched to theory at 47 GHz, while in the high frequency range this occurs at 96.4 GHz. The scaling factors increase monotonically

with increasing V_g magnitude by less than 50% for the low frequency range. In the high frequency range, these factors differ by less than 2%, which is within the experimental uncertainty. In neither case is the vertical ordering of the fits changed by the scaling. The need for different scaling factors in the low frequency range implies that the coupling coefficient *B* depends on gate bias. The coupling between sub-THz and plasmons should be completely accounted for by the theory represented by Fig. 28, but the coupling between plasmons and electrical effect, *B*, lacks a theory, and it might depend on n_s, in principle.

Linear fits shift downward with increasingly negative gate bias for all of the high frequency range and for all but the V_g = 0 case for the low frequency range, in qualitative agreement with the theory curves. Interestingly, the ordering of the linear fits at 40 GHz is opposite that at 60 GHz, just as occurs with the *dA/df* curves. Linear fits obviously cannot reflect the curvature in the *dA/df* spectra in this low frequency range. In the high frequency region, the *dA/df* spectra are more nearly linear. That the fit slopes differ from theory can be attributed to several factors, namely, standing waves, monotonic decrease in power with increasing wavelength due to waveguide attenuation, and monotonic decrease in power with decreasing wavelength due to scattering. It is also interesting that the magnitude of the high frequency response is approximately half that of the low frequency range, though this apparent agreement with Fig. 28 (b) is partly coincidental since the high frequency BWO outputs only 65% as much power as the low frequency one. The agreement between experiment and theory in both frequency and gate-bias dependence, though not exact, is sufficient to support the interpretation that the photoresponse is due to absorption by plasmons within their resonance band.

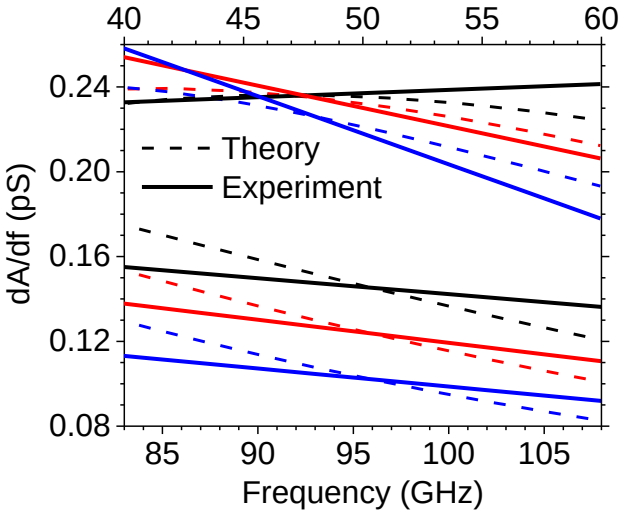

Figure 35: Comparison of theoretical *dA/df* curves with linear fits to measured photoresponse for nominal perpendicular polarization. The upper (lower) group of curves corresponds to the upper (lower) frequency axis.

To reflect the curvature in the *dA/df* spectra in the low frequency range, measured data was also fitted to other functions such as different order polynomials, Gaussian, and Lorentzian function. Although the 2nd-order polynomial was found to explain the curvature in the data, none of the above functions gave a perfect match to the theoretical *dA/df*. The detail explanation of these fittings is presented in appendix D.

The peak response in Fig. 32 is 5 μV for 83-108 GHz frequency range, but there were a few points in the low frequency range which had up to 10 μV peak response. These correspond to a mm-wave induced change in the current through the device of 0.1 μA. The channel resistance at 4 K was measured to be 700 Ω. Using the voltage divider formula, we find that the change in the channel resistance due to absorption of mm-waves by plasmons is 0.13 Ω or

0.02%. This value exceeds by an order of magnitude the value we determine (0.01 Ω) from the data presented for AlGaAs/GaAs HEMTs at 763 GHz in [36].

We may estimate responsivity (for our specific circuit configuration) as follows. Assuming the 2.6 mW mm-wave power at the input to the horn is uniformly distributed over its 300 mm^2 aperture, the intensity leaving the horn is 9 $\mu W/mm^2$. After diverging on its several cm path to the device, with attenuation and scattering by the cryostat window, the intensity may be reduced by at least 10x at the sample. The total power incident on the gate (with dimensions 195 μm × 250 μm) is then about 42 nW. This gives a responsivity estimate of 240 V/W. We may also estimate the NEP of the device as a detector. With maximum signal-to-noise ratio (SNR) of about 220, 42 nW mm-wave power (P) incident on the gate, and lock-in time constant of 3s giving the bandwidth Δf of 0.66 Hz [Appendix E], we estimate $NEP = P/(SNR \times \Delta f^{1/2})$ = 235 $pW/Hz^{1/2}$.

4.1.2 Results of amplitude modulation experiment

For calculations of the plasmon frequencies and absorption spectrum, the value of n_s is estimated from Eq. 5. 4 K I-V curves of the device was measured to determine the V_{th} value to be -0.85 V, giving $n_s = 1.52 \times 10^{12}$ cm^{-2} for $V_g = 0$ V. Although, the same device were used for both AM and FM experiments, but its I-V curves were measured at the beginning of each of the experiments to account for aging and degradation effects. This gave the effective sheet charge density for each of the experiments.

The plasmon absorption spectra are calculated as $A = 1-T$ from Fig 11 and are presented in figure 36 for an unbiased device, $V_{SD} = 0$ V, as a function of V_g. Spectra are shown for the frequencies of up to 700 GHz. At these low frequencies, fundamentals and harmonics are separated by less than their line widths, and hence are not resolved. Their locations, indicated by symbols and identified in the figure, were determined by calculating spectra with an artificially large relaxation time (Fig. 10). These locations are independent of relaxation time up to the limit at which they can no longer be separately resolved, which occurs at $\tau = 0.5$ ps (Fig. 10). The two vertical dashed lines in Fig. 36 mark the experimental excitation frequencies 77 and 106 GHz, which lie within the absorption bandwidth of the fundamental.

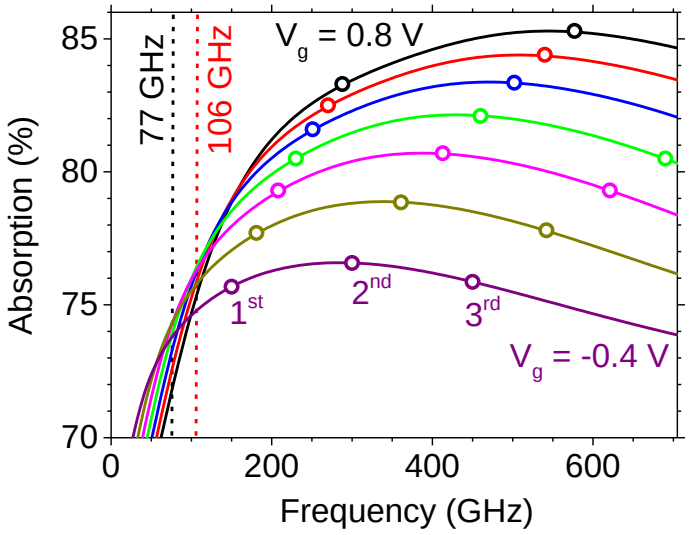

Figure 36:Calculated absorption spectra of the device at different V_g. The extremes of the V_g range are indicated with neighboring curves differing by V_g steps of 0.2 V. Two measurement frequencies are marked by vertical dashed lines.

The measured photoresponse of the unbiased device is presented in figure 37 as a function of V_g for the two excitation frequencies of 77 and 106 GHz. Data for polarization with E-field parallel to the grating bars is also presented, and this parallel response has been reduced from 85% to about 20%, in comparison with [48], by improvements to the set up that increase the polarization purity at the sample.[48, 50-51].

For comparison, the calculated absorption of an unbiased device at 77 and 106 GHz are also plotted as a function of V_g in Fig 37 with the right axis indicating the absorption values (APPENDIX F). These show slices of Fig. 36 in the location of the two dashed lines. The colors of the absorption curves match the color of their respective dashed-lines in Fig 36 and photoresponse curves in Fig. 37. The τ value used in the calculations was determined to be 0.25 ps by calculating the best fit between peaks of the measured photoresponse and that of the absorption curves. The different τ value from FM measurement can be attributed to the gradual degrading of the sample material. These curves peak at V_g values of -0.1 and 0.18 V for 77 and 106 GHz radiations, respectively. The measured photoresponse agrees with the calculated absorption in a number of significant ways. Namely, the overall photoresponse to 106 GHz radiation is stronger and broader than the response at 77 GHz, and its maximum occurs at a more positive V_g value. The peak separation for the two frequencies is about the same for theory and experiment ($\Delta V_g \sim 300 \pm 30$ mV) and absolute V_g values for the measured photoresponse peaks also agree with that those of the calculated absorption spectra. Also note that the absorption values vary by only 5% while the photoresponse varies by 88%. This suggests a non-linear dependence of electrical response on absorption. Another observation is that the measured

photoresponse peaks are sharper than the theoretical ones, which can also result from a non-linearity.

The measured data of unbiased device was also compared with the calculated absorption curves of an imaginary device with 20x smaller sheet charge densities and τ = 6.5 ps. Calculated curves explained the single peak and its line-shape in measured data at 77 GHz as well as the double peak behavior of the 106 GHz data and their line-shape to be due to the crossing of 2nd order harmonic and overtaking of the 3rd-order mode as V_g decreases to higher negative values. It didn't, however, explain the flat photoresponse to 77 GHz for V_g > 0.2 V, it rather showed a nearly monotonic increase in absorption for this V_g range. This analysis also failed to predict the V_g separation between the two peaks in measured data at 106 GHz. While experiment shows a separation of ~ 0.35 V, theory predicts the V_g separation to be ~ 0.6 V. This separation between the 3rd and 2nd order harmonics depends on the factor $ed/\varepsilon_t\varepsilon_0$ which includes the fixed parameters of the device's layer structure. All these parameters are independent of the τ and n_s values used in the calculations, which leaves the V_g separation independent of these values. The detailed analysis is presented in appendix G.

Figure 38 presents the measured photoresponse at 77 GHz for different V_{SD} values which were measured sequentially in the same day. The maximum photoresponse decreases almost two-fold when positive V_{SD} is applied. While the unbiased case shows a single peak, indicated by a symbol, two peaks appear with applied V_{SD}. The second peak seems to move toward lower gate biases with increasing V_{SD}. The first peak apparently has the opposite V_{SD} dependence.

For finite V_{SD}, the qualitative shape of the absorption curve becomes similar to that of the V_{SD} = 0 curve for f = 106 GHz in Fig. 37. To lowest order, the effect of the splitting of the dispersion is simply to red (blue) shift the low frequency shoulder of the absorption spectrum by a frequency value that depends on the drift velocity, Δf. The blue-shift, however, won't be significant due to the broad harmonics in the higher frequencies (with line-widths of ~ 100 GHz) and therefore, only the red-shift will be considered. This is qualitatively similar to artificially increasing the frequency of the source from 77 to 77 + Δf GHz. The photoresponse of the device with applied V_{SD} can then be compared with the absorption of an unbiased device at this higher frequency. The first photoresponse peaks are observed at V_g values of -0.04 and 0.05 V for applied V_{SD} of 0.25 and 0.5 V, respectively. The locations of these maxima can be fitted to the gate-bias dependent absorption curves, with excitation frequency as fitting parameter. This results in two artificially high excitation frequencies of 84 and 93 GHz for V_{SD} of 0.25 and 0.5 V, respectively. These two frequencies are 7.7% and 19.2% larger than 77 GHz. Drift velocity values can then be obtained by fitting Eqs. 3 and 4 to above mentioned percentages. They are concluded to be 1.44 and 3.55×10^5 m/s for V_{SD} values of 0.25 and 0.5 V, respectively. These values are well in the range of previously reported saturation velocities for this material system [68-69].

That a DC current through the drain and load resistor is observed when the source is grounded implies a significant photovoltaic (PV) response [36]. The finite applied positive V_{SD} results in an electron current from Drain to the Source, which induces a photoconductive (PC) behavior in the channel [37]. The possible plasmon induced PC-like photo-current in the biased

device will then flow in the opposite direction of that of the PV-like, decreasing the overall photoresponse. This can result in the measured 2-fold drop in the overall effect. Source-Drain current, I_{SD}, saturates at V_{SD} < 0.5 V for V_g < -0.1 V, however, for more positive gate-biases the transistor operates in the Ohmic region for 0.25 V < V_{SD} < 0.5 V. Therefore, the induced PC-like effect can be more eminent at higher V_g values resulting in the observed bigger drop in photoresponse when device is biased at V_{SD} = 0.5 V for the large positive V_g.

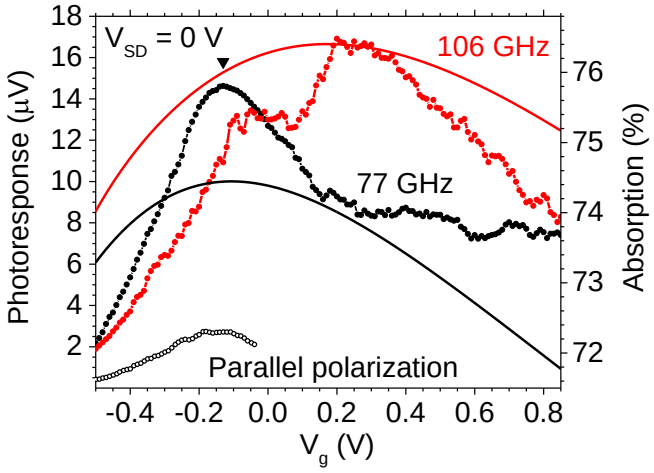

Figure 37: Calculated absorption of the device along with the measured photoresponse as a function of the applied V_g at free-space frequencies of 77 and 106 GHz. Photoresponse is measured with polarization perpendicular to the grating bars, except for one of the curves as indicated.

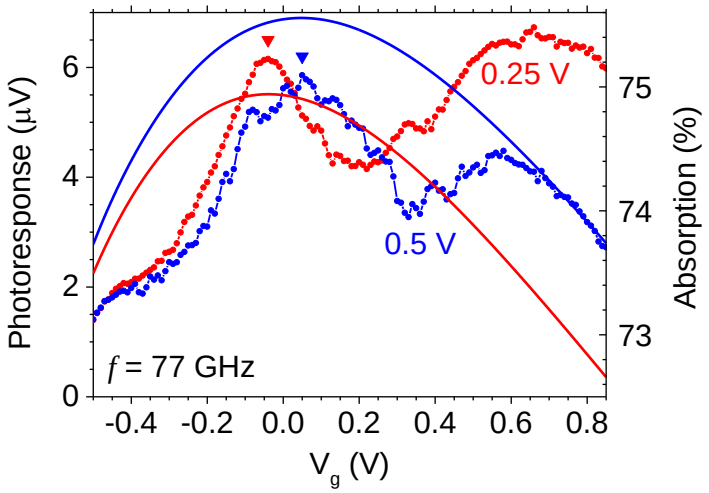

Figure 38: Measured photoresponse of the InGaAs/InP HEMT to free-space frequencies of 77 GHz at different applied V_{SD} values.

NEP of the detector is extracted as a function of V_g from the measured photoresponse and is plotted in figure 39 for the two measurement frequencies. In these calculations, $NEP = P/(SNR \times \Delta f^{1/2})$, where P is the radiation power at the device area, $SNR = Photoresponse\ (V_g) / Noise$ and is the signal to noise ratio, and Δf is the measurement bandwidth taken as 0.05 Hz from 10s lock-in time constant. P is calculated by assuming that the measured 12.2 mW radation power at the input to the horn is uniformly distributed over its 695 mm^2 aperture, giving an intensity of 17.5 $\mu W/mm^2$. We assume that diffraction and scattering may reduce the actual intensity ten-fold at the sample. The total power incident on the 195 μm × 250 μm channel is then about 85 nW. The noise was determined to be ~ 5 nV by blocking the radiation and recording the lock-in output.

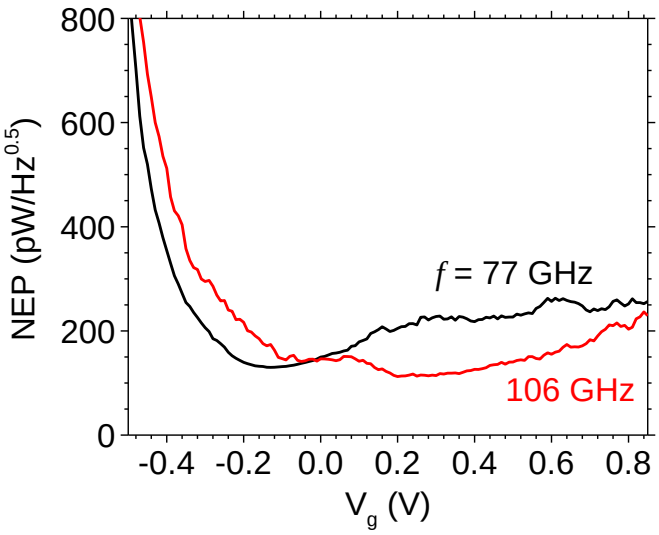

Figure 39:Calculated NEP of the device for the two measurement frequencies. The minimum measured NEP is 113 pW/Hz$^{1/2}$ at 106 GHz.

From Fig. 39, the minimum NEP value is determined to be 113 pW/Hz$^{1/2}$ and is measured at the peak of the response to the 106 GHz radiation. This is comparable to the previously reported values [48, 52]. The smaller value reported in [53] for InGaAs/InP based detectors at room temperature at 1 THz radiation can be partly attributed to the higher measurement frequency (higher $\omega\tau$) and more efficient collection with a narrow band antenna. The peak responsivity of our detector is calculated from the estimated incident power at the device and its peak photoresponse to be 200 V/W, which is approximately equal to previously reported values [48].

4.2 THz HEMT Device

4.2.1 FTIR Measurement of plasmonic spectra (Bomam DA8 Setup)

Following the approach discussed in section 4.1.1, device's I-V characteristics were measured at room and 4 K temperatures for different applied V_g. Saturation I_{SD} values for each V_g were then used to determine relaxation time and sheet charge densities of the device (Table 5).

Table 5: Values of mobility, relaxation time, initial doping, and sheet charge density of THz device for V_g = 0 V at 295 and 4 K.

T (K)	**μ (cm^2/V.s)**	**τ (ps)**	**n_d (cm^{-2})**	**V_{th} (V)**	**n_s (V_g = 0) (cm^{-2})**
295	9700	0.24	1.50×10^{12}	-0.82	1.46×10^{12}
4	21840	0.53	1.37×10^{12}	-0.74	1.33×10^{12}

Presented in figures 40 and 41 are calculated transmission spectra for V_g values of 0, -0.1, and -0.2 V at room and 4 K sample temperatures, respectively. At room temperature, the plasmon fundamental appears at 2.89 THz at zero bias and red-shifts to 2.51 THz under -0.2 V bias. At zero bias, the 2nd-order harmonic appears at 4.77 THz. For low temperatures, the fundamental appears at 2.76 THz for zero gate bias and red-shifts to 2.35 THz for -0.2 V bias. The zero bias 2nd-order harmonic appears near 4.55 THz. Calculated low temperature resonances are sharper and deeper than their room temperature counterparts which is attributed to larger relaxation time when sample is cooled (Section 2.1, Fig. 10).

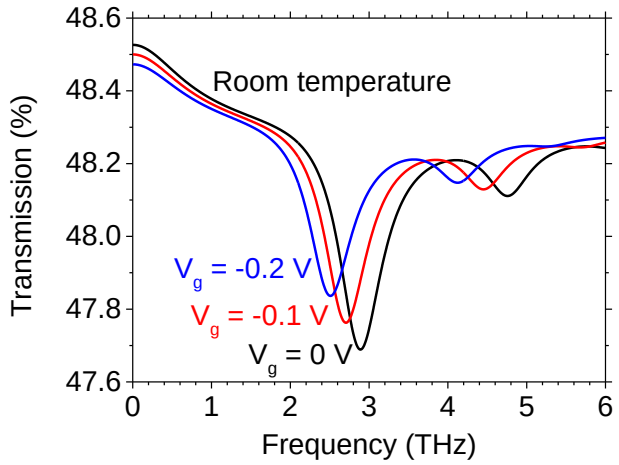

Figure 40: Calculated Plasmon spectra of THz HEMT device at room temperature

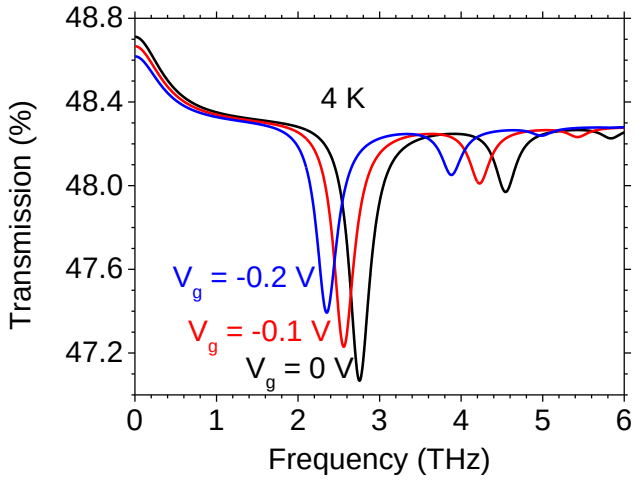

Figure 41: Calculated Plasmon spectra of THz HEMT at 4K sample temperature

Low temperature transmission spectra were measured using two different beam splitters, 12 and 25 micron Mylar, to cover a wider range of frequencies. Figure 42 shows the transmitted power spectra of the sample at helium temperature using the two beam splitters. The primary useful range for the 25 micron beam splitter is determined from these spectra to be 1-3 THz with

a second range of good modulation efficiency observed at 4.5-7.5 THz. The useful range for the 12 micron beamsplitter is evidently 1-7 THz. This beamsplitter is thus the best choice if the plasmon resonance fundamental occurs at 2.76 THz as predicted by theory (Fig. 41). We note that these power spectra were collected with the sample already at helium temperature and positioned in front of the bolometer within its cryostat. Hence any plasmon features should already be present.

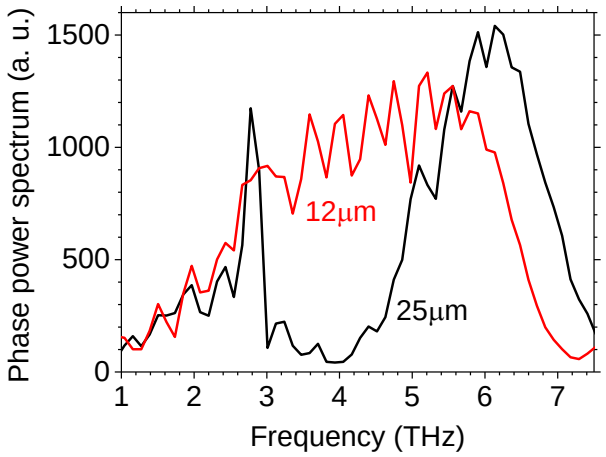

Figure 42: Phase power spectrum for THz HEMT using two different beam splitters. Thicknesses of beam splitters are labeled beside each plot in the graph.

The spectra plotted in Fig. 42 are at low resolution and were obtained from a short double sided interferogram and a complex FFT. This measurement is used to characterize the phase of the interferogram as a function of frequency. Whenever there is a low signal as in case of a strong absorption line, due to low modulation efficiency by the interferometer, the phase is poorly characterized, resulting in spectral artifacts at those frequency positions.

Figure 43 presents a higher resolution transmitted power spectrum using the 12 μm beamsplitter. This spectrum is obtained using a single-ended interferogram and a Cosine FFT with the phase correction obtained from the Fig. 42 measurement. A strong narrow feature with derivative like line shape and ~ 0.06 THz width is observed near 2.76 THz. Such line shape can occur if there is an absorption line in a spectral range where the phase is poorly characterized. A strong line present during the phase characterization, even if unresolved, could cause such a phase error. While sharp features in the low resolution phase spectrum are unexpected on physical grounds, one does occur precisely at 2.76 THz, as shown in figure 44. These considerations strongly suggest the presence of a sharp strong absorption line in the sample.

There is also a suggestion of something in the higher resolution transmission spectrum (Fig. 43) at 4.95 THz, and there is a corresponding feature in the low resolution phase (Fig. 44). Comparison with the calculated spectrum, also plotted in Fig. 43, suggests that the 2.76 THz feature be identified with the plasmon fundamental and that the 4.95 THz feature might be identified as the harmonic.

Working against this assignment is the absence of any significant dependence on gate bias of the observed features. The spike centered at 2.76 THz becomes broader and weaker with increasing negative gate bias which can be a sign of a shift to lower frequencies, however, expectations supported by calculations are for an observable red-shift of Δf ~ 0.5 THz with negative gate bias (Fig. 41). It was confirmed that the HEMT is working by measurement of the

I-V Curves, which also allowed an estimate of sample temperature by comparison with earlier T-dependence characterization of device: T=10K.

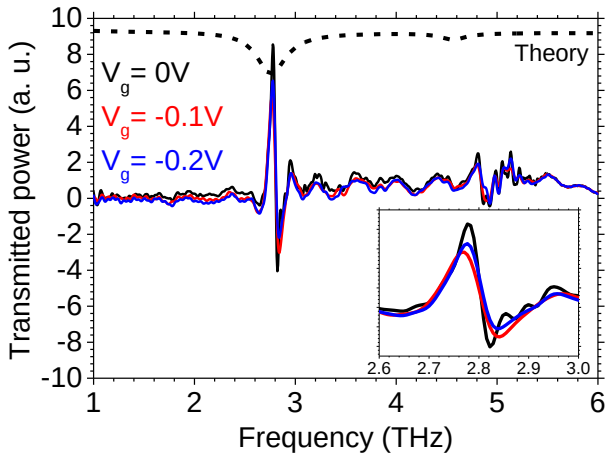

Figure 43: Transmission spectrum of InP HEMT at T = 4 K for three different gate biases.

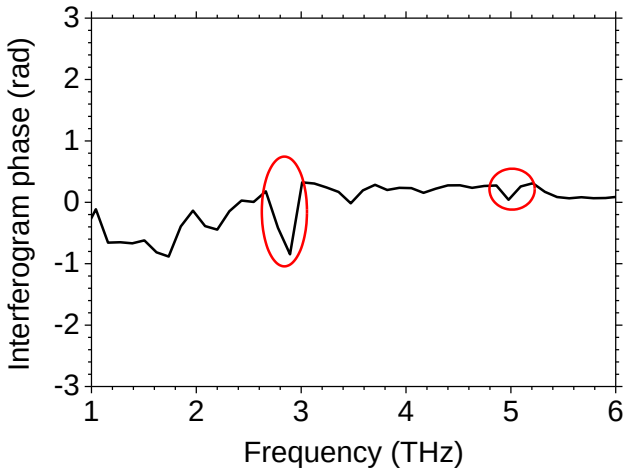

Figure 44: Phase spectrum with sample in the beam. Features in the phase at frequencies associated with features in the transmission spectrum are circled.

4.2.2 FTIR Measurement of plasmonic spectra (Bruker Vertex 80v Setup)

Transmission spectra were measured in the frequency range of 1.8 to 5.3 THz and shown in figure 45. Intensity oscillations, possibly due to Fabry-Perot resonances in the InP substrate of the device, are present in both plots. Plasmon absorptions can be identified by any distortion in the oscillations pattern due to the induced change in the Q-factor of Fabry-Perot cavity.

In Fig. 45, possible plasmon features for each V_g are marked with red arrows and are in qualitative agreement with theory (Fig. 41) in a number of ways, namely, they shift to lower frequencies by increasing negative gate-bias and higher-order resonances are weaker than the lower ones. These features, therefore, may be attributed to 2D-plasmon resonances. Frequencies of observed resonances are, however, different from the theoretical calculations (Fig. 41) and their harmonic numbers cannot be defined with certainty, hence they have been labeled as n^{th} and $(n+1)^{th}$-order. Identified resonance frequencies in $V_g = 0$ V spectrum are not consistent with the ones reported in Fig. 43 despite the fact that the same device was measured with two different FTIR spectrometers.

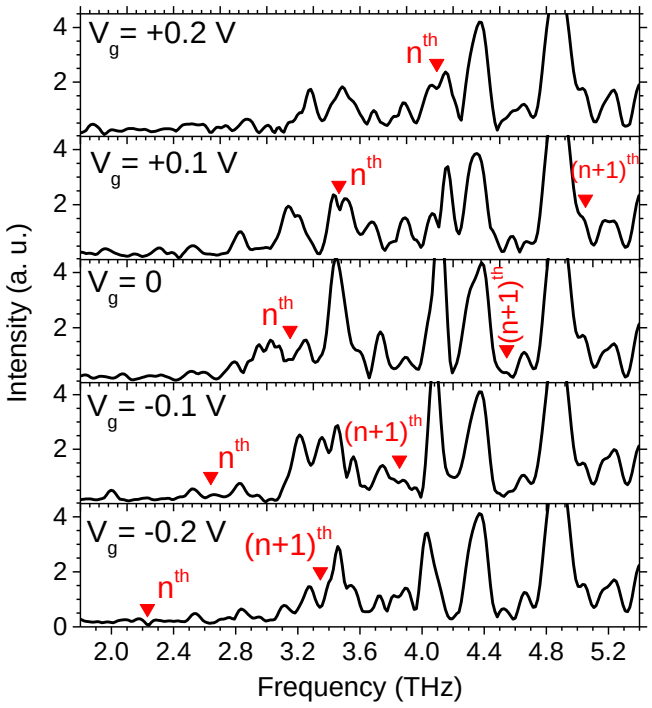

Figure 45: Transmission spectra of the HEMT in frequency range 1.8-5.3 THz.

To better understand the measured data, n^{th} and $(n+1)^{th}$ features were assumed to be 1^{st} and 2^{nd}-order plasmon modes and are marked in figure 46 with black, red, blue, and green symbols for V_g values of 0.1, 0, -0.1, and -0.2 V, respectively. The sheet charge density of the device can then be calculated by fitting the 2D-plasmons dispersion relation of Eq. 1 to the data symbols in Fig 46 with n_s as fitting parameter. Colored curves in Fig. 46 present such fits with colors matching that of their respective data points. Obtained Sheet charge density values are compared with the ones calculated from measured I-V curves in table 6. Absolute values of sheet charge density calculated from two measurements don't match. Zero gate bias n_s value calculated from transmission spectra is higher than the one calculated from I-V curves; however, the two sets of sheet charge densities don't follow this trend at negative gate voltages. It is also

noted that dispersion fits in Fig. 46 don't match the data symbols, which can hint on possibly wrong mode numbers and explain the discrepancies between the two sets of calculated sheet charge densities.

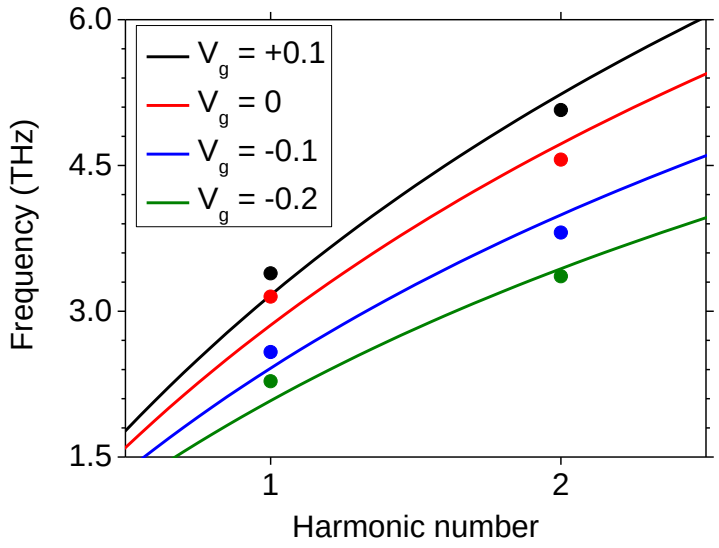

Figure 46: Frequency vs mode number of identified features. Both data points (symbols) and fits (lines) are presented for four measurement gate biases of 0.1, 0, -0.1, and -0.2 V.

Table 6: Comparison of n_s values derived from transmission spectra with those derived from measured I-V curves

V_g (V)	**n_s from I-V curves (cm^{-2})**	**n_s from transmission spectra (cm^{-2})**
0.1	--------	1.76×10^{12}
0	1.33×10^{12}	1.43×10^{12}
-0.1	1.15×10^{12}	1.02×10^{12}
-0.2	9.7×10^{11}	7.6×10^{11}

From Eq. 1, it is seen that ratios ω_{n+1}/ω_n are only affected by the value of nd/a and not by the chosen n_s. Thus, working with resonant frequency ratios as opposed to the absolute frequencies, any experimental uncertainty involving the sheet charge density can be neglected. Figure 47 presents such ratios as a function of d/a for ω_2/ω_1 and ω_3/ω_2 with black and red curves, respectively. Black symbol in Fig. 47 is calculated for the measured device from transmission spectra (Fig. 45) with ω_{n+1}/ω_n = 1.47, and d/a = 38 nm/500 nm = 0.076. This experimental point doesn't correspond with any of the calculated curves which might point to the presence of a virtual gate in the structure as suggested by [76].

Based on device layer structure (Table 2) a second 2DEG layer is located about 20 nm below the top one (Fig. 13). In such structure, the top 2DEG can potentially act as a virtual gate, with its charge carriers mirroring the polarization of the grating bars under THz radiation. The second 2DEG layer will then host the 2D-plasmon oscillations, changing the effective 2DEG depth to d = 20 nm (separation of the two 2DEGs). This changes the experimental value of d/a from 0.076 to 0.04 resulting in the black symbol in Fig 47 to shift to the left (hollow circle). This shift is, however, not enough to associate this experimental value with ω_3/ω_2 curve.

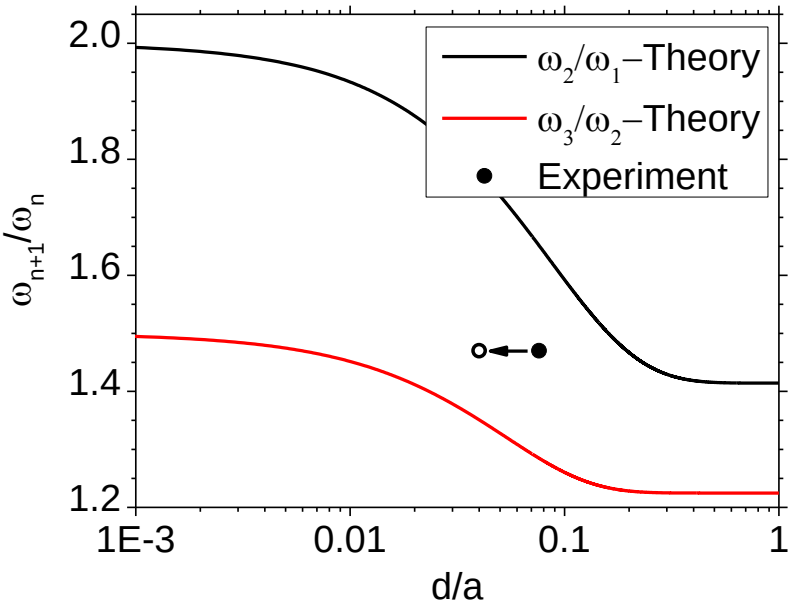

Figure 47: ω_{n+1}/ω_n ratio as a function of *d/a*. The experimental value of the device is shown with the black symbol.

The FTIR experiments for far-IR transmission measurements were repeated for number of times to check the consistency of the measured data. The recorded spectra were highly influenced by low throughput of the device (due to its small dimensions of the gate region when compared with the wavelength of the light), as well as strong atmospheric absorption. These resulted in noisy spectra with low SNR values, making them unrepeatable and inconclusive for the tested THz device.

CHAPTER 5 CONCLUSION AND SUMMARY

In conclusion, we investigated sub-THz and THz resonant detectors based on plasmon excitation in 2DEG of InGaAs/InP-based HEMTs. Investigated devices were fabricated from a double-quantum-well InGaAs/InAlAs heterostructure. A grating coupler was used to compensate for the momentum mismatch between free space radiation and 2D-plasmons. For sub-THz devices grating gate of 9 μm period and 22% duty cycle were fabricated, while for THz device grating period was designed to be 0.5 μm with 80% duty cycle. The photoresponse of the sub-THz device was measured to GHz radiation in two frequency modulation (FM) and amplitude modulation (AM) experiments. Transmission spectra of the THz device were also measured with FTIR spectrometer to investigate the excitation of 2D-plasmons in the channel of the device.

For FM experiments Source and drain of the sub-THz device were grounded with gate biased at 0, -0.1, and -0.2 V with respect to the ground. Photoresponse was recorded as the voltage drop across a load resistor connected to the drain while frequency of the radiation was swept in two ranges of 40-60 and 83-108 GHz that are well within the plasmon resonance bandwidth. Measured photoresponse was strongly affected by formation of standing waves and uncertainties over polarization of the incident light. Further measurements proved that light scattering from the rough surface of the polyethylene window and reflections from different metallic surfaces inside cryostat can alter the polarization state of the incident radiation, and therefore, cause the observed photoresponse at undesired nominal polarization (with E-field

parallel to the grating bars). Moreover, to compare experiment with theory, linear functions were fitted to the data in each full frequency range. These represent the average photoresponse and its frequency dependence for each V_g. linear fits were compared with theory calculation and results were found to be in qualitative agreement. Incident radiation power at the surface of the device was estimated to be ~42 nW and was used to calculate responsivity and NEP of the detector as 240 V/W and 235 pW/Hz$^{0.5}$, respectively.

For AM experiments, gate-bias tunable electrical photoresponse to sub-THz 77 and 106 GHz radiations was measured in our InGaAs/InP sub-THz HEMT. Source and drain of the sub-THz device were grounded with gate voltage was swept from -0.5 V to 0.85 V with V_g step sizes of 0.01 V with respect to the ground. The photoresponse was measured for both unbiased (V_{SD} ~ *0* V) and biased (V_{SD} = 0.25 and 0.5 V) configurations. Radiation generated by the BWO was guided into the cryostat via a rectangular waveguide vacuum-sealed at a standard waveguide junction by a rubber o-ring with a sheet of mylar. This reduced standing wave interferences and polarization scrambling in comparison to FM experiments by having the output of the polarization-preserving horn just few millimeters above the sample, which in turn, reduced the response when the polarization is parallel to the grating bars by 5-folds when compared with FM experiments. The photoresponse spectra of the unbiased device showed a single peak moving to the higher V_g values for higher radiation frequencies, as expected from theory. The spectra for biased device, however, showed two photoresponse peaks. One moving to the higher V_g values and the other one moving in the opposite direction with increasing applied source-drain voltage, V_{SD}. The formation of two oppositely moving peaks were explained in terms of splitting of the

left and right moving plasmons when a $V_{SD} \neq 0$ V is applied. The measured photoresponse also showed some nonlinear behaviors, significantly, the resonance line-widths, as well as the magnitude of the overall plasmon induced photoresponse, are not consistent with values obtained via theoretical absorption spectra calculations which point to a nonlinear relation between the two. Such differences between photoresponse and absorption have been observed previously and in other systems, while the plasmonic absorption in group III-V heterostructures are typically ~ 4-5% at resonance, a resonant photoresponse of 9-times stronger than the baseline is reported for GaAs-devices. Detector parameters such as responsivity and minimum NEP were also estimated for the AM experiment to be 200 V/W and 113 $pW/Hz^{0.5}$, respectively.

In both AM and FM experiments, a photoresponse to sub-THz radiation was observed for V_{SD} = =0V, which is a signature of the photovoltaic nature of the observed electrical effect. In both cases, we attribute the measured photoresponse to excitation of plasmons in the 2DEG and a corresponding change in channel conductance, due to the significant agreements between the 2D-plasmons theory and the measured data. Such a device may find application as a chip-scale tunable sub-THz detector. In principle, by employing a smaller grating period, the device may be scaled to THz frequencies, where resonances are sharper and tuning exceeds the resonant line width.

The plasmonic transmission spectra of the THz device were measured with multiple FTIR spectrometers to investigate excitation of plasmon resonances. In all cases the transmitted signal was masked by high noise levels due to strong atmospheric absorption of THz light and

low throughput of the device. The low throughput was attributed to the small gate region dimensions when compared with the wavelength of the incident beam. Incident light is highly scattered when its wavelength is in the same range of aperture dimensions, which translates into extremely poor light throughput and small signal-to-noise (SNR) ratio that can suppress absorption features due to 2D-plasmon excitation. The transmission measurements of the THz device were therefore found to be unrepeatable and inconclusive.

APPENDIX A:
DERIVATION OF THE DISPERSION RELATION OF PLASMONS FOR A DEVICE WITH APPLIED V_{SD}

Plasmons can be generated in the 2DEG of a grating gated HEMT (Fig. 1) by an incident TM^x polarized light with the magnetic vector potential $\vec{A} = \psi\hat{x}$. The wave function ψ for such potential can be defined as

$$\psi = \begin{cases} \phi_1 e^{i(kx-\omega t)+\delta z} & z \leq 0 \\ \phi_2 e^{i(kx-\omega t)} + \sin\delta(z-d) & 0 < z \leq d \\ 0 & z > d \end{cases} \quad (10)$$

Where 2DEG and Gate are assumed to be at $z = 0$ and d, respectively. δ, ω, and k are assumed to be attenuation constant in z-direction, frequency of the incident light, and plasmon complex wavevector, respectively. The wave equation for the wavefunction of Eq. 10 can be written as

$$\begin{cases} \delta^2 + \gamma^2 + \frac{\varepsilon_r \omega^2}{c^2} = 0 & z \geq 0 \\ -\delta^2 + \gamma^2 + \frac{\varepsilon_r \omega^2}{c^2} = 0 & z < 0 \end{cases} \quad (11)$$

Magnetic and electric field components can be defined as follows for the incident TM^x mode

$$\begin{cases} \vec{H} = (0, H_y, 0) \\ \vec{E} = (E_x, 0, E_z) \end{cases} \quad (12)$$

For the magnetic field, therefore, we will have

$$\vec{H} = \vec{\nabla} \times \vec{A} \rightarrow \vec{H} = \frac{\partial \psi}{\partial z}\hat{y} \quad (13)$$

Which will give the y-component of the magnetic field as

$$H_y = \begin{cases} \delta\phi_1 e^{i(kx-\omega t)+\delta z} & z \le 0 \\ \delta\phi_2 e^{i(kx-\omega t)} + \cos\delta(z-d) & 0 < z \le d \\ 0 & z > d \end{cases} \quad (14)$$

The electric field components can be derived from the Ampere's law which can be written as [77]

$$\frac{\partial \bar{E}}{\partial t} = \frac{1}{\varepsilon}\bar{\nabla} \times \bar{H} \rightarrow \frac{\partial \bar{E}}{\partial t} = \frac{1}{\varepsilon}\left(-\frac{\partial H_y}{\partial z}, 0, \frac{\partial H_y}{\partial x}\right) \quad (15)$$

Solving for the *x*- and *y*-components of the electric field we will have

$$E_z = \frac{-k\delta}{\varepsilon\omega}\begin{cases} \phi_1 e^{i(kx-\omega t)+\delta z} & z \le 0 \\ \phi_2 e^{i(kx-\omega t)} + \cos\delta(z-d) & 0 < z \le d \\ 0 & z > d \end{cases} \quad (16)$$

and

$$E_x = \frac{\delta^2}{i\varepsilon\omega}\begin{cases} \phi_1 e^{i(kx-\omega t)+\delta z} & z \le 0 \\ -\phi_2 e^{i(kx-\omega t)} + \sin\delta(z-d) & 0 < z \le d \\ 0 & z > d \end{cases} \quad (17)$$

Field components above the gate region will be Zero due to the presence of the gate metal. Boundary conditions can be defined as $E_x|_{z=0^+} = E_x|_{z=0^-}$ and $J_x = H_y|_{z=0^+} - H_y|_{z=0^-}$ for the tangential component of the electric and magnetic fields, respectively [77]. Applying these boundary conditions to Eqs. 14, 16 and 17 we will get

$$\phi_1 = \phi_2 \sin\delta d \quad (18.1)$$

$$J_x = \delta(\phi_2 \cos \delta d - \phi_1) e^{i(kx-\omega t)} \qquad (18.2)$$

On the other hand from Ohm's law we have $J_x = \sigma E_x|_{z=0}$, with σ being the surface conductivity of the 2DEG. This gives the *x*-component of the surface current density as

$$J_x = \frac{\delta^2}{i\varepsilon\omega} \sigma \phi_1 e^{i(kx-\omega t)} \qquad (19)$$

Substituting Eq. 17.1 into Eq. 19 will give

$$J_x = \frac{\delta^2}{i\varepsilon\omega} \sigma \phi_2 \sin \delta d \, e^{i(kx-\omega t)} \qquad (20)$$

Comparing Eq. 20 with Eq. 18.2 we will have

$$\frac{\delta\sigma}{i\varepsilon\omega} = (\cot \delta d - 1) \qquad (21)$$

Conductivity of the 2DEG layer is required to derive the dispersion relation of two-dimensional plasmons. To find conductivity, 2DEG is considered as a sea of electrons and magntohydrodynamic relations are solved for the system. From Drude model, for equation of motion of electrons in a conductor layer we have

$$\frac{d\vec{v}}{dt} + \frac{\vec{v}}{\tau} = -\frac{q}{m} \vec{E} \qquad (22)$$

For a sea of electrons velocity will be a function of both position and time and it can be defined as

$$d\vec{v} = \frac{\partial \vec{v}}{\partial x}dx + \frac{\partial \vec{v}}{\partial y}dy + \frac{\partial \vec{v}}{\partial z}dz + \frac{\partial \vec{v}}{\partial t}dt \quad (23)$$

Dividing both sides of Eq. 23 by *dt*, velocity derivative with respect to time can be written as

$$\frac{d\vec{v}}{dt} = v_x \frac{\partial \vec{v}}{\partial x} + v_y \frac{\partial \vec{v}}{\partial y} + v_z \frac{\partial \vec{v}}{\partial z} + \frac{\partial \vec{v}}{\partial t} \quad (24)$$

Rewriting Eq. 24 in terms of the Gradient operator

$$\frac{d\vec{v}}{dt} = \vec{v}.(\nabla \vec{v}) + \frac{\partial \vec{v}}{\partial t} \quad (25)$$

Substituting Eq. 25 into Eq. 22 will give us the Euler equation for electrons in the 2DEG layer as

$$\vec{v}.(\nabla \vec{v}) + \frac{\partial \vec{v}}{\partial t} = -\frac{\vec{v}}{\tau} - \frac{q}{m}\vec{E} \quad (26)$$

Continuity relation for electrons can also be defined as

$$\vec{\nabla}.(n\vec{v}) + \frac{\partial \mathrm{n}}{\partial t} = 0 \quad (27)$$

In small Signal analysis the external radiation can be defined as an electric field with the following relation

$$E_{tot}^{x} = E_0 + E_x^{ss} e^{i(kx-\omega t)} \quad (28)$$

Since the electron density and velocity in the 2DEG depend directly on the applied E-field we can write

$$v_x = v_0 + v_x^{ss} e^{i(kx-\omega t)} \quad (29)$$

$$n = n_0 + n^{ss} e^{i(kx-\omega t)} \quad (30)$$

Inserting Eqs. 29 and 30 into the continuity relation (Eq. 27) we will get

$$-i\omega n^{ss} e^{i(kx-\omega t)} + ikn^{ss} e^{i(kx-\omega t)} + ikn_0 v_x^{ss} e^{i(kx-\omega t)} + 2ikn^{ss} v_x^{ss} e^{2i(kx-\omega t)} = 0 \quad (31)$$

From the small signal analysis, the last term of Eq. 31 can be ignored and v_x^{ss} can be found as

$$v_x^{ss} = \frac{\omega - kv_0}{kn_0} n^{ss} \quad (32)$$

Same as Eq. 31, if we substitute Eq. 29 and 30 into Euler relation, Eq. 26, and consider small signal analysis we will get

$$-i\omega v_x^{ss} e^{i(kx-\omega t)} + ikv_0 v_x^{ss} e^{i(kx-\omega t)} = \frac{-q}{m^*} E_0 + \frac{-q}{m^*} E_x^{ss} e^{i(kx-\omega t)} - \frac{v_0}{\tau} - \frac{v_x^{ss}}{\tau} e^{i(kx-\omega t)} \quad (33)$$

Separating the terms with and without exponential factor, it is concluded that

$$\begin{cases} \left(ikv_0 - i\omega + \frac{1}{\tau}\right) v_x^{ss} = \frac{-q}{m^*} E_x^{ss} \\ \\ v_0 = \frac{-q\tau}{m^*} E_0 \end{cases} \quad (34)$$

Substituting Eq. 32 into Eq. 34 will give

$$\left(ikv_0 - i\omega + \frac{1}{\tau}\right) \frac{\omega - kv_0}{kn_0} n^{ss} = \frac{-q}{m^*} E_x^{ss} \quad (35)$$

On the other hand from Ohm's law current density can be written as $J = -qnv = \sigma E$. Substituting Eqs.28-30 for E, v, and n in the J relation, we will have

$$-qn_0v_0 - qn_0v_x^{ss}e^{i(kx-\omega t)} - qn_{ss}v_0e^{i(kx-\omega t)} - qn_{ss}v_x^{ss}e^{2i(kx-\omega t)}$$

$$= \sigma E_0 + \sigma E_x^{ss}e^{i(kx-\omega t)} \quad (36)$$

Considering small signal analysis and separating the term with and without exponential factor we will get

$$\begin{cases} -q(n_0v_x^{ss} + n_{ss}v_0) = \sigma E_x^{ss} \\ \\ -qn_0v_0 = \sigma E_0 \end{cases} \quad (37)$$

Replacing for v_x^{ss} in Eq. 37 from Eq. 32 it can be derived that

$$n_{ss} = \frac{k\sigma}{-q\omega}E_x^{ss} \quad (38)$$

Substituting Eq. 38 in Eq. 35 will give

$$\left(ikv_0 - i\omega + \frac{1}{\tau}\right)\frac{\omega - kv_0}{n_0}\frac{k\sigma}{-q\omega}E_x^{ss} = \frac{-q}{m^*}E_x^{ss} \quad (39)$$

Crossing the E_x^{ss} from both sides of the Eq. 39 and solving for σ, surface conductivity can be obtained as

$$\sigma = \frac{Ne^2}{m^*}\frac{\omega}{(\omega - v_0k)\left(ikv_0 - i\omega + \frac{1}{\tau}\right)} \quad (40)$$

Incorporating Eq. 40 for conductivity into Eq. 21, it can be calculated that

$$(\cot \delta d - 1) = \frac{Ne^2\delta}{i\varepsilon m^*} \frac{1}{(\omega - v_0 k)\left(ikv_0 - i\omega + \frac{1}{\tau}\right)} \quad (41)$$

Assuming a highly confined 2DEG ($\delta d << 1$) we will have $cot\delta d - 1 \sim {}^{1}/_{\delta d} - 1 \sim {}^{1}/_{\delta d}$ which simplifies Eq. 41 as

$$-4A\delta^2 di = (\omega - v_0 k)\left(ikv_0 - i\omega + \frac{1}{\tau}\right) \quad (42)$$

Where $A = Ne^2/4\varepsilon m^*$. Substituting for δ^2 from the wave equation,

$$-4A\left(\delta^2 + \frac{\varepsilon_r \omega^2}{c^2}\right) di = (\omega - v_0 k)\left(ikv_0 - i\omega + \frac{1}{\tau}\right) \quad (43)$$

For the device reported here $k = 2\pi/a$ with a = 9 μm, $\omega = 2\pi f$ with f = 100 GHz, ε_r = 13.90. this will give $k^2 \sim 4.9\times10^{11}$ m^{-2} and $\varepsilon_r\omega^2/c^2 \sim 2.64\times10^{8}$ cm^{-2}. Therefore $\varepsilon_r\omega^2/c^2$ factor can be ignored and $\delta^2 \approx k^2$. Re-arranging Eq. 43 for is a quadratic function of k we will have

$$(4Ad - v_0^2)k^2 + \left(2\omega v_0 + \frac{iv_0}{\tau}\right)k - \left(\omega^2 + \frac{i\omega}{\tau}\right) = 0 \quad (44)$$

Solving for k and assuming $\omega\tau >> 1$ we will have

$$k_{1,2} = \frac{-\left(\frac{iv_0}{\tau} + 2v_0\omega\right) \pm \sqrt{\Delta}}{2\left(4Ad - v_0^2\right)} \quad (45)$$

$$\Delta \equiv -\frac{v_0^2}{\tau^2} + 16Ad\omega^2 \quad (46)$$

Which are similar to Eq. 3 and 4 in the Chapter 2.

APPENDIX B: CALCULATION OF THE DISPERSION CURVES

This Program was developed in Wolfram Mathematica to calculate the dispersion curves of the n^{th}-order harmonic for devices with and without applied V_{SD}

```
e=1.6 10^-19; (*electron Charge, C*)
p=N[Pi];
eps0=8.85 10^-12; (*Vacuum Permittivity, F/m*)
epst=12.24; (*Relative Permittivity of InAlAs layer*)
epss=13.90;
mstar=0.043; (*Effective electron mass*)
me=9.11 10^-31; (*Electron mass, Kg*)
d=38 10^-9; (*2DEG depth, m*)
tau=0.25 10^-12; (*Relaxation time S*)
Vsd=0.5; (*Applied source drain voltage, V*)
L=250 10^-6; (*Channel Length, m*)
a=9 10^-6; (*Grating Period, m*)
meu=e tau /(me mstar);(*mobility, V^2/m.S*)
v01=1 10^5;
v02=0;(*Drift Velocity m/s*)
p=N[Pi];(*3.14*)
A[ns_]:=(ns*e^2)/(4 epst eps0 me mstar)
qn[n_]:=2*p*n/a
neu1[v0_,ns_,n_]:=((2*v0*qn[n])+Sqrt[16*A[ns]*d*(qn[n]^2)])/(4 p)
neu2[v0_,ns_,n_]:=((2*v0*qn[n])-Sqrt[16*A[ns]*d*(qn[n]^2)])/(4 p)
t1=Table[{i,neu1[v01,i,1]},{i,0,3 10^16,1 10^14}];
t2=Table[{i,-1*neu2[v01,i,1]},{i,0,3 10^16,1 10^14}];
t3=Table[{i,neu1[v02,i,1]},{i,0,3 10^16,1 10^14}];
t4=Table[{i,-1*neu2[v02,i,1]},{i,0,3 10^16,1 10^14}];
Fig1=ListPlot[t1];
Fig2=ListPlot[t2];
Fig3=ListPlot[t3];
Fig4=ListPlot[t4];
Show[Fig1,Fig2,Fig3,Fig4]
SetDirectory["D:\\Most up to date folders\\Research\\HEMT Project\\HEMT-UCF\\HEMT
Data\\PLS020 Series\\PLS023C (Sub-THz device-UCF)\\Calculated Plasmon Spectrum\\11-15-
2013 (Nov 2013 data)\\Dispersion Relation analysis"]
Export["w(+) vs ns.txt",t1,"CSV"]
Export["w(-) vs ns.txt",t2,"CSV"]
Export["w0 vs ns.txt",t3,"CSV"]
```

This program was developed in Wolfram Mathematica to calculate the frequency of the fundamental plasmon harmonic for a given range of sheet charge densities in a biased and unbiased device.

```
e=1.6 10^-19; (*electron Charge, C*)
ns=1.51 10^16; (*Sheet Charge Density*)
p=N[Pi];
eps0=8.85 10^-12; (*Vacuum Permittivity, F/m*)
epst=12.24; (*Relative Permittivity of InAlAs layer*)
epss=13.90;
mstar=0.043; (*Effective electron mass*)
me=9.11 10^-31; (*Electron mass, Kg*)
d=38 10^-9; (*2DEG depth, m*)
tau=0.25 10^-12; (*Relaxation time S*)
Vsd=0.5; (*Applied source drain voltage, V*)
L=250 10^-6; (*Channel Length, m*)
a=9 10^-6; (*Grating Period, m*)
meu=e tau /(me mstar);(*mobility, V^2/m.S*)
v01=1 10^5;
v02=0;(*Drift Velocity m/s*)
p=N[Pi];(*3.14*)
A=(ns*e^2)/(4 epst eps0 me mstar);
neu1[v0_,k_]:=((2*v0*k)+Sqrt[16*A*d*(k^2)])/(4 p)
neu2[v0_,k_]:=((2*v0*k)-Sqrt[16*A*d*(k^2)])/(4 p)
neu1[3.55 10^5,702403]
-neu2[3.55 10^5,702403]
t1=Table[{i,neu1[v01,i]},{i,0,1.5 10^6,1 10^4}];
t2=Table[{i,-neu2[v01,i]},{i,0,1.5 10^6,1 10^4}];
t3=Table[{i,neu1[v02,i]},{i,0,1.5 10^6,1 10^4}];
t4=Table[{i,-neu2[v02,i]},{i,0,1.5 10^6,1 10^4}];
Fig1=ListPlot[t1];
Fig2=ListPlot[t2];
Fig3=ListPlot[t3];
Fig4=ListPlot[t4];
Show[Fig1,Fig2,Fig3,Fig4]
SetDirectory["D:\\Most up to date folders\\Research\\HEMT Project\\HEMT-UCF\\HEMT
Data\\PLS020 Series\\PLS023C (Sub-THz device-UCF)\\Calculated Plasmon Spectrum\\11-15-
2013 (Nov 2013 data)\\Dispersion Relation analysis"]
Export["w(+) vs ns.txt",t1,"CSV"]
```

```
Export["w(-) vs ns.txt",t2,"CSV"]
Export["w0 vs ns.txt",t3,"CSV"]
```

APPENDIX C: CALCULATION OF THE TRANSMISSION SPECTRUM OF THE DEVICE.

This program is written in Wolfram Mathematica to calculate the transmission spectrum of a plasmon based HEMT device based on the recipe provided in Theory of 2D-grating couplers [ZSM Theory]

```
(*Fundamental constants, Gaussian units*)

e=4.80325 10^-10 (*electron charge, Sqrt[dyne-cm^2]*);
c=2.99792 10^10 (*speed of light, cm/s*);
m=9.10939 10^-28 (*electron mass, g*);
p=N[Pi];
eps0=10^7/(4 p (c/100)^2)  (*permittivity of free space, C^2/N-m^2*);

(*Device parameters*)

ns=0.037 10^12;(*2DEG carrier density, cm^-2*)
d=380 10^-8 (*2DEG depth, cm*);
tOVERa= 0.22(*ratio of grating window widths to grating period*);
a=9 10^-4 (*grating period, cm*);
t=tOVERa a (*width of grating windows, cm*);

(*Materials parameters*)

mef=0.043m (*electron effective mass gram*);
tau=25 10^-12 (*relaxation time, sec*);
es=13.90(*In[.68]Ga[.32]As substrate permittivity*);
eo=12.24(*In[.52]Al[.48]As top layer permittivity*);
rh=1050 4 p eps0/100 (*2D resistivity in grating gaps, first # is ohms, rest converts to s/cm*);
rl=rh 0.1 4 p eps0/100 (*2D resistivity of grating bars, s/cm*);

(*experimental parameters*)

wm=2 p c 0.1 (*minimum frequency, rad/s*);
dw=2 p c 0.1 (*frequency resolution rad/s*);

(*Derived quantities for device*)

ra=(t/a) rh + (1-t/a) rl(*average 2D surface resisitivity s/cm*);
sa=(t/a) (1/rh) + (1-t/a) (1/rl) (*average 2D surface conductivity, cm/s*);
g=2 p/a (*grating wavevector, 1/cm*);
```

```
(*Defined functions*)
vt[n_,time_]:= n e^2 time/mef (*cm/s*);
d1[x_,time_]:=(1-x^2 time^2)^2 + 4 x^2 time^2;
alf[x_,n_,time_]:=vt[n,time] (1+x^2 time^2)/d1[x,time];
bet[x_,n_,time_]:=vt[n,time] x time (1+x^2 time^2)/d1[x,time];
d2[x_,k_,n_,time_]:=(es+eo Coth[k g d] - 4 p k g bet[x,n,time]/x)^2+(4 p k g alf[x,n,time]/x)^2;
ak[x_,k_,n_,time_]:=eo^2 (1-Coth[g k d]^2) alf[x,n,time]/d2[x,k,n,time];
bk[x_,k_,n_,time_]:=((4 p g k/x) (1+eo Coth[g k d]) (alf[x,n,time]^2+bet[x,n,time]^2)-(2(es+eo
(1+es) Coth[g k d])+eo^2(1+Coth[g k d]^2)) bet[x,n,time]+(es+eo Coth[g k d]) (es+eo (1+es)
Coth[g k d]+eo^2) (x/(4 p g k)))/d2[x,k,n,time];
rtl[k_]:=(2/(p k)) (rh-rl) Sin[p k t/a];
uE[x_,n_,time_]:=(1/ra)-(1/2) Sum[(rtl[k]/ra)^2 ak[x,k,n,time],{k,1,10}];
uF[x_,n_,time_]:=-(1/2) Sum[(rtl[k]/ra)^2 bk[x,k,n,time],{k,1,10}];
bigD[x_,n_,time_]:=((1+Sqrt[es]+(4 p/c) (alf[x,n,time]+uE[x,n,time])) (1+Sqrt[es]+(4p/c)
(alf[x,n,time] + sa))-(4 p/c)^2 ((bet[x,n,time]+uF[x,n,time]) bet[x,n,time]))^2+((4 p/c)
(bet[x,n,time]+uF[x,n,time]) (1+Sqrt[es]+(4 p/c) (alf[x,n,time]+sa))+(4 p/c) bet[x,n,time]
(1+Sqrt[es]+(4 p/c) (alf[x,n,time]+uE[x,n,time])))^2;
Eyy2[x_,n_,time_]:=(4(1+Sqrt[es]+(4 p/c) (alf[x,n,time]+sa))^2+(8 p
bet[x,n,time]/c)^2)/bigD[x,n,time];
Ezy2[x_,n_,time_]:=0.;
Ty[x_,n_,time_]:=Sqrt[es] (Eyy2[x,n,time]+Ezy2[x,n,time]);
Ezz2[x_,n_,time_]:=(4(1+Sqrt[es]+(4 p/c) (alf[x,n,time]+uE[x,n,time]))^2+(8 p/c)^2
(bet[x,n,time]+uF[x,n,time])^2)/bigD[x,n,time];
Eyz2[x_,n_,time_]:=0.;
Tz[x_,n_,time_]:=Sqrt[es] (Ezz2[x,n,time]+Eyz2[x,n,time]);
TtotDevice[x_,n_,time_]:=(Ty[x,n,time]+Tz[x,n,time])/2;

(*Reference sample quantities*)

tOVERaref= 1;
tref=tOVERaref a (*width of grating windows, cm*);

(*Derived functions for reference*)

raref=(tref/a) rh + (1-tref/a) rl(*average 2D surface resisitivity s/cm*);
saref=(tref/a) (1/rh) + (1-tref/a) (1/rl) (*average 2D surface conductivity, cm/s*);
rtlref[k_]:=(2/(p k)) (rh-rl) Sin[p k tref/a];
uEref[x_,n_,time_]:=(1/raref)-(1/2) Sum[(rtlref[k]/raref)^2 ak[x,k,n,time],{k,1,10}];
uFref[x_,n_,time_]:=-(1/2) Sum[(rtlref[k]/raref)^2 bk[x,k,n,time],{k,1,10}];
bigDref[x_,n_,time_]:=((1+Sqrt[es]+(4 p/c) (alf[x,n,time]+uEref[x,n,time])) (1+Sqrt[es]+(4p/c)
(alf[x,n,time] + saref))-(4 p/c)^2 ((bet[x,n,time]+uFref[x,n,time]) bet[x,n,time]))^2+((4 p/c)
```

```
(bet[x,n,time]+uFref[x,n,time]) (1+Sqrt[es]+(4 p/c) (alf[x,n,time]+saref))+(4 p/c) bet[x,n,time]
(1+Sqrt[es]+(4 p/c) (alf[x,n,time]+uEref[x,n,time])))^2;
Eyy2ref[x_,n_,time_]:=(4(1+Sqrt[es]+(4 p/c) (alf[x,n,time]+saref))^2+(8 p
bet[x,n,time]/c)^2)/bigDref[x,n,time];
Ezy2ref[x_,n_,time_]:=0.;
Tyref[x_,n_,time_]:=Sqrt[es] (Eyy2ref[x,n,time]+Ezy2ref[x,n,time]);
Ezz2ref[x_,n_,time_]:=(4(1+Sqrt[es]+(4 p/c) (alf[x,n,time]+uEref[x,n,time]))^2+(8 p/c)^2
(bet[x,n,time]+uFref[x,n,time])^2)/bigDref[x,n,time];
Eyz2ref[x_,n_,time_]:=0.;
Tzref[x_,n_,time_]:=Sqrt[es] (Ezz2ref[x,n,time]+Eyz2ref[x,n,time]);
Ttotref[x_,n_,time_]:=(Tyref[x,n,time]+Tzref[x,n,time])/2;

(*This section calculates the transmission spectrum of the device*)

t1=Table[{(wm+i dw)/(2 p c),TtotDevice[(wm + i dw),ns,tau]},{i,0,2000}];
ListPlot[t1, PlotJoined→True, PlotRange→{0,0.4},Frame→True]
(*This section calculates the transmission spectrum of the reference with t/a=1*)
t2=Table[{(wm+i dw)/(2 p c),Ttotref[(wm + i dw),ns,tau]},{i,0,2000}];
ListPlot[t2, PlotJoined→True, PlotRange→{0,1},Frame→True]

(*This section calculates the transmittance spectrum of the HEMT*)

Ttot[x_,n_,time_]:=TtotDevice[x,n,time]/Ttotref[x,n,time];
t3=Table[{(wm+i dw)/(2 p c),Ttot[(wm + i dw),ns,tau]},{i,0,2000}];
ListPlot[t3, PlotJoined→True, PlotRange→{0,1},Frame→True]
Absorp[x_,n_,time_]:=1-(TtotDevice[x,n,time]/Ttotref[x,n,time]);
t4=Table[{(wm+i dw)/(2 p c),Absorp[(wm + i dw),ns,tau]},{i,0,300}];
ListPlot[t4, PlotJoined→True, PlotRange→{0.6,1},Frame→True]

(*This section differentiates the transmittance spectrum of the HEMT*)

DerTtot[x_,n_,time_]:=D[Ttot[x,n,time],x];
t5=Table[{(wm+i dw),DerTtot[x,ns,tau]/.x→(wm+i dw)},{i,0,2000}];
ListPlot[t5, PlotJoined→True, PlotRange→{-32*10^-14,5*10^-14},Frame→True]
t6=Table[{(wm+i dw),-1*DerTtot[x,ns,tau]/.x→(wm+i dw)},{i,0,2000}];
ListPlot[t6, PlotJoined→True, PlotRange→{-5*10^-14,32*10^-14},Frame→True]

SetDirectory["D:\\Most up to date folders\\Research\\HEMT Project\\HEMT-UCF\\HEMT
Data\\PLS020 Series\\PLS023C (Sub-THz device-UCF)\\Calculated Plasmon Spectrum\\11-15-
2013 (Nov 2013 data)\\Relaxation Time Test"]
Export["PLS023C-d38nm-a9um-tau0,18-Vgn0,4DivTransmission.txt",t1,"CSV"]
Export["PLS023C-d38nm-a9um-tau0,18-Vgn0,4RefTransmission.txt",t2,"CSV"]
```

Export["Imag Device-tau0.25-ns1,51e12-mstar0,08-tOVERa 0,8-a0,5um-d38nm.txt",t3,"CSV"]
Export["PLS023C-tau25-ns0.037e12(nsOVER21,5)-Absorption.txt",t4,"CSV"]
Export["PLS023C-tau0,25-Vgn0,4-dToverdf.txt",t5,"CSV"]
Export["PLS023C-ns1,04d20nmtau0,37nTransmittanceDerivativeVsAngFreq.txt",t6,"CSV"]*)

APPENDIX D:
FITTING OF THE FM EXPERIMENTAL DATA USING MULTIPLE FUNCTIONS

Polynomial fit to the measured data in 40-60 GHz frequency range

As seen in Fig. 35 theory lines in 40-60 GHz frequency range have a curvature that is not reflected by linear fits to the measured photoresponse. Series of polynomial functions were fitted to the measured data to reproduce these curvatures. Different 2nd and 3rd-order polynomials were tried until a function in the form of ax^2+bx gave the best fit to the data. Figure 48 compares such a fit to the theoretical curves. Polynomial fits are scaled vertically to match theory lines with different scaling factors for each gate-bias. These scaling factors are plotted in figure 49 as a function of V_g with red symbols while the black line represents a linear fit to these points. Calculated scaling factors are increasing linearly with increasing negative gate voltage. 2nd-order polynomial fits reproduce the curvature of theory lines; however, theory lines and experimental fits don't match.

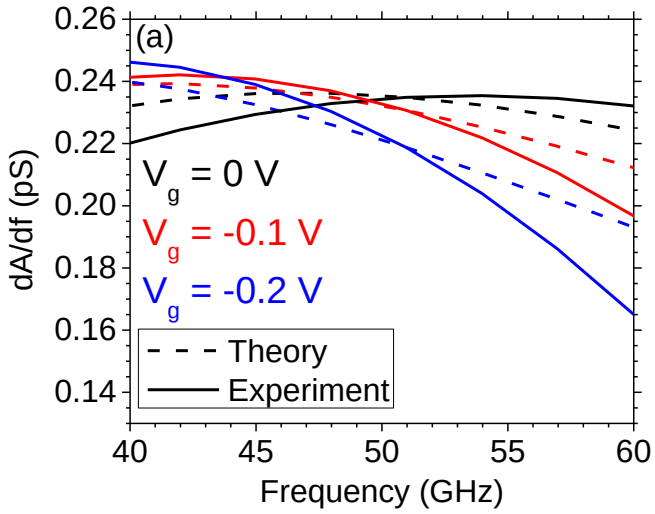

Figure 48: Comparison of theoretical *dA/df* curves with polynomial fits to measured photoresponse for frequency range of 40-60 GHz.

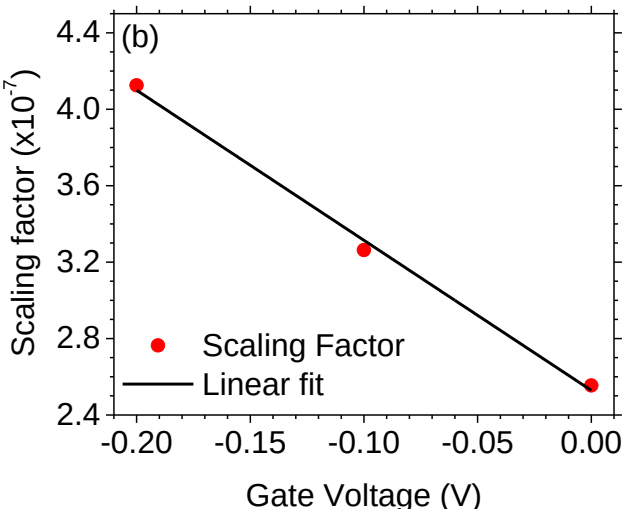

Figure 49: Scaling factor vs Vg data (symbols) and linear fit (line).

Gaussian and Loretzian fits to the data and theory

The absorption spectra of the device, $A = 1-T$, is calculated and shown in figure 28 (a). Absorption peaks in a spectrum can typically be approximated by a Gaussian or Lorentzian function. Therefore, in the first attempt both of these functions were fitted to the absorption spectrum at zero gate-bias and in frequency range of 5-150 GHz. Figure 50 presents the absorption spectrum along with Gaussian and Lorentzian fits with black symbols, red and blue curves respectively. Both functions match theory up to 140 GHz where they start to diverge. A slight slop mismatch, however, can be observed between absorption spectrum and fitted functions in this figure.

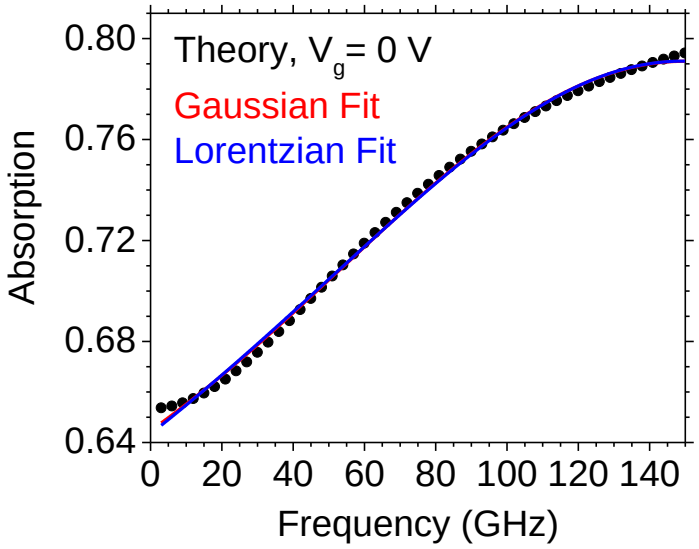

Figure 50: Theoretical absorption spectrum (Black symbols) along with Gaussian and Lorentzian fits (Red and Blue curves) in frequency range of 5-150 GHz.

Since the measured photoresponse is related to *dA/df* by Eq. 9, derivatives of the theory line and fitted Gaussian function were calculated with respect to frequency and compared in figure 51. Although Gaussian fit matches the absorption spectrum, the derivatives don't match. This is possibly due to the observed slope mismatch in Fig 50. The Lorentzian function also shows the same behavior when derivatives were compared.

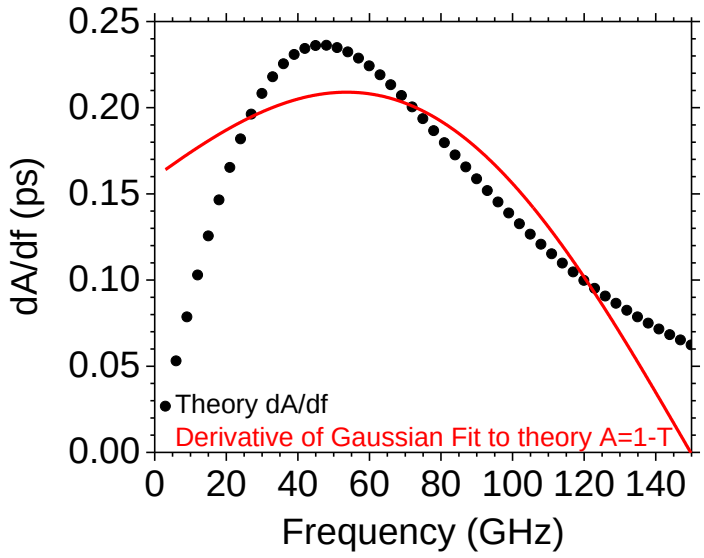

Figure 51: Theoretical *dA/df* spectrum (Black symbols) along with derivative of Gaussian fit (Red curve) in frequency range of 5-150 GHz.

APPENDIX E:
NOISE ANALYSIS AND REQUIRED LOCK-IN AMPLIFIER INTEGRATION TIME TO ELIMINATE A NOISE COMPONENT.

Lock-in amplifier is used to measure low electrical signal levels in a high noise environment. One example to these environments is photodetectors. In characterization of such detectors, the incident light is electrically modulated or mechanically chopped with a reference signal. Then the detector output will be monitored and its Fourier component at the modulation/chopping frequency will be measured by Lock-in amplifier. Stronger the component, larger will be the output of the amplifier. During this process, the detector output will be averaged by the instrument over a preset time span called Lock-in Time Constant, τ.

On the other hand, one of the most important figures of merit to characterize photodetectors is Noise-Equivalent-Power (NEP) for application purposes. This value is defined as the radiation power that can generate signal-to-noise ratio (SNR) of 1 at 1 Hz output bandwidth and it's calculated by $NEP = P/(SNR \times \Delta f^{1/2})$ where P is the incident power on the detector and Δf is the bandwidth that is defined by $2/\tau$. This appendix, presents the derivation of $\Delta f = 2/\tau$.

A sinusoidal electrical signal with the frequency of f_0 can be defined by:

$$S = A_1 Cos(2\pi f_0 t) \qquad (47)$$

Where t is the time and A_1 is the amplitude of the signal. If the system encounters a sinusoidal noise of bandwidth Δf centered around f_0 ($\Delta f << f_0$), it's mathematical relation can be written as:

$$N = A_2 Cos\left[2\pi\left(f_0 \pm \frac{\Delta f}{2}\right)t\right] \qquad (48)$$

During the measurements, the input of the Lock-in amplifier will be the superposition of signal and noise, *S+N*, which is in the form of

$$S + N = A_1 Cos(2\pi f_0 t) + A_2 Cos\left[2\pi\left(f_0 \pm \frac{\Delta f}{2}\right)t\right] = Re\left[\left(A_1 + A_2 e^{-i2\pi\frac{\Delta f}{2}t}\right)e^{-i2\pi f_0 t}\right] \qquad (49)$$

This is a Sin-wave with frequency of f_0 and modulated amplitude. Depending of the strength of the modulation term ($A_2 e^{-i2\pi\frac{\Delta f}{2}t}$) the input can look like wave packets with beat frequency of $\Delta f/2$. Averaging over the defined time constant the noise component of the input will be removed and lock-in will record the desired signal. This required time constant is calculated below.

Figure 52 (top), shows the signal and noise of an electrical system over 100 mS, where the amplitude of signal and noise, A_1 and A_2, are 2 mV and 0.2 mV respectively. Signal frequency is f_0 = 100 Hz and noise bandwidth is $\Delta f = 1\ Hz$. In this figure the signal and noise are plotted with black and red color curves respectively. Fig. 52 (down), presents the super position of two sinusoidal waves which is observed by Lock-in Amplifier over the course of $t = 5\ S$. the amplitude of the signal is modulated from 1.8 to 2.2 mV with modulation frequency of $\frac{\Delta f}{2} = 0.5\ Hz$ which is consistent with Equ. 49 above.

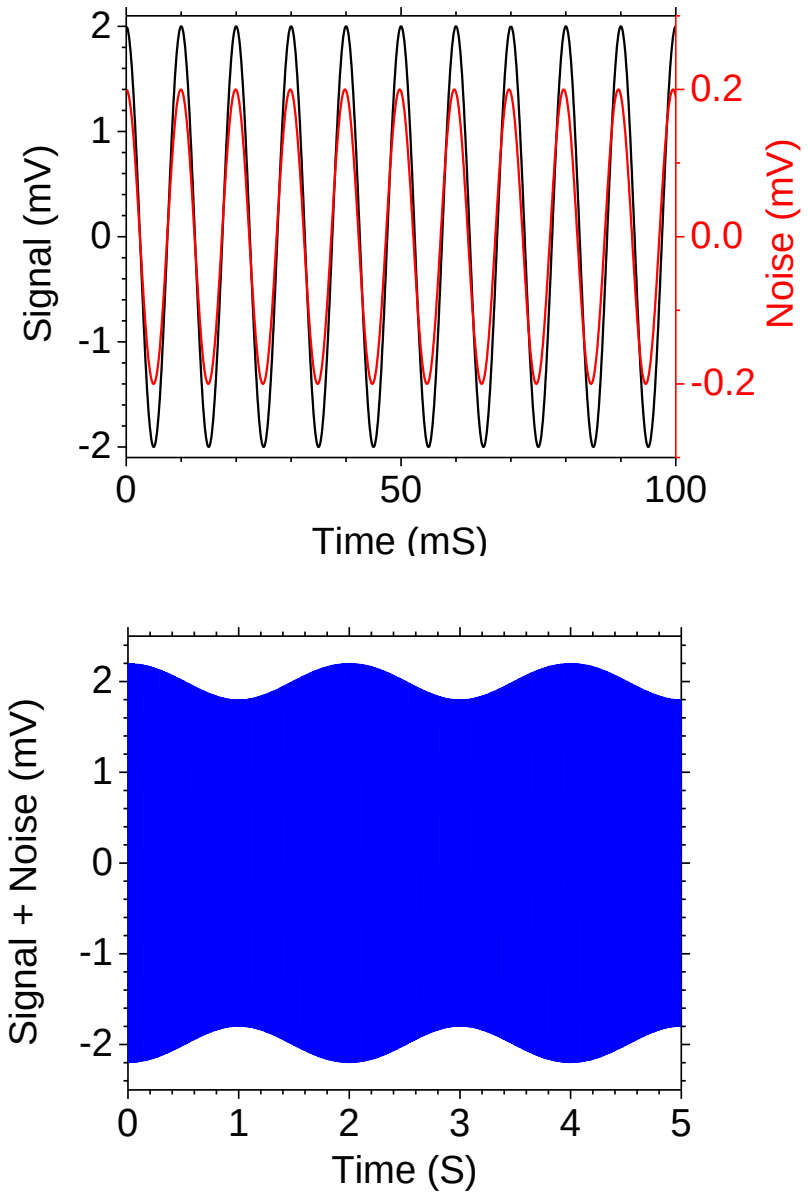

Figure 52: Sinusoidal signal and noise curves are presented with black and red colors respectively for a signal with 2 mV amplitude and 100 Hz frequency and a noise with 0.2 mV amplitude and 1 Hz bandwidth **(top)** along with superposition of two **(down)**

Figure 53 presents the calculated root mean square (RMS) value of the wave packet in Fig. 52 (down) as the function of averaging time with blue curve. The RMS value of the signal without

noise (Black curve in Fig. 52 top) is also calculated by averaging over $t_{ave} = 3\ S$ and is presented with the red dot. Its value is 1.41×10^{-6} mV as marked in the figure.

The RMS value of the superposed signal drops with increasing averaging time until it converges to the RMS value of the pure signal at $t_{ave} = 2\ S$ and it remains close to this value for longer averaging times. Considering $\tau = 2\ S$ to be the desired Time Constant for Lock-in measurements in this case, one might recognize that it's equal to the $\frac{1}{\Delta f/2}$ or consequently the bandwidth of the detector can be written as

$$\Delta f = \frac{2}{\tau} \qquad (50)$$

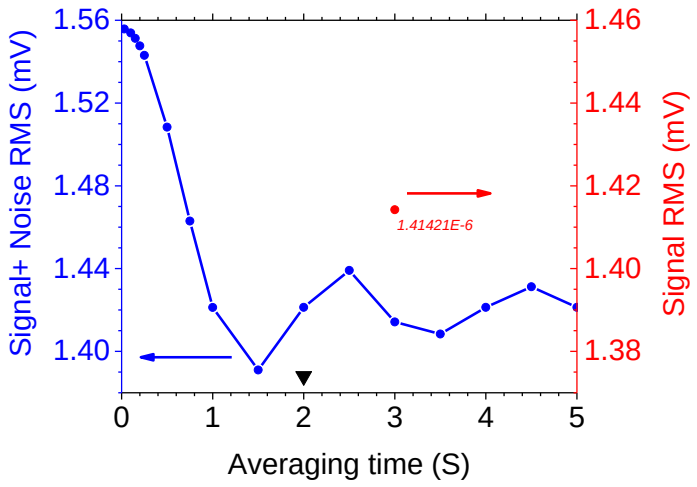

Figure 53: Plot of RMS value of the superposed signal as a function of averaging time. The RMS value of the pure signal without noise is presented with the red dot in the figure. this dot is calculated by averaging the signal for 3 seconds.

APPENDIX F:
CALCULATION OF THE DEVICE ABSORPTION AS A FUNCTION OF APPLIED V_g AT A FIX RADIATION FREQUENCY.

This program is written in Wolfram Mathematica to calculate the absorption of out grating-gated HEMTs as a function of applied V_g at a given constant free space radiation frequency.

```
(*Fundamental constants, Gaussian units*)

e=4.80325 10^-10 (*electron charge, Sqrt[dyne-cm^2]*);
e1=1.6 10^-19 (*electron Charge, Coulomb*);
c=2.99792 10^10 (*speed of light, cm/s*);
m=9.10939 10^-28 (*electron mass, g*);
p=N[Pi];
eps0=10^7/(4 p (c/100)^2)  (*permittivity of free space, C^2/N-m^2*);

(*Device parameters*)

d=380 10^-8 (*2DEG depth, cm*);
tOVERa= 0.22(*ratio of grating window widths to grating period*);
a=9 10^-4 (*grating period, cm*);
t=tOVERa a (*width of grating windows, cm*);

(*ns calculation*)

nd=1.55 10^16 (*delta doping charge density, m-2*);
ϕb=0.7 (*Schottky barrier height*);
x=0.68(*mole fraction of In in Subscript[In,x]Subscript[Ga,1-x]As*);
Ec=0.344+0.487x(*conduction band offset for InGaAs/InAlAs (x>0.58)(eV) from
Appl.Phys.Lett 60(6),Feb.1992 733-735*);
epst=12.24(*InAlAs permittivity*);
eps0=8.85 10^-12(*Vacuum permittivity in F/m*);
dm=d/100(*2DEG depth, m*);
ns[Vg_]:=((((epst*eps0)/(e1*dm))*(Vg-ϕb+Ec)+nd)/(1 10^4)) (*Sheet charge density as a
function of gate bias, cm-2*);
t0=Table[{i,ns[i]},{i,-0.6,1,0.1}]

(*Materials parameters*)

mef=0.043m (*electron effective mass gram*);
tau=6.5 10^-12 (*relaxation time, sec*);
es=13.90(*In[.68]Ga[.32]As substrate permittivity*);
eo=12.24(*In[.52]Al[.48]As top layer permittivity*);
rh=1050 4 p eps0/100 (*2D resistivity in grating gaps, first # is ohms, rest converts to s/cm*);
```

```
rl=rh 0.1 4 p eps0/100 (*2D resistivity of grating bars, s/cm*);

(*experimental parameters*)
Vgm=-0.6(*minimum frequency, rad/s*);
dVgm=0.001 (*frequency resolution rad/s*);
freq1= 2 p 93 10^9 (*First measurment frequency, rad/s*);

(*Derived quantities*)

ra=(t/a) rh + (1-t/a) rl(*average 2D surface resisitivity s/cm*);
sa=(t/a) (1/rh) + (1-t/a) (1/rl) (*average 2D surface conductivity, cm/s*);
g=2 p/a (*grating wavevector, 1/cm*);

(*Defined functions for device*)

vt[Vg_,time_]:= ns[Vg] e^2 time/mef (*cm/s*);
d1[x_,time_]:=(1-x^2 time^2)^2 + 4 x^2 time^2;
alf[x_,Vg_,time_]:=vt[Vg,time] (1+x^2 time^2)/d1[x,time];
bet[x_,Vg_,time_]:=vt[Vg,time] x time (1+x^2 time^2)/d1[x,time];
d2[x_,k_,Vg_,time_]:=(es+eo Coth[k g d] - 4 p k g bet[x,Vg,time]/x)^2+(4 p k g
alf[x,Vg,time]/x)^2;
ak[x_,k_,Vg_,time_]:=eo^2 (1-Coth[g k d]^2) alf[x,Vg,time]/d2[x,k,Vg,time];
bk[x_,k_,Vg_,time_]:=((4 p g k/x) (1+eo Coth[g k d]) (alf[x,Vg,time]^2+bet[x,Vg,time]^2)-
(2(es+eo (1+es) Coth[g k d])+eo^2(1+Coth[g k d]^2)) bet[x,Vg,time]+(es+eo Coth[g k d])
(es+eo (1+es) Coth[g k d]+eo^2) (x/(4 p g k)))/d2[x,k,Vg,time];
rtl[k_]:=(2/(p k)) (rh-rl) Sin[p k t/a];
uE[x_,Vg_,time_]:=(1/ra)-(1/2) Sum[(rtl[k]/ra)^2 ak[x,k,Vg,time],{k,1,10}];
uF[x_,Vg_,time_]:=-(1/2) Sum[(rtl[k]/ra)^2 bk[x,k,Vg,time],{k,1,10}];
bigD[x_,Vg_,time_]:=((1+Sqrt[es]+(4 p/c) (alf[x,Vg,time]+uE[x,Vg,time])) (1+Sqrt[es]+(4p/c)
(alf[x,Vg,time] + sa))-(4 p/c)^2 ((bet[x,Vg,time]+uF[x,Vg,time]) bet[x,Vg,time]))^2+((4 p/c)
(bet[x,Vg,time]+uF[x,Vg,time]) (1+Sqrt[es]+(4 p/c) (alf[x,Vg,time]+sa))+(4 p/c) bet[x,Vg,time]
(1+Sqrt[es]+(4 p/c) (alf[x,Vg,time]+uE[x,Vg,time])))^2;
Eyy2[x_,Vg_,time_]:=(4(1+Sqrt[es]+(4 p/c) (alf[x,Vg,time]+sa))^2+(8 p
bet[x,Vg,time]/c)^2)/bigD[x,Vg,time];
Ezy2[x_,Vg_,time_]:=0.;
Ty[x_,Vg_,time_]:=Sqrt[es] (Eyy2[x,Vg,time]+Ezy2[x,Vg,time]);
Ezz2[x_,Vg_,time_]:=(4(1+Sqrt[es]+(4 p/c) (alf[x,Vg,time]+uE[x,Vg,time]))^2+(8 p/c)^2
(bet[x,Vg,time]+uF[x,Vg,time])^2)/bigD[x,Vg,time];
Eyz2[x_,Vg_,time_]:=0.;
Tz[x_,Vg_,time_]:=Sqrt[es] (Ezz2[x,Vg,time]+Eyz2[x,Vg,time]);
TtotDevice[x_,Vg_,time_]:=(Ty[x,Vg,time]+Tz[x,Vg,time])/2;
```

```
(*Reference sample Functions*)

tOVERaref= 1;
tref=tOVERaref a (*width of grating windows, cm*);

(*Derived Functions for device*)

raref=(tref/a) rh + (1-tref/a) rl(*average 2D surface resisitivity s/cm*);
saref=(tref/a) (1/rh) + (1-tref/a) (1/rl) (*average 2D surface conductivity, cm/s*);
rtlref[k_]:=(2/(p k)) (rh-rl) Sin[p k tref/a];
uEref[x_,Vg_,time_]:=(1/raref)-(1/2) Sum[(rtlref[k]/raref)^2 ak[x,k,Vg,time],{k,1,10}];
uFref[x_,Vg_,time_]:=-(1/2) Sum[(rtlref[k]/raref)^2 bk[x,k,Vg,time],{k,1,10}];
bigDref[x_,Vg_,time_]:=((1+Sqrt[es]+(4 p/c) (alf[x,Vg,time]+uEref[x,Vg,time]))
(1+Sqrt[es]+(4p/c) (alf[x,Vg,time] + saref))-(4 p/c)^2 ((bet[x,Vg,time]+uFref[x,Vg,time])
bet[x,Vg,time]))^2+((4 p/c) (bet[x,Vg,time]+uFref[x,Vg,time]) (1+Sqrt[es]+(4 p/c)
(alf[x,Vg,time]+saref))+(4 p/c) bet[x,Vg,time] (1+Sqrt[es]+(4 p/c)
(alf[x,Vg,time]+uEref[x,Vg,time])))^2;
Eyy2ref[x_,Vg_,time_]:=(4(1+Sqrt[es]+(4 p/c) (alf[x,Vg,time]+saref))^2+(8 p
bet[x,Vg,time]/c)^2)/bigDref[x,Vg,time];
Ezy2ref[x_,Vg_,time_]:=0.;
Tyref[x_,Vg_,time_]:=Sqrt[es] (Eyy2ref[x,Vg,time]+Ezy2ref[x,Vg,time]);
Ezz2ref[x_,Vg_,time_]:=(4(1+Sqrt[es]+(4 p/c) (alf[x,Vg,time]+uEref[x,Vg,time]))^2+(8 p/c)^2
(bet[x,Vg,time]+uFref[x,Vg,time])^2)/bigDref[x,Vg,time];
Eyz2ref[x_,Vg_,time_]:=0.;
Tzref[x_,Vg_,time_]:=Sqrt[es] (Ezz2ref[x,Vg,time]+Eyz2ref[x,Vg,time]);
Ttotref[x_,Vg_,time_]:=(Tyref[x,Vg,time]+Tzref[x,Vg,time])/2;

Absorp[x_,Vg_,time_]:=1-(TtotDevice[x,Vg,time]/Ttotref[x,Vg,time]);
t4=Table[{i,Absorp[freq1,i,tau]},{i,-0.5,0.85,0.001}];
ListPlot[t4, PlotJoined→True, PlotRange→{0.65,0.85},Frame→True]

SetDirectory["D:\\Most up to date folders\\Research\\HEMT Project\\HEMT-UCF\\HEMT
Data\\PLS020 Series\\PLS023C (Sub-THz device-UCF)\\Calculated Plasmon Spectrum\\11-15-
2013 (Nov 2013 data)\\Gate bias dependence spectra at fix frequency"]
Export["93 Ghz freq-tau6,5-nsOVER21,5-a9u-A.txt",t4,"CSV"]
```

APPENDIX G:
ANALYSIS OF AM EXPERIMENT RESULTS WITH MODIFIED n_s AND τ.

Sheet charge density of a HEMT can be calculated from Eq. 5. Table 7 presents the sheet charge density values for the sub-THz device at different gate-biases with V_{th} = -0.85 V, d = 38 nm, and ε_t = 12.24. These are the calculated values from the measured I-V curves at the time of AM experiment.

Table 7: Sheet charge density values as a function of applied V_g

V_g (V)	n_s ($\times 10^{12}$ cm^{-2})
0.8	2.93
0.6	2.57
0.4	2.22
0.2	1.86
0	1.52
-0.2	1.15
-0.4	0.793

Figure 54 presents the measured photoresponse of the unbiased device, V_{SD} = 0 V. Absorption of the device at two constant frequencies of 80 and 101 GHz is calculated for different V_g values and compared with the measurements. Sheet charge density values used in calculations are the values in table 7 divided by a factor of 20.5, therefore, for these values we have

$$n'_{s(V_g)} = n_{s(V_g)}/20.5 = \left[n_{s(V_g=0)} + \frac{\varepsilon_t \varepsilon_0}{ed} V_g\right]/20.5 \qquad (51)$$

Theory curves for two relaxation times of 6.5 and 30 ps are compared with measurements in Fig. 54 (top) and (Bottom), respectively.

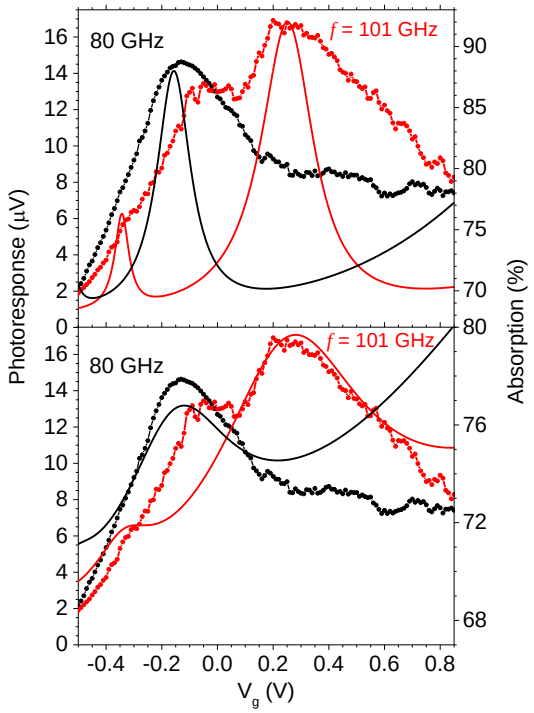

Figure 54: Measured photoresponse of the unbiased device compared with calculated absorption at different V_g values.

Absorption spectra of the device are also calculated and presented in figures 55 and 56 for relaxation times of 30 and 6.5 ps, respectively. The sheet charge densities used in these calculations are similar to the ones used in calculation of theory curves in Fig. 54. The two measurement frequencies of 82 and 101 GHz are also marked with two black and red dashed lines, respectively.

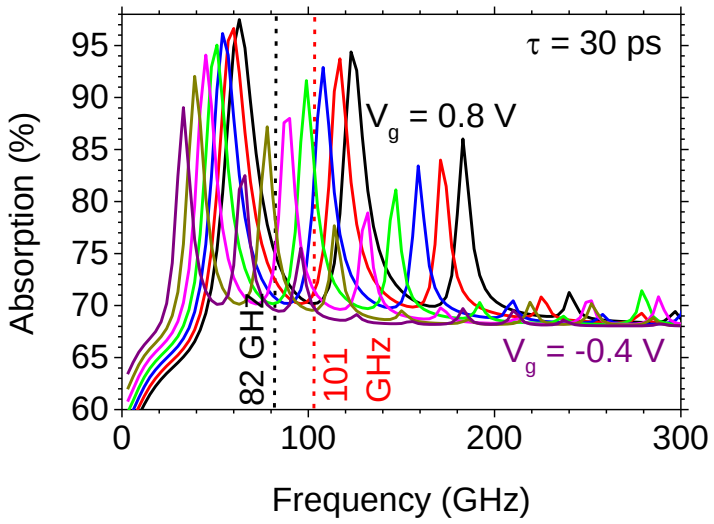

Figure 55: Calculated absorption spectra of the sub-THz device with an imaginary relaxation time of 30 ps.

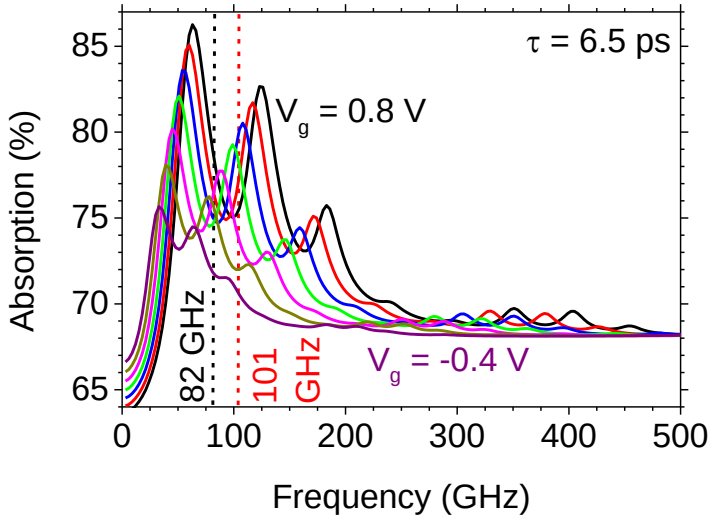

Figure 56: Calculated absorption spectra of the sub-THz device with an imaginary relaxation time of 6.5 ps. Sheet charge density values used are the values of table 7 divided by 20.5.

In Fig. 54, the two measured photoresponse peaks to 101 GHz radiation are separated by ΔV_g ~ 0.35 V 101. Calculated absorption curve, however, predicts a larger of ΔV_g ~ 0.6 V. This results in low V_g absorption peak to position to the left of the single peak at 82 GHz absorption curve, in contrast with the measured photoresponse. The ΔV_g between the two peaks in the theoretical 101 GHz absorption curve is derived as follows:

The plasmon dispersion curve in the sub-THz device is:

$$\omega_n = \sqrt{\frac{e^2 n_s'(V_g) d}{m^* \varepsilon_0 \varepsilon_t}}\, 2\pi n/a \qquad (52)$$

In Fig. 52, 101 GHz absorption curve shows a double peak. Comparing with Fig. 53, it is seen that the two peaks at low and high V_g values are representations of 3rd and 2nd order harmonics, respectively. At this excitation frequency, therefore, we will have

$$\omega_2 = \omega_3 \qquad (53)$$

Substituting Eq. 52 into Eq. 53, we will get

$$n'_{s,2} = \frac{9}{4} n_{s,3}' \qquad (54)$$

Also, calculating for $\Delta n_s' = n_{s,2}' - n_{s,3}'$ from Eq. 51, we will have

$$\Delta n'_s = n'_{s,2} - n'_{s,3} = \frac{\varepsilon_t \varepsilon_0}{20.5\, ed}\left(V_{g,2} - V_{g,3}\right) \qquad (55)$$

Substituting Eq. 54 in Eq. 55 gives

$$\Delta V_g = 25.625\left({n_{s,3}}'ed/\varepsilon_t\varepsilon_0\right) = 1.25\left(n_{s,3}ed/\varepsilon_t\varepsilon_0\right) \quad (56)$$

From Eq. 56, it is obvious that the V_g separation between the 3rd and 2nd order harmonics depends on the fixed parameters of the device's layer structure, namely ε_0, d, and the sheet charge density at the V_g where the peak of the 3rd harmonic is positioned. All these parameters are independent of the τ and n_s' values used in the calculations of the theory curves, and therefore, the calculated ΔV_g will remain the same regardless of the chosen values of n_s' and τ.

The line-shape and FWHM of the peaks in theory curves with τ = 6.5 ps have a better agreement with the experiment; however, they cannot explain the flat photoresponse to 82 GHz radiation at V_g > 0.2 V. A drastic increase in τ is required to be able to explain the flat photoresponse as evidenced by the theory curves with τ = 30 ps. In this case, however, the line-shapes of the theory curves don't agree with the experiment.

APPENDIX H: LIST OF PUBLICATIONS

Journal Publications

1) N. Nader Esfahani, R. E. Peale, W. R. Buchwald, X. Qiao, J. R. Hendrickson, and J. W. Cleary, "*Nonlinear voltage-tunable photoresponse of InGaAs/InP HEMTs to sub-THz radiation due to excitation of 2D plasmons.*", Submitted, Appl. Phys, Lett, (2014)

2) N. Nader Esfahani, R. E. Peale, W. R. Buchwald, C. J. Fredricksen, J. R. Hendrickson, and J. W. Cleary, "*Millimeter-wave photoresponse due to excitation of two-dimensional plasmons in InGaAs/InP high-electron-mobility transistors.***"** Jour. Appl. Phys. 114, 033105 (2013)

Conference Proceedings

1) N. Nader Esfahani, R. E. Peale, W. R. Buchwald, J. R. Hendrickson, and J. W. Cleary, "Tunable excitation of two-dimensional plasmon modes in InGaAs/InP HEMT devices for terahertz detection**"** Proc. Of SPIE 8993-89930F (2013)

2) N. Nader Esfahani, R. E. Peale, W. R. Buchwald, J. R. Hendrickson, and J. W. Cleary, "Millimeter and terahertz detectors based on plasmon excitation in InGaAs/InP HEMT devices," ," Proc. SPIE 8624-86240Q (2013)

3) N. Nader Esfahani, R. E. Peale, W. R. Buchwald, J. R. Hendrickson, and J. W. Cleary, "First observation of a plasmon-mediated tunable photoresponse in a grating-gated InGaAs/InP HEMT for millimeter-wave detection," Proc. SPIE 8512-85120Y (2012)

4) N. Nader Esfahani, Justin W. Cleary, Robert E. Peale, Walter R. Buchwald, Christopher J. Fredricksen, Joshua Hendrickson, Michael S. Lodge, Ben D. Dawson, M. Ishigami,

"InP- and Graphene-based grating-gated transistors for tunable THz and mm-wave detection**",** Proc. of SPIE 8373-837327, (2012) (Invited)

5) N. Nader Esfahani, R. E. Peale, Christopher J. Fredricksen, Justin W. Cleary, Joshua Hendrickson, Walter R. Buchwald, Ben D. Dawson, and M. Ishigami, "Plasmonic absorption in grating-coupled InP HEMT and Graphene sheet for tunable THz detection", Proc. of SPIE 8261-82610E, (2012)

6) R. E. Peale, N. Nader Esfahani, C. J. Fredricksen, G. Medhi, J. Cleary, J Hendrickson, W. Buchwald, H. Saxena, O. Edwards, M. Lodge, B. Dawson, M. Ishigami, "InP- and Graphene-based grating-gated transistors for tunable THz and mm-wave detection", Proc. of SPIE 8164-816408, (2011) (Invited)

6) N. Nader Esfahani, C. J. Fredrickson, G. Medhi, R. E. Peale, J. W. Cleary, W. R. Buchwald, H. Saxena, and O. J Edwards, "Plasmon resonance response to millimeter-waves of grating-gated InGaAs/InP HEMT," Proc. of SPIE 8023-80230R (2011)

REFERENCES

[1] Yun-Shik Lee, "Principles of Terahertz Science and Technology", Springer, 2009.

[2] J. F. Federici, D. Gary, R. Barat, and D. Zimdars, "THz standoff detection and imaging of explosives and weapons" Proc. SPIE 5781, 75 (2005).

[3] Y. Chen, H. Liu, Y. Deng, D. Schauki. M. J. Fitch, R. Osiander, C. Dodson, J. B. Spicer, M. Shur, and X. –C. Zhang, "THz spectroscopic investigation of 2,4-dinitrotoluene", Chem. Phys. Lett. 400, 357-361 (2004).

[4] F. Huang, B. Schulkin, H. Altan, J. F. Federici, D. Gary, R. Barat, D. Zimdars, M. Chen and D. B. Tanner, "Terahertz study of 1,3,5-trinitro-s-triazine by time-domain and Fourier transform infrared spectroscopy", Appl. Phys. Lett. 85**,** 5535 (2004).

[5] W. R. Tribe, D. A. Newnham, P. F. Taday, and M. C. Kemp, "Hidden object detection: security applications of terahertz technology", Proc. SPIE. 5354, 168-75 (2004).

[6] M. J. Fitch, D. Schauki, C. Dodson, and R. Osiander, "THz spectroscopy of explosives and related compounds", Proc. SPIE. 5411, 84-91 (2004).

[7] M. J. Fitch, D. Schauki, C. A. Kelly, and R. Osiander, "Terahertz imaging and spectroscopy for landmine detection", Proc. SPIE. 5354, 45-54 (2004).

[8] Y. Chen, H. Liu, Y. Deng, D. B. Veksler, M. S. Shur, X. –C. Zhang, D. Schauki, M. J. Fitch, R. Osiander, C. Dodson, and J. B. Spicer, "Spectroscopic characterization of explosives in the far-infrared region", Proc. SPIE. 5411, 1-8 (2004).

[9] Y. C. Shen, T. Lo, P. F. Taday, B. E. Cole, W. R. Tribe, and M. C. Kemp, "Detection and identification of explosives using terahertz pulsed spectroscopic imaging", Appl. Phys. Lett. 86, 241116 (2005).

[10] M.R. Leahy-Hoppa, M. J. Fitch, X. Zheng, L.M. Hayden, and R. Osiander, "Wideband terahertz spectroscopy of explosives," Chem. Phys. Lett., 434, 227 (2007).

[11] M. J. Fitch, M. R. Leahy-Hoppa, E. W. Ott, and R. Osiander, "Molecular absorption cross-section and absolute absorptivity in the THz frequency range for the explosives TNT, RDX, HMX, and PETN", Chem. Phys. Lett. 443, 284 (2007).

[12] Online, Available: http://mtinstruments.com/THz_Generators.html

[13] Online, Available: https://www.coherent.com/downloads/OpticallyPumpedLaser.pdf

[14] R. Kohler, A. Tredicucci, F. Beltram, H. E. Beere. E. H. Linfield, A. Giles Davies, D. A. Ritchie, R. C. Lotti, and F. Rossi, "Terahertz semiconductor-heterostructure laser," Nature 417, 156-159 (2002)

[15] B. S. Williams, "Terahertz quantum-cacade lasers," Nature {hot. 1, 517-525 (2007)

[16] M. Belkin, "THz QCL sources for operation above cryogenic temperatures," Online (2008), Available: http://www.iqclsw.phys.ethz.ch/pres/belkin17.pdf

[17] K. Vijayraghavan, M. Jang, A. Jiang, X. Wang, M. Troccoli, and M.A. Belkin, "Room temperature terahertz sources with MOVPE grown quantum cascade lasers," IEEE Photon. Technol. Lett., 26**,** 391 (2014).

[18] K. Vijayraghavan, Y. Jiang, M. Jang, A. Jiang, K. Choutagunta, A. Vizbaras, F. Demmerle, G. Boehm, M. C. Amman, and M.A. Belkin "Broadly tunable terahertz generation in mid-infrared quantum cascade lasers," Nature Comm., 4**,** 2021 (2013).

[19] R.W. Adams, A. Vizbaras, M. Jang, C. Grasse, S. Katz, G. Boehm, M.C. Amann, and M.A. Belkin, "Terahertz Sources Based on Intracavity Frequency Mixing in Mid-Infrared Quantum Cascade Lasers with Passive Nonlinear Sections," Appl. Phys. Lett., 98**,** 151114 (2011).

[20] M.A. Belkin, F. Capasso, A. Belyanin, D.L. Sivco, A.Y. Cho, D.C. Oakley, C.J. Vineis, G.W. Turner, "Terahertz quantum-cascade-laser source based on intracavity difference-frequency generation," Nature Photonics 1**,** 288 (2007).

[21] R. W. Adams, K. Vijayraghavan, Q. J. Wang, J. Fan, F. Capasso, S. P. Khanna, A. G. Davies, E. H. Linfield, nd M. A. Belkin, "GaAs/$Al_{0.15}Ga_{0.85}As$ terahertz quantum cascade lasers with double-phonon resonant depopulation operating up to 172 K," Appl. Phys. Lett. 97, 131111 (2010)

[22] G. C. Dyer, C. D. Norquist, M. J. Cich, A. D. Grine, C. T. Fuller, J. L. Reno, and M. C. Wankw, "Rectified diode response of a multimode quantum cascade laser integrated terahertz transceiver," Optics Express 4, 3996 (2013).

[23] Online Available: http://virginiadiodes.com/index.php?option=com_content&view=article&id=12&Itemid=3

[24] Online, Available: http://www.terahertz.co.uk/index.php?option=com_content&view=article&id=236&Itemid=530

[25] Online, Available: http://www.tydexoptics.com/pdf/Golay_cell.pdf (2010)

[26] B. S. Karasik, D. Olaya, J. Wei, S. Pereverzev, M. E. Gershenson, J. H. Kawamura, W. R. McGrath, and A. V. Sergeev, "Record low NEP in the hot-electron titanium nanobolometers," IEEE Trans. Appl. Supercond., 17, 293–297, (2007).

[27] Online, Available: http://www.terahertz.co.uk/index.php?option=com_content&view=article&id=215&Itemid=594

[28] Online, Available: http://www.terahertz.co.uk/index.php?option=com_content&view=article&id=214&Itemid=532

[29] Online, Available: http://www.infraredlaboratories.com/uploads/IRLabs-Bolometers-WEB.pdf

[30] Online, Available: https://www.gentec-eo.com/products/thz-detectors

[31] Online, Available: http://www.tydexoptics.com/pdf/Golay_cell.pdf

[32] Online, Available: http://mtinstruments.com/Golay_Cell_Data.pdf

[33] S. J. Allen, D. C. Tsui and R. A. Logan, "Observation of the Two-Dimensional Plasmon in Silicon Inversion Layers," Phys. Rev. Lett. 38, 980 (1977).

[34] R. Tauk, F. Teppe, S. Boubanga, D. Coquillat, W. Knap, Y. M. Meziani, C. Gallon, F. Boeuf, T. Skotnicki, C. Fenouillet-beranger, D. K. Maude, S. Rumyantsev, and M. S. Shur, Appl. "Plasma wave detection of terahertz radiation by silicon field effects transistors: Responsivity and noise equivalent power," Phys. Lett 89, 253511 (2006).

[35] G. C. Dyer, G. R. Aizin, S. Preu, N. Q. Vinh, S. J. Allen, J. L. Reno, and E. A. Shaner, "Inducing an Incipient Terahertz Finite Plasmonic Crystal in Coupled Two Dimensional Plasmonic Cavities," Phys. Rev. Lett., 109, 126803 (2012).

[36] E. A. Shaner, M. Lee, M. C. Wanke, A. D. Grine, J. L. Reno, and S. J. Allen, "Single-quantum-well grating-gated terahertz plasmon detectors," Appl. Phys. Lett, 87, 193507 (2005).

[37] X. G. Peralta, S. J. Allen, M. C. Wanke, N. E. Harff, J. A. Simmon, M. P. Lilly, J. L. Reno, P. J. Burke, and J. P. Eisenstein, "Terahertz photoconductivity and plasmon modes in double-quantum-well field-effect transistors," Appl. Phys. Lett. 81**,** 1627 (2002).

[38] W. Knap, Y. Deng, S. Rumyantsev, M. S. Shur, "Resonant detection of subterahertz and terahertz radiation by plasma waves in submicron field-effect transistors," Appl. Phys. Lett. 81, 4637 (2002).

[39] E. A. Shaner, A. D. Grine, M. C. Wanke, M. Lee, J. L. Leno, and S. J. Allen, "Far-infrared Spectrum Analysis Using Plasmon Modes in a Quantum-Well Transistor" IEEE Photon. Technol. Lett. 18, 1925 (2006).

[40] G. C. Dyer, G. R. Aizin, J. L. Reno, E. A. Shaner and S. J. Allen, "Novel Tunable Millimeter-Wave Grating-Gated Plasmonic Detectors," IEEE J. Sel. Top. Quantum Electron. 17, 85 (2011).

[41] G. C. Dyer, S. Preu, G. R. Azin, J. Mikalopas, A. D. Grine, J. L. Reno, J. M. Hensley, N. Q. Vinh, A. C. Gossard, M. S. Sherwin, S. J. Allen, and E. A. Shaner, "Enhanced performance of resonant sub-terahertz detection in a plasmonic cavity," Appl. Phys. Lett. 100, 083506 (2012).

[42] G. C. Dyer, G. R. Azin, S. J. Allen, A. D. Grine, D. Bethke, J. L. Reno, and E. A. Shaner, "Induced transparency by coupling of Tamm and defect states in tunable terahertz plasmonic crystals" Nature Photon. **7**, 925 (2013).

[43] M. Lee, M. C. Wanke, and J. L. Reno, "Millimeter wave mixing using plasmon and bolometric response in a double-quantum-well field-effect transistor," Appl. Phys. Lett., 86, 033501 (2005).

[44] A. Satou, V. Ryzhii, I. Khmirova, M. Ryzhii, and M. S. Shur, "Characteristics of a terahertz photomixer based on a high-electron mobility transistor structure with optical input through the ungated regions" J. Appl. Phys. 95, 2084 (2004).

[45] A. R. Davoyan, V. V. Popov, and S. A. Nikitov, "Tailoring Terahertz Near-Field Enhancement via Two-Dimensional Plasmons" Phys. Rev. Lett. 108, 127401 (2012).

[46] A. V. Muravjov, D. B. Veksler, V. V. Popov, O. V. Polischuk, N. Pala, X. Hu, R. Gaska, H. Saxena, R. E. Peale, and M. S. Shur, "Temperature dependence of plasmonic terahertz

absorption in grating-gate gallium-nitride transistor structure" Appl. Phys. Lett. 96, 042105-1 (2010).

[47] H. Saxena, R. E. Peale, and W. R. Buchwald, "Tunable two-dimensional plasmon resonances in an InGaAs/InP high electron mobility transistor," J. Appl. Phys. 105**,** 113101-1 (2009).

[48] N. Nader Esfahani, R. E. Peale, W. R. Buchwald, C. J. Fredricksen, J. R. Hendrickson, and J. W. Cleary, "Millimeter-wave photoresponse due to excitation of two-dimensional plasmons in InGaAs/InP high-electron-mobility transistors," J. Appl. Phys., 114, 033105 (2013).

[49] N. Nader Esfahani, R. E. Peale, C. J. Fredricksen, J. W. Cleary, J. R. Hendrickson, W. R. Buchwald, B. D. Dawson, M. Ishigami, "Plasmon absorption in grating-coupled InP HEMT and Graphene sheet for tunable THz detection" Proc. SPIE 8261, 82610E (2012).

[50] N. Nader Esfahani, R. E. Peale, W. R. Buchwald, J. R. Hendrickson, and J. W. Cleary, "Millimeter and terahertz detectors based on plasmon excitation in InGaAs/InP HEMT devices." Proc. SPIE 8624, 86240Q (2013).

[51] N. Nader Esfahani, R. E. Peale, W. R. Buchwald, J. R. Hendrickson, and J. W. Cleary, "First observation of a plasmon-mediated tunable photoresponse in a grating-gated InGaAs/InP HEMT for millimeter-wave detection" Proc. SPIE 8512, 85120Y (2012).

[52] A. El Fatimy, F. Teppe, N. Dyakonova, W. Knap, D. Seliuta, G. Valusis, A. Shchepetov, Y. Roelens, S. Bollaert, A. Cappy, and S. Rumyantsev, "Resonant and voltage tunable

terahertz detection in InGaAs/InP nanometer transistors," Appl. Phys. Lett. 89, 131926 (2006).

[53] T. Otsuji, T. Watanabe, S. A. Boubanga Tombet, A. Satou, W. M. Knap, V. V. Popov, M. Ryzhii, V. Ryzhii, "Emission and Detection of Terahertz Radiation Using Two-Dimensional Electrons in III-V Semiconductors and Graphene," IEEE Trans. On THz Science and Tech. 3, 63 (2013).

[54] T. Ptsuji, M. Hanabe, and O. Ogawara, "Terahertz plasma wave resonance of two-dimensional electrons in InGaP/InGaAs/GaAs high-electron-mobility transistors," Appl. Phys. Lett. 85, 2119 (2004).

[55] W. Knap, V. Kachorovskii, Y. Deng, S. Rumyantsev, J. –Q. Lu, R. Gaska, and M. S. Shur, "Nanresonant detection of terahertz radiation in field effect transistors," J. Appl. Phys. 91, 9346 (2002).

[56] L. Ju, B. Geng, J. Horng, C. Girit, M. Martin, Z. Hao, H. A. Bechtel, X. Liang, A. Zettl, Y. Ron Shen, and F. Wang, "Graphene plasmonics for tunable terahertz metamaterials," Nature Nanotech. 6. 630 (2011)

[57] L. Vicarelli, M. S. Vitiello, D. Coquillat, A. Lombardo, A. C. Ferrari, W. Knap, M. Polini, V. Pellegrini, and A. Tredicucci, "Graphene field-effect transistors as room-temperature terahertz detectors," Nature Mat. 11, 865 (2012).

[58] A. A. Grinberg, "The effect of the two-dimensional gas degeneracy on the I-V characteristics of the modulation-doped field-effect transistor," J. Appl. Phys. 60, 1097 (1986).

[59] A. A. Grinberg, and M. Shur, “A new analytical model for heterostructure field-effect transistors,” J. Appl. Phys. 65. 2116 (1989).

[60] A. K. Das, M. L. Glasser, and S. H. Payne, “On a two-dimensional electron gas modulated by a periodic potential,” J. Phys. C: Solid State Phys. 21 357 (1988).

[61] M. J. Kelly, “The two dimensional electron gas in a periodic potential,” Surface Science, 170, 49 (1986)

[62] I. Khmyrova, R. Yamase, M. Fukuda, and N. Watanabe, “Analysis of terahertz plasma resonances in structures with two-dimensional electron systems periodically modulated by interdigitated gate,” J. Appl. Phys. 108, 074511 (2010).

[63] V. V. Popov, D. V. Fateev, O. V. Polischuk, and M. S. Shur, “Enhanced electromagnetic coupling between terahertz radiation and plasmons in a grating-gate transistor structure on membrane substrate,” Optics Express, 18, 16771 (2010).

[64] V. V. Popov, “Plasmon excitation and Plasmonic Detection of Terahertz Radiation in the Grating-Gate Field-Effect-Transistor Structures,” J. Infrared Milli. Terahz. Waves 32, 1178 (2011)

[65] V. V. Popov, O. V. Polischuk, and M. S. Shur, “Resonant excitation of plasma oscillations in a partially gated two-dimensional electron layer,” J. Appl. Phys. 89, 033510 (2005)

[66] L. Zheng, W. L. Schaich, and A. H. Macdonald, “Theory of two-dimensional grating couplers,” Phys. Rev. B. 41, 8493 (1990).

[67] M. A. Khorrami, S. El-Ghazaly, S. -Q. Yu, and H. Naseem, "Terahertz plasmon amplification using two-dimensional electron-gas layers," J. Appl. Phys. 111, 094501 (2012).

[68] K. Shinohara, Y. Yamashita, A. Endoh, K. Hikosaka, T. Matsui, T. Mimura, and S. Hiyamizu, "Ultrahigh-speed pseudomorphic InGaAs/InAlAs HEMTs with 400-GHz cutoff frequency," IEEE Elect. Dev. Lett., 22, 507 (2001)

[69] T. Suzuki, H. One, and S. Taniguchi, "High-temperature electron transport in metamorphic InGaAs/InAlAs heterostructures," Sci. and Tech. of Adv. Mat. 6, 400 (2005).

[70] N. Nader Esfahani, C. J. Fredrickson, G. Medhi, R. E. Peale, J. W. Cleary, W. R. Buchwald, H. Saxena, and O. J Edwards, "Plasmon resonance response to millimeter-waves of grating-gated InGaAs/InP HEMT," Proc. of SPIE 8023-80230R (2011).

[71] W. R. Buchwald, H. Saxena, R. E. Peale, "Tunable Far-IR Detectors/Filters Based on Plasmons in Two Dimensional Electron Gases in InGaAs/InP Heterostructures," Proc. SPIE 6678-32 (2007).

[72] J. W. Cleary, R. E. Peale, H. Saxena, and W. R. Buchwald, "Investigation of plasmonic resonances in the two-dimensional electron gas of an InGaAs/InP high electron mobility transistor," Proc, SPIE, 8023, 80230X (2011).

[73] U. K. Mishra, J. Singh, Semiconductor device physics and design (Springer, Dordrecht, 2008) p. 378, 381.

[74] J. A. Swegle, J. W. Poukey, and G. T. Leifeste, “Backward wave oscillators with rippled wall resonators: Nalytic theory and numerical simulation,” Phys. Fluids 28, 2882 (1985).

[75] L. D. Landau, E.M. Lifshitz, and L. P. Pitaevskii, Electrodynamics of Continuous Media, 2nd ed. (Elsevier Butterworth Heinemann, Amsterdam, 1984) p. 293-298.

[76] R. E. Peale; H. Saxena; W. R. Buchwald; G. Aizin; A. V. Muravjov; D. B. Veksler; N. Pala; X. Hu; R. Gaska; M. S. Shur, “Grating-gate tunable plasmon absorption in InP and GaN based HEMTs“ Proc. SPIE 7467, 74670Q (2009).

[77] D. J. Griffiths, Introduction to Electrodynamics, 3rd ed. (Pearson Education Inc. Upper Saddle River, New Jersey, 1999) p. 331-333.